UC San Diego

UC San Diego Electronic Theses and Dissertations

Title

Physical Controls on Ice Variability in the Bering Sea /

Permalink

https://escholarship.org/uc/item/75m1g99w

Author

Li, Linghan

Publication Date

2013

Peer reviewed|Thesis/dissertation

eScholarship.org Powered by the California Digital Library
University of California

UNIVERSITY OF CALIFORNIA, SAN DIEGO

Physical Controls on Ice Variability in the Bering Sea

A dissertation submitted in partial satisfaction of the
requirements for the degree
Doctor of Philosophy

in

Oceanography

by

Linghan Li

Committee in charge:

Arthur J. Miller, Chair
Ian Eisenman
Myrl C. Hendershott
Julie L. McClean
Laurence B. Milstein
Jean-Bernard Minster

2013

Copyright
Linghan Li, 2013
All rights reserved.

The dissertation of Linghan Li is approved, and it is acceptable in quality and form for publication on microfilm and electronically:

_____

_____

_____

_____

_____

_____

Chair

University of California, San Diego

2013

EPIGRAPH

To see a world in a grain of sand,
And a heaven in a wild flower,
Hold infinity in the palm of your hand,
And eternity in an hour.
—William Blake

TABLE OF CONTENTS

Signature Page . . . iii

Epigraph . . . iv

Table of Contents . . . v

List of Figures . . . vii

List of Tables . . . ix

Acknowledgements . . . x

Vita and Publications . . . xi

Abstract of the Dissertation . . . xii

Chapter 1 Introduction . . . 1

Chapter 2 Thermodynamic and Dynamic Controls on the Seasonal Cycle of Sea Ice in the Bering Sea . . . 4
- 2.1 Introduction . . . 5
- 2.2 Coupled ocean/sea-ice model . . . 7
- 2.3 Comparison with observations . . . 10
- 2.4 Thermodynamic and dynamic balances . . . 12
- 2.5 Relationship between sea ice variability and atmospheric and oceanic conditions . . . 16
  - 2.5.1 Covariability of ice with atmosphere-ocean fields . 16
  - 2.5.2 Local forcing of sea ice variability . . . 19
  - 2.5.3 Sea ice heat budget . . . 19
  - 2.5.4 Sea ice force balance . . . 20
- 2.6 Summary and Discussion . . . 22

Acknowledgements . . . 25

References . . . 26

Chapter 3 Thermodynamic and Dynamic Controls on Sea Ice Variability in the Bering Sea . . . 45
- 3.1 Introduction . . . 46
- 3.2 Method . . . 49
- 3.3 Results . . . 51
  - 3.3.1 Variability of sea ice and climatic forcing over the entire ice cover of the Bering Sea . . . 51

3.3.2 Anomalous events . . . 58
3.3.3 Local forcing of ice variation . . . 61
3.3.4 Sea ice transport through the Bering Strait . . . 68
3.4 Discussion . . . 70
3.5 Conclusion . . . 72
Acknowledgements . . . 74

References . . . 75

Chapter 4 Greenland Surface Lakes Observed by Repeated Laser Altimetry 103
4.1 Introduction . . . 104
4.2 Methods . . . 106
4.3 Results . . . 107
4.3.1 Typical ICESat observations of surface lakes . . . 107
4.3.2 Statistics of surface lakes detected by ICESat . . . 108
4.3.3 Temporal variability and correlation of lake surface elevations . . . 109
4.3.4 Lake water volume and drainage estimation . . . 110
4.3.5 Validation of lake geometry estimation and water level using independent data . . . 113
4.4 Discussions . . . 116
4.4.1 Geometry of supraglacial lakes . . . 116
4.4.2 Mechanisms for drainage of surface lakes . . . 117
4.4.3 Spatial distribution of supraglacial lakes . . . 118
4.4.4 Temporal evolution of lake water volume . . . 120
4.4.5 Correlation of water levels among lakes . . . 121
4.4.6 Lake depths estimation . . . 122
4.5 Conclusions . . . 123
Acknowledgements . . . 124

References . . . 125

Chapter 5 Conclusion . . . 139
5.1 Summary . . . 139
5.2 Future work . . . 141

Appendix A Ice thermodynamic and dynamic equations in the CICE model 143

LIST OF FIGURES

Figure 2.1: Bathymetry of the Bering Sea and model grids. 30
Figure 2.2: Total ice area comparison between model and observation. . . . 31
Figure 2.3: Seasonal ice concentration comparison between model and observation. 32
Figure 2.4: Fall ice volume tendencies. 33
Figure 2.5: Winter ice volume tendencies. 34
Figure 2.6: Spring ice volume tendencies. 35
Figure 2.7: Summer ice volume tendencies. 36
Figure 2.8: Local ice volume tendencies. 37
Figure 2.9: Total ice volume tendencies. 38
Figure 2.10: Major ocean currents in the Bering Sea. 38
Figure 2.11: Seasonal atmosphere, ocean and ice conditions. 39
Figure 2.12: Local heat fluxes and wind stress. 40
Figure 2.13: Surface heat flux budget in winter and spring. 41
Figure 2.14: Winter sea ice force balance. 42
Figure 2.15: Spring sea ice force balance. 43
Figure 2.16: Schematic of the large-scale Bering Sea winter sea ice balance. . 44

Figure 3.1: Bathymetry of the Bering Sea and model grids. 79
Figure 3.2: Total ice area from model and observation and their anomalies. 80
Figure 3.3: Total ice volume and its anomaly. 81
Figure 3.4: Thermodynamic, dynamic, and net ice volume tendencies integrated over the entire Bering Sea and their anomalies. 82
Figure 3.5: Surface air temperature over ice and its anomaly. 83
Figure 3.6: Surface heat flux budget over ice and anomalies. 84
Figure 3.7: Time series of force balance of ice and ice velocity, and their anomalies. 86
Figure 3.8: Ice condition of the anomalous event in February 1989. 87
Figure 3.9: Atmosphere and ocean conditions of the anomalous event in February 1989. 88
Figure 3.10: Ice condition of the anomalous event in February 1984. 89
Figure 3.11: Atmosphere and ocean conditions of the anomalous event in February 1984. 90
Figure 3.12: Local ice volume tendencies at the northern site and their anomalies. 91
Figure 3.13: Local surface heat flux, surface air temperature and wind anomalies at the northern site. 92
Figure 3.14: Local ice volume tendencies at the southern site and their anomalies. 93
Figure 3.15: Local surface heat flux, surface air temperature and wind anomalies at the southern site. 94

Figure 3.16: Local ocean heat flux and ocean stress anomalies at the southern site. 95
Figure 3.17: Local surface heat flux budget at the northern site and anomalies. 96
Figure 3.18: Local surface heat flux budget at the southern site and anomalies. 97
Figure 3.19: Local force balance of ice and ice velocity at the northern site and their anomalies. 99
Figure 3.20: Local force balance of ice and ice velocity at the southern site and their anomalies. 101
Figure 3.21: Modeled sea ice transport through the Bering Strait. 102

Figure 4.1: Operational time periods of the ICESat campaigns. 134
Figure 4.2: (a) Surface elevation profiles of a supraglacial lake in western Greenland from repeated ICESat laser altimeter measurements. (b) Time series of surface elevations of this supraglacial lake. (c) Surface elevation profiles of an ice-dammed lake adjacent to Petermann Glacier in northern Greenland from repeated ICESat laser altimeter measurements. (d) Time series of surface elevations of this ice-dammed lake. (e) Spatial distribution of surface lakes in Greenland detected by ICESat. 136
Figure 4.3: (a) ICESat tracks on the ASTER satellite image of one supraglacial lake near Ryder Glacier in northern Greenland. (b) ICESat measurements of the lake. (c) (d) Interpolated surface from ICESat measurements of the lake basin. (e) (f) Constructed 3D geometry of the lake basin from ICESat data. 137
Figure 4.4: (a) (b) (c) Digital Elevation Model derived from LVIS measurements of one supraglacial lake in western Greenland. (d) ICESat measurements of this lake. (e) (f) Constructed geometry of the lake basin from ICESat data. (h) (i) Constructed geometry of the lake basin from LVIS data. (g) MODIS satellite image of this lake. 138

LIST OF TABLES

Table 2.1: Model-Observation comparison of seasonal mean values. Ice area and mean concentration (area/extent) are computed for ice concentration > 15% Rms error (normalized by Rms obs) and correlation are computed over the area where both model > 0% and obs > 0% (parenthetical values where either model > 0% or obs > 0%) 29

Table 4.1: ICESat campaigns for the 3 laser altimeters and their corresponding operational periods 129

Table 4.2: Fitted model parameters for the geometries of the supraglacial lake basin near Ryder Glacier in northern Greenland and the supraglacial lake basin in western Greenland 130

Table 4.3: Maximum depth, area, and volume estimates at different times of the supraglacial lake near Ryder Glacier in northern Greenland 131

Table 4.4: Volume, area, and maximum depth estimates in different campaigns from constructed geometry of a lake basin in western Greenland based on ICESat data and LVIS data separately . . . 132

Table 4.5: Lake areas in different campaigns from constructed geometry of a lake basin in western Greenland based on ICESat data and from MODIS satellite images 133

ACKNOWLEDGEMENTS

I greatly appreciate my advisor Art Miller for his wise guidance and strong support throughout my studies of the Bering Sea.

I also thank my other PhD committee members: Julie McClean, for sharing with me her initial results with her POP-CICE simulation and helping me with understanding the model; Ian Eisenman, for teaching me about ice dynamics and discussing scientific issues with me; Myrl Hendershott for instructing me on oceanography and helping me with the basic equations; and Bernard Minster and Larry Milstein for serving on my committee and providing important feedbacks on my research. I especially thank Art, Myrl, Julie, and Ian for meeting with me regularly to discuss my research results extensively.

I also thank Helen Fricker for guidance and support during the early part of my PhD studies and for inspiring my interests in cryosphere, especially Greenland supraglacial lakes and Antarctic ice shelves.

I greatly appreciate the Scripps Graduate Department for providing funding, especially during the final year of my PhD study. The Office of Naval Research also provided partial support (N00014-13-1-0139).

I also thank all my friends for the pleasant time together and my professors at SIO for their expert opinions.

Finally, I deeply appreciate my husband Xiaopeng Tong, my parents and my brother for their persistent support and love.

Chapter 2 is in preparation for submission to Ocean Dynamics. Linghan Li, Julie L McClean, Arthur J Miller, Ian Eisenman, and Myrl C Hendershott, 2013. The dissertation author was the primary investigator and author of Chapter 2. Chapter 3 is in preparation for submission to Dynamics of Atmospheres and Oceans. Linghan Li, Arthur J Miller, Julie L McClean, Ian Eisenman, and Myrl C Hendershott, 2013. The dissertation author was the primary investigator and author of Chapter 3.

VITA

2004	B.E. in Electrical Engineering, Wuhan University
2008	M.S. in Space Physics, Chinese Academy of Sciences
2013	Ph.D. in Oceanography, Scripps Institution of Oceanography, University of California, San Diego

PUBLICATIONS

Li, L., A. J. Miller, J. L. McClean, I. Eisenman, and M. C. Hendershott, 2013: Thermodynamic and dynamic controls on sea ice variability in the Bering Sea. *Dynamics of Atmospheres and Oceans*, in preparation.

Li, L., J. L. McClean, A. J. Miller, I. Eisenman, and M. C. Hendershott, 2013: Thermodynamic and dynamic controls on the seasonal cycle of sea ice in the Bering Sea. *Ocean Dynamics*, in preparation.

Li, L. and T. Chen, 2008: Shear rate determination of flow near magnetopause. *Chinese Journal of Space Science*, **28**, 273-282.

ABSTRACT OF THE DISSERTATION

Physical Controls on Ice Variability in the Bering Sea

by

Linghan Li

Doctor of Philosophy in Oceanography

University of California, San Diego, 2013

Arthur J. Miller, Chair

This study primarily focuses on sea ice variability in the Bering Sea, and its thermodynamic and dynamic controls.

First, the seasonal cycle of sea ice variability in the Bering Sea is studied, using a global fine-resolution (1/10-degree) fully-coupled ocean and sea ice model forced with reanalysis atmospheric forcing for 1980-1989. The ocean/sea-ice model consists of the Los Alamos National Laboratory Parallel Ocean Program (POP) and the Los Alamos Sea Ice Model (CICE). The modeled seasonal mean sea ice concentration strongly resembles satellite-derived observations. During winter, which dominates the annual mean, model sea ice is mainly formed in the northern Bering Sea, with the maximum ice growth rate occurring along the coast, due to cold air from northerly winds and ice motion away from the coast. South of St.

Lawrence Island, winds drive sea ice to drift southwestward. Along the ice edge in the western Bering Sea, ice is melted by warm ocean water, which is carried by the Bering Slope Current flowing to the northwest, resulting in the S-shaped asymmetric pattern seen in the ice edge.

Second, the year-to-year variability of sea ice in the Bering Sea for 1980-1989 is addressed. While thermodynamic processes dominate the variations in ice volume change in the Bering Sea on the large scale, dynamic processes are important locally near ice margins (both oceanic and land), where local dynamic and thermodynamic ice volume changes have opposite signs with large and similar amplitudes. The thermodynamic ice volume change is dominated by ice-air surface heat flux, which in turn is dominated by sensible heat flux, except near the southern ice edge where it is largely controlled by ocean-ice heat flux. This indicates that surface air temperature, which is specified from observations, strongly controls ice volume change. Ice motion is generally consistent with winds driving the flow, except near certain straits in the north where ice motion largely follows ocean currents.

This study also addresses Greenland supraglacial lakes on top of ice and ice-dammed lakes adjacent to glaciers. Those surface lakes have been observed to fill and drain periodically, affecting the ice motion over land. This study provides observational constraints on the volume of water contained in and drained from the lakes, based on the repeat laser altimetry.

Chapter 1

Introduction

Ice is an important component of the global climate system. Ice in the northern hemisphere is very sensitive to climate variability through positive feedbacks such as ice albedo feedback. Changing ice cover has a large influence on the mass and energy balance of the climate system. This study primarily focuses on sea ice in the Bering Sea: the atmospheric and oceanic controls on its seasonal cycle (Chapter 2) and its interannual variability (Chapter 3). An additional component of this cryospheric research involves supraglacial lakes on the Greenland ice sheet (Chapter 4).

Sea ice is sensitive to climate change, because it has fast and extensive interaction with climate due to its small thickness and large area. Sea ice responds to variations in atmospheric and oceanic heat fluxes and momentum exchanges. On the other hand, sea ice affects the heat, moisture, and momentum exchange between ocean and atmosphere. The positive ice albedo feedback impacts the radiation balance of the climate system. In addition, sea ice can influence global patterns of ocean circulation: brine rejection during sea ice formation helps to form dense deep water spreading globally in the deep ocean and upwelling at lower latitudes. The Bering Sea connects the North Pacific Ocean to the Arctic Ocean, and modifies the pole-ward transport of heat, freshwater and salt. It is of importance to probe the large seasonal and interannual variability of sea ice in the Bering Sea, because it influences the marine ecosystem by affecting light, water temperature and the availability of substrate. However, understanding of

the physical mechanisms governing sea ice variability in the Bering Sea remains incomplete. **Chapter 2 and Chapter 3 address climatic forcing of sea ice variability in the Bering Sea, both on the seasonal and on the inter-annual timescales. A high-resolution ocean-sea ice model (POP-CICE) forced with observed atmospheric forcing is used as the primary tool of analysis. The Appendix presents the basic equations governing the heat, momentum and mass balances of the model sea ice.**

The ice sheets in Greenland and Antarctica contain about 99% of the world's freshwater ice, and contribute to 64 m of sea level rise if all melted. The mass balance of ice sheets affects the global sea level rise, but the contribution of ice sheets to sea level rise is still marked by large uncertainty. Ice sheets have a long response time to climate, but at the surface they respond rapidly to present climate conditions. The Greenland Ice Sheet has started to lose mass around its margin. The mass loss of the Greenland Ice Sheet consists of increased surface melting and increased ice discharge into the ocean. Greenland summer surface melt increased by 30% from 1979 to 2006. On the Greenland Ice Sheet, surface melt water accumulates in surface depressions to form supraglacial lakes, and the fast drainage of those lakes through the ice sheet to the ice-bedrock interface influences the ice flow towards the ocean. But the volume of water contained in the lakes and involved in lake drainages are poorly known. **Chapter 4 studies Greenland surface lakes using repeat-track laser altimeter data from Ice, Cloud, and land Elevation Satellite (ICESat). Draining and filling of Greenland surface lakes from their surface elevation changes are examined, and the volume of water contained in the lakes is estimated.**

This research combines the use of satellite observations and models to address fundamental processes controlling sea ice variability in the Bering Sea and the surface lakes over the Greenland ice sheet. The results indicate that additional observations are needed to better understand theses processes. For instance, ice thickness is not well observed by satellite yet it is an important aspect of the ice balance that needs to be monitored under global change. Likewise, supraglacial lakes need better coverage by satellite observations to properly estimate the vol-

ume of water lost through the rapid drainage processes that we have investigated here with limited observations. Sea ice models and ice sheet models provide a way for improving our estimate of long-term changes in sea ice and land ice in the Earth System. Additional studies using models and observations together, such as accomplished here, are needed to make further progress in understanding the global cryosphere system.

Chapter 2

Thermodynamic and Dynamic Controls on the Seasonal Cycle of Sea Ice in the Bering Sea

The seasonal cycle of sea ice variability in the Bering Sea is studied using a global fine-resolution (1/10-degree) fully-coupled ocean and sea ice model forced with reanalysis atmospheric forcing for the time period 1980-89. The ocean/sea-ice model consists of the Los Alamos National Laboratory Parallel Ocean Program (POP) and the Los Alamos Sea Ice Model (CICE). The seasonal mean fields of sea ice concentration in the model strongly resemble satellite-derived sea ice observations. Seasonal climatologies of sea-ice concentration and thickness, upper ocean temperature and velocity, surface wind and air temperature, and heat flux and momentum exchange between the ice and the atmosphere and the ocean are constructed, and changes in the ice volume are decomposed into contributions from various thermodynamic and dynamic processes.

During winter, which dominates the annual mean, we find that model sea ice is mainly formed in the northern Bering Sea, with the maximum ice growth rate occurring along the coast, due to cold air from northerly winds and ice motion away from the coast. South of St. Lawrence Island, winds drive model sea ice to drift southwestward from the north to the southwestern ice covered region. Along the ice edge in the western Bering, model ice is melted by warm ocean water, which

is carried by the model Bering Slope Current flowing to the northwest, resulting in the S-shaped asymmetric pattern seen in the ice edge. In spring and fall, similar dynamics and thermodynamics occur in the model, but with typically smaller magnitudes and with season-specific geographical and directional differences. The Bering Sea is observed to be ice free in summer, while the model has small amounts of residual ice. Surface melting is insignificant relative to basal and lateral melting in all seasons.

The driving forcings of seasonal cycle of sea ice in the Bering Sea, including heat budget and force balance for sea ice, are also studied. Seasonal thermodynamic ice volume change is dominated by surface heat flux between the atmosphere and the ice in the north, and by heat flux from the ocean to the ice along the southern ice edge especially on the western side. Sea ice motion is largely associated with wind stress. Internal ice stress is large near the land boundaries in the north, and is small in the central and southern ice-covered area.

The model has considerable skills, as quantified by rms error and pattern correlation coefficients, in reproducing the basic observed seasonal structure of sea ice concentration, therefore motivating further studies of the processes controlling the interannual variability of sea ice anomalies in the Bering Sea with this model.

2.1 Introduction

The Bering Sea connects the subpolar North Pacific to the western Arctic basin. As a result it is a climatically and economically important region that has been the focus of intense study during recent decades. It supports a large oceanic fishery for both commercial and subsistence use (Hunt et al., 2011). It contains a highly seasonal sea ice distribution, which is affected by a vigorous mesoscale eddy field (Johnson et al., 2004). Understanding the processes that control the temporal evolution of the sea ice distribution is vital to anticipating how the physical-biological system will change in future years and decades (Wang et al., 2012).

The dominant change in sea ice cover in the Bering Sea is associated with

the seasonal cycle. A conveyor belt mechanism, with a northern source, a southern sink, and an intermediate zone where ice is transported southward by northerly winds, has been proposed to explain the basic north-south structure using observations alone (Pease, 1980; Muench and Ahlnas, 1976). The satellite and in situ observations (Pease, 1980; Muench and Ahlnas, 1976; Wang et al., 2009; Stabeno et al., 2001), however, provide a limited perspective on what controls the seasonal extent and thickness of the ice. So numerical simulations are needed to better understand the dynamics and thermodynamics of these variations.

Previous sea-ice modeling studies of the Bering Sea have revealed a strong sensitivity to the types of parameterizations used in the ice model, the structure of the background oceanic circulation, and the details of the atmospheric forcing. Bitz et al. (2005) studied global sea ice in version 2 of the National Center for Atmospheric Research Community Climate System Model (NCAR CCSM2), including thermodynamic and dynamic balances on a seasonal mean basis. They noted that in the Bering Sea, which is relatively far from the pole, the ice edge location is more strongly controlled by oceanic heating effects driven by solar absorption than by ocean heat flux convergence. Zhang et al. (2010), using the Zhang-Rothrock sea ice model (Zhang and Rothrock, 2001) embedded in the Los Alamos National Laboratory Parallel Ocean Program (POP), focused on interannual sea ice variations in the Bering Sea, which they found to be dominated by wind-driven changes in ice transport and the ocean thermal front in the southern Bering Sea. Danielson et al. (2011) used the Regional Ocean Modeling System (ROMS) sea ice model to show that although the simulated seasonal structure of the sea ice pattern was realistic, the spring retreat of sea ice in the model was too slow compared to observations.

Because of the economic and climatic importance of the Bering Sea, a detailed investigation of the processes involved in establishing the climatological seasonal distribution of sea ice is needed. This can then form a baseline for determining the controls on the interannual changes in sea ice and those associated with global warming on long time scales.

We study the seasonal cycle of Bering Sea ice distribution in a forced global fine-resolution ocean/sea-ice simulation in the Community Earth System Model

(CESM) framework. The ocean/sea-ice model consists of the Los Alamos National Laboratory Parallel Ocean Program (POP) and the Los Alamos Sea Ice Model (CICE). This simulation was run with Coordinated Ocean-Ice Reference Experiment version 2 (CORE2) interannual atmospheric forcing.

In the following sections, we introduce the sea ice-ocean model (Section 2.2), compare the simulation results with available satellite observations (Section 2.3), determine the relative importance of terms in the thermodynamic and dynamic equations controlling the ice variability (Section 2.4), and examine the relationship between sea ice variability and atmospheric and oceanic conditions (Section 2.5). Lastly, we summary the results and discuss directions for future work (Section 2.6).

2.2 Coupled ocean/sea-ice model

We use output from a fine resolution (1/10-degree) global coupled ocean/sea-ice simulation that was run in the CESM framework with the component models POP and CICE. Sea-ice variability and its causes have been studied in earlier POP/CICE simulations configured at lower horizontal resolution, e.g., by Ivanova et al. (2012); Prasad et al. (2005); Hunke et al. (2008). This simulation is configured on a tripole grid; the two Northern Hemisphere poles lie in Canada and Russia. Figure 2.1 shows the model grid points subsampled every 10 points and bathymetry of the Bering Sea used in the model.

CICE utilizes the energy-conserving thermodynamic sea ice model by Bitz and Lipscomb (1999) to compute ice/snow growth and melt rates. CICE has one snow layer and four ice layers. CICE uses a subgridscale ice thickness distribution with five ice thickness categories: $0.00m \sim 0.60m$, $0.60m \sim 1.40m$, $1.40m \sim 2.40m$, $2.40m \sim 3.60m$, $> 3.60m$. For each ice thickness category, the model calculates the ice and snow thickness changes and vertical temperature profiles based on vertical radiative, turbulent and conductive heat fluxes. The model considers the effect of brine pockets on specific heat and thermal conductivity due to internal melting and freezing. The vertical salinity profile is prescribed as a constant. CICE use the elastic-viscous-plastic (EVP) sea ice dynamic model by

Hunke and Dukowicz (1997) to compute ice velocity. The ice momentum equation consists of 5 stresses: wind stress, ocean stress, internal ice stress, Coriolis stress, and stress due to sea surface slope. CICE uses an incremental remapping advection scheme. The important ice thermodynamic and dynamic equations used by CICE are summarized in the Appendix.

POP is a z-level ocean general circulation model which solves the three-dimensional primitive equations for ocean temperature, salinity and momentum. It has an implicit free surface. It uses partial bottom cells for better representation of flow over the bottom boundary. POP has 42 levels of thickness, from 10 m thick in the uppermost layer to 250 m thick in the deep ocean. The horizontal resolution is around 6 km in the Bering Sea. POP and CICE are coupled via an external flux coupler.

This model run is forced with Coordinated Ocean-ice Reference Experiment version 2 (CORE2) interannually varying atmospheric forcing from 1970-1989 (Large and Yeager, 2009). CORE 2 includes 6-hourly (1948-2006) surface wind velocity, specific humidity and air temperature based on NCEP reanalysis, daily radiation (1984-2006) and monthly precipitation (1979-2006) from satellite observations. Climatological mean annual cycles are used for radiation (1948-1983) and precipitation (1948-1978) before satellite observational periods. Some data sets are adjusted to satellite and in situ observations in the mean. For example, NCEP winds are adjusted to QuikSCAT satellite scatterometer winds (2000-2004): wind speed is increased almost everywhere, but wind direction is not corrected. Fluxes of heat, momentum and fresh-water at the surface are calculated interactively with the model variables of SST, ice/snow surface temperature, and ice surface roughness. CORE2 is on T62 grid with a horizontal resolution of $\sim 100km$ (east-west) and $\sim 200km$ (north-south) in the Bering Sea.

This simulation was integrated for years 1970-1989. Here we analyze years 1980-1989. The first 10 years (1970-1979) are treated as a spin-up period. The initial condition is a uniform ice of 2 m thick poleward of 75° N and 65° S. Further details can be obtained from McClean et al. (2013).

The governing equations for evolution of ice concentration and ice volume

are shown in the Appendix. The model saves monthly-mean variables along with accumulated terms in the thermodynamic and dynamic balances (e.g. ice volume tendency terms due to thermodynamics and dynamics). The primary equation of interest is the equation partitioning the ice volume tendency $\frac{\partial V}{\partial t}$ (partial time derivative of ice volume) into two components:

$$\frac{\partial V}{\partial t} = \frac{\partial V_T}{\partial t} + \frac{\partial V_D}{\partial t} \tag{2.1}$$

where the first term $\frac{\partial V_T}{\partial t}$ on the right-hand side is the ice volume tendency due to thermodynamics, and the second term $\frac{\partial V_D}{\partial t}$ on the right-hand side is the ice volume tendency due to dynamics. The dynamic component of the ice volume tendency is determined by the convergence of the product of ice velocity and ice volume

$$\frac{\partial V_D}{\partial t} = -\nabla \cdot (\mathbf{u}V) \tag{2.2}$$

where V is ice volume and $\mathbf{u}$ is ice velocity.

The thermodynamic component of the ice volume tendency can be further separated into the growth rate and the melt rate

$$\frac{\partial V_T}{\partial t} = G + M \tag{2.3}$$

where G is the growth rate, representing a sum of congelation ice growth, frazil ice growth, and snow-ice formation, and M is the melt rate, representing a sum of basal melt, lateral melt, and surface melt. Here the melt rate M is negative, meaning contributing to ice volume decrease. Basal melt/congelation ice growth is determined by the difference between the net heat flux from the ocean to the ice and the conductive heat flux at the bottom surface of the ice. Surface melt is determined by the difference between the net heat flux from the atmosphere to the ice and the conductive heat flux from the top ice surface to the ice interior. The melt rate is broken up into the basal/lateral melt rate and the surface melt rate

$$M = M_{BL} + M_S \tag{2.4}$$

where M_{BL} is the sum of basal and lateral melt rates and M_S is the surface melt rate, and both of them are negative.

The basic equations governing the mass and heat balances of the sea ice in the model are summarized in the Appendix.

2.3 Comparison with observations

We first consider how well the model captures the regional variability of the spatial extent of sea ice during the time period of the run. We obtained observed "ice concentration", which varies from 0 to 1, from satellite passive microwave data on a 25 km grid. We used Bootstrap Sea Ice Concentrations from Nimbus-7 SMMR and DMSP SSM/I-SSMIS, which is publicly available at National Snow & Ice Data Center (Comiso, 2000). This dataset has an error of approximately 5-10% which varies with season, and this error is larger for thin ice and ice with surface melt, especially near the ice edge. Here we follow the standard convention of defining the "ice edge" as the 15% ice concentration contour line. "Ice area" is defined as the sum of ice concentration multiplied by the grid cell area for grid cells where ice concentration is at least 15%, considering only the Bering Sea region (south of the Bering Strait, north of Aleutian Islands, and bounded by land in the east and the west).

Figure 2.2a shows the monthly-mean ice area in the Bering Sea for both model and observations during the 1980-1989 time period. The model tracks the observed seasonal evolution of sea ice rather closely and captures many aspects of the interannual variability as well. A bias exists, however, in that the model tends to have too little ice in cold months. The ROMS model simulation of Danielson et al. (2011) also has a bias towards too low ice area. Ivanova et al. (2012), in contrast, simulated a winter-mean ice distribution during 1990-2002 in POP-CICE (0.4 deg grid and forced with NCEP/NCAR forcing) which had larger concentrations than NASATEAM SSM/I satellite observations in the Bering Sea, as shown in their Figure 3.

Figure 2.2b shows the 10-year climatological seasonal cycle of the ice area in the Bering Sea. The model tracks the observed seasonal cycle, with a rapid retreat of sea ice in spring, but a low bias exists in fall, winter and early spring.

Although the model does not retreat as fast as observations, it appears to retreat more rapidly than ROMS, based on the similar plot presented by Danielson et al. (2011).

Figure 2.2b shows the 10-year climatological seasonal cycle of the ice area in the Bering Sea. The model tracks the observed seasonal cycle, with a rapid retreat of sea ice in spring, but a low bias exists in fall, winter and early spring (6-20% from December to April). Although the model does not retreat as fast as observations, it appears to retreat more rapidly than ROMS, based on the similar plot Figure 11 presented Danielson et al. (2011).

The model underestimation of the Bering Sea ice area maybe associated with lack of tidal effects in the POP-CICE model, which could be important over the shallow Bering shelf. Zhang et al. (2010) show that the difference of model sea ice thickness with and without tides is up to 0.1 m or 15% in the central-eastern Bering Sea. It is also possible that uncertainty in the atmospheric forcing, especially radiative forcing, at high latitudes could cause this model bias. It might be also related to the fact that the ice surface near the ice edge is rougher because of rafting and thus the air-ice drag coefficient is larger there, which the model does not take into account.

We next address the seasonal mean structures of sea ice in the model compared with observations. We define winter as Jan-Feb-Mar, spring as Apr-May-June, summer as July-Aug-Sep, and fall as Oct-Nov-Dec. Figure 2.3 shows the seasonal means (fall, winter, spring and summer) of ice concentration for 1980-1989 from the model (a-d) and satellite observations (e-h), and the difference between the two (i-l). In winter (Figure 2.3b, f and j), the spatial structure of model ice concentration appears to be very similar to the observed ice concentration, except near the eastern coastal region and the Kamchatka coastal region where the model has too little ice. In fall (Figure 2.3a, e and i), there is a substantial low bias of ice in Norton Sound and along the eastern coast and a high bias in the Gulf of Anadyr. In spring (Figure 2.3c, g and k), the model simulates too much ice in the Gulf of Anadyr and too large an ice concentration maximum in the central Bering region. The model also produces less ice near much of the coast than is evident in the

observations. In these coastal areas, the model simulates small-scale polynya-like features, which may not be accurately captured by the lower-resolution satellite observations ($\sim 25km$) due to land-to-ocean spillover effects (Parkinson et al., 1987; Maslanik et al., 1996). In summer, no ice is observed in Figure 2.3h, but the model contains some small regions with some ice near the coast of the Gulf of Anadyr in Figure 2.3d.

We quantify the model-data mismatch by computing several statistics: Total ice area with ice concentration greater than 15%, mean ice concentration for areas with greater than 15% concentration, RMS ice concentration error, and spatial pattern correlation for areas where both model and observations contain non-zero ice concentration. These results are presented in Table 2.1. Considering ice area, the model has a low bias in fall ($\sim$ 25% less ice than observations) and winter ($\sim$ 15% less). The model simulates slightly too much ice in summer, when essentially no ice is observed in the Bering Sea (although satellite-derived observations may fail to detect very low ice concentrations due to factors including the filtering of weather effects). In terms of mean ice concentration of the ice-covered area, the model value is very similar to observations for fall, winter and spring. The normalized rms error of ice concentration is small in winter (0.16) and spring (0.22) but moderately large in fall (0.43). The spatial pattern correlation is very high in winter (0.97) and spring (0.94) and only slight weaker in fall (0.81). Statistics in summer are ill-defined due to only limited spotty regions of observed ice.

Taken as a whole, these results suggest that the POP-CICE simulation captures the main observed spatial patterns and magnitudes of ice coverage and concentration in the Bering Sea, giving confidence to the observational accuracy of a study of the model processes that control the temporal and spatial structures in the seasonal evolution of sea ice in this region.

2.4 Thermodynamic and dynamic balances

We next consider the thermodynamic and dynamic balances controlling the climatological seasonal cycle of sea ice in the Bering Sea. Figures 2.4-2.7

show, for each season, the key terms affecting the ice volume tendency, which is the first panel of each figure. Since this term is nearly zero for the annual mean and since the balances in winter tend to dominate the annual mean, we do not plot the annual mean results. The other panels in each figure correspond to the ice volume tendency due to dynamics ($\frac{\partial V_D}{\partial t}$), the ice volume tendency due to thermodynamics ($\frac{\partial V_T}{\partial t}$), the ice growth rate ($G$), the basal plus lateral melt rate (M_{BL}), and the surface melt rate (M_S). Thermodynamic ice volume tendency $\frac{\partial V_T}{\partial t}$ is the ice volume change due to ice growth (including congelation ice growth, frazil ice growth and snow ice formation) and ice melt at the bottom, surface and lateral sides of sea ice, and positive/negative value means ice volume increase/decrease due to thermodynamic processes. Dynamic ice volume tendency $\frac{\partial V_D}{\partial t}$ is the ice volume change due to ice motion, and positive/negative value means ice volume increase/decrease resulting from ice transport into/out of a certain area. The net ice volume tendency $\frac{\partial V}{\partial t}$ is the sum of thermodynamic ice volume tendency $\frac{\partial V_T}{\partial t}$ and dynamic ice volume tendency $\frac{\partial V_D}{\partial t}$.

In the fall (Figure 2.4), ice forms primarily in the open ocean region of the northeastern Bering Sea between St Lawrence Island and Norton Sound and along the coastal region (Figure 2.4d) to the west of Cape Navarin, yielding an S-shaped ice edge. The ice volume tendency is positive over the entire region containing ice as shown in Figure 2.4a. Although ice growth (Figure 2.4d) dominates the thermodynamic tendency (Figure 2.4c), some significant basal/lateral melting occurs near the coast of the Gulf of Anadyr (Figure 2.4e). We use a convention whereby ice melt is assigned negative values here rather than the positive values it has in the model simulation to simplify our interpretation of the ice volume tendency terms. Surface melting is very weak at this time (Figure 2.4f), as it is in all seasons. The dynamic ice volume tendency shown in Figure 2.4b implies a transport of ice from the coastal regions of the northern Bering Sea to build up the sea ice southwestward of St Lawrence Island and in the Gulf of Anadyr, where some open ocean melting also occurs in Figure 2.4e.

In winter (Figure 2.5), when sea ice reaches its maximum extent, strong ice growth rates occur near all the northern Bering Sea coastal regions, including

southeastward into the northern Bristol Bay (Figure 2.5d). Growth rates are also high in open oceans ranging diagonally from the northwest to the southeast across the northern Bering Sea (Figure 2.5d). As shown in Figure 2.5b, dynamical export of ice occurs over much of that same growth region, moving the ice into the warmer waters southwest of the marginal ice zones where significant basal/lateral melting occurs (Figure 2.5e). In Figure 2.5a, two hot spots of ice volume increase occur due to the blockage of transport by land, one northeast of St Lawrence Island, and one in the southwestern Gulf of Anadyr, and consequently ice thickness reaches a maximum there (Figure 2.11f). In the coastal polynya regions of the northern Bering Sea, the thermodynamic ice growth in Figure 2.5c and dynamical ice export in Figure 2.5b are very nearly in balance. In the central Bering Sea near the ice edge, significant ice volume increase still occurs (Figure 2.5a), with more ice volume being transported in (Figure 2.5b) than is melted (Figure 2.5c).

In spring (Figure 2.6), as the ice retreats, the volume tendency is negative everywhere as the ice cover decreases, as shown in Figure 2.6a. Although the growth rate is still positive in the higher latitude region (Figure 2.6d), the basal/lateral melt rate (Figure 2.6e) is high, especially in the southwestern Bering. The net thermodynamic tendency (Figure 2.6c) indicates a loss of ice everywhere except in small coastal and island regions in the northern Bering Sea. Strong ice transport out of the northern Bering Sea (Figure 2.6b) dominates the weak ice growth (Figure 2.6c), causing the net ice volume to decrease (Figure 2.6a). Although ice is transported into the southwest near the ice edge (Figure 2.6b), the local melting dominates (Figure 2.6e). Some relatively small surface melting occurs in the northwestern Gulf of Anadyr (Figure 2.6f).

In summer (Figure 2.7), there is only a small amount of ice with $\sim 5\%$ concentration along the coast of the Gulf of Anadyr. The little remaining ice in this region decreases (Figure 2.7a) due to basal/lateral melt effects (Figure 2.7e) along with weak surface melting (Figure 2.7f) and dynamical transport (Figure 2.7b) as it breaks apart.

Note that the surface melt term is very small in all seasons in the Bering Sea (Figure 2.4f, 2.5f, 2.6f and 2.7f). This is because there is essentially no ice

in the Bering Sea in summer, even though this term becomes significant in other regions of the Arctic Ocean due to air temperatures above the melting point. Issues associated with the CICE treatment of melt ponds on sea ice (Flocco et al., 2012) are therefore not expected to be relevant in this region.

This analysis of ice volume tendencies reveals large differences for the northern region, which is dominated by ice growth and ice outflow in winter, versus the southern region, which is dominated by melting and ice inflow. To display the seasonal evolution of this basic structure, spatial averages of the tendency terms were computed for two boxes (Figure 2.1), one in the northern ice growth region (a $90km \times 60km$ box centered at 63.76° N, 173.01° W) and one in the southern ice melt region (a $127km \times 100km$ box centered at 60.89° N, 178.31° W), for each month of the year (Figure 2.8). Ice growth dominates the thermodynamic tendency in the northern box from December to April, after which basal/lateral melting becomes the most significant term until summer when both tendencies are effectively zero. Ice transport out of the northern box is strongly negative and keeps the ice volume tendency close to zero though slightly positive throughout the winter months. In the southern box, the reverse happens in winter months. A strong dynamic influx of ice occurs from February through May, with a maximum in March, while substantial bottom melting nearly balances that input, resulting in a weak positive net ice volume tendency in winter and a weak negative value in spring. From May through July, when the ice edge moves near the northern box, the average in the northern box behaves like an attenuated version of the southern box.

Next we consider the total ice volume tendency summed over all the grid cells in the Bering Sea, which represents the time rate of change of total ice volume in the Bering Sea. Monthly climatological rates are shown in Figure 2.9. The time rate of change of total ice volume becomes positive from November and reaches its annual maximum positive value in January. During February and March, the rate is still positive but lower than the January maximum. It becomes negative in April and the ice retreat is greatest in May. The seasonal cycle of total ice volume tendency is dominated by the thermodynamic tendency. The contribution

of the dynamic tendency is relatively small. This dynamic tendency is positive only in November, and is negative from December to July and it attains its most negative value in April. During the winter months (December - March), the dynamic tendency and thermodynamic tendency have opposite signs; hence the dynamic tendency reduces the gains by the thermodynamic tendency. During spring (April-July) and fall (November) months, the dynamic tendency and thermodynamic tendency have the same sign, producing enhanced losses of ice in the spring and enhanced gains of ice in the fall.

2.5 Relationship between sea ice variability and atmospheric and oceanic conditions

2.5.1 Covariability of ice with atmosphere-ocean fields

While the terms in the ice volume tendency equation give us a picture of the overall processes at work in creating, transporting, and melting ice, they do not clearly differentiate between the various driving factors in the atmospheric and oceanic system. For example, although ice is transported laterally from the north to the south in winter, the transport could be due to direct wind forcing or to advection by ocean currents. In this section, we address the relationship between ice variables and large-scale and regional-scale patterns in the winds, surface air temperature, ocean currents, and sea surface temperature.

The major ocean currents in the Bering Sea are shown in Figure 2.10. The Alaska Stream flows westward along the southern side of the Aleutian Islands, enters the Bering Sea through several Aleutian Passes, and then flows eastward along the northern side of the Aleutian Islands. The Bering Sea basin is dominated by a cyclonic gyre. The Bering Slope Current flows northwestward along the shelf break with many eddies and meanders. Then the Bering Slope Current splits into Kamchakta Current to the west and Anadyr Current to the northeast. Finally, Anadyr Current Water in the west, Bering Shelf Water in the middle, and Alaska Coastal Current Water in the east move through the Bering Strait into the Arctic

Ocean.

In the fall season, northwestward ocean flow over the Bering shelf causes the SST to be warmer in the northwestern shelf than in the northeast, as shown in Figure 2.11i. As cold northerly winds blow (Figure 2.11a), ice forms most actively along the northern coastal regions of the Bering Sea. Ice also forms over the eastern, cooler part of the asymmetric SST pattern in the open ocean region of the northeastern shelf (Figure 2.11i). From there ice is transported southwestward (Figure 2.11e) by the very strong northeasterly winds (Figure 2.11a) to the warmer SST region, where ice melts (Figure 2.11i). This creates a very broad marginal ice zone (Figure 2.3a), in contrast to winter conditions where the transition is sharp near the ice edge (Figure 2.3b).

In the winter season, the ice typically moves southwestward, and maximum velocities occur along the western ice edge (Figure 2.11f). The wind field in winter (Figure 2.11b) over the ice covered Bering Sea exhibit strong northeasterly flow, which is consistent with wind-forced transport of the ice with a small rotation angle to the right. The wind strength is somewhat greater towards the western Bering ice-covered area (Figure 2.11b), which renders the surface wind stress on the ice (not shown) greater there than in the east. The net result is transport of ice from the northern region, where it is generated locally mostly by coastal polynyas opened by the northerly winds, to the southwestern ice covered area, where it is melted along the ice edge. The stress of the ocean on the ice (not shown) is slightly weaker than the wind stress on the ice and acts in the opposite direction. This, combined with the ocean currents tending to flow westward under the ice covered central region (Figure 2.11j), implies weak effects of large-scale oceanic advection of ice in this season.

Ocean currents do appear to play a substantial role in creating the asymmetry in the ice edge during winter, when the ice edge penetrates further southward in the east than in the west. As shown in Figure 2.11j, the Bering Slope Current carries warmer surface water from the southeastern Bering region to the western edge of the ice-covered area where melting occurs at higher latitudes than in the east (Figure 2.5e). Ocean-ice heat flux in winter (not shown) reveals strong warm-

ing of ice along the western ice edge, which results in the large basal ice melting seen in Figure 2.5e. The melting in this region occurs under the ice far from the ice edge, possibly due to the lateral mixing effects of very energetic oceanic eddies that occur along the Bering Slope Current. It is also likely that stronger winds and faster ice movement along the western ice edge induce stronger oceanic mixing. This is in contrast to the eastern ice edge, where basal melting is strongest very close to the ice edge.

Air temperature (Figure 2.11b) correlates well with ice concentration (the black line is the 15% ice concentration contour). Atmosphere-ice heat flux in winter (not shown) reveals substantial cooling in the northern Bering Sea near the coastal regions, where ice tends to be thinner than further offshore (Figure 2.11f). This is consistent with the idea that coastal polynyas form there due to the southward ice transport by the model northerly wind (Figure 2.11b and f). The largest growth rates occur along the northern coastal regions as seen in Figure 2.5d, probably associated with the fact that the thinner ice around the coastal polynyas grows faster (due to the conductive heat flux being approximately inversely related to the ice thickness).

In spring, sea ice volume decreases throughout the ice-covered region. Ice is still produced in the north, where the air temperature (a specified forcing) is consistently less than 0° C (Figure 2.11c). As shown in Figure 2.11g, north of St Lawrence Island, ice is transported northward through the Bering Strait into the Arctic likely by the influence of the ocean stress induced by the Anadyr Current (Figure 2.11k). In the broader regions south of St Lawrence Island, ice moves westward (Figure 2.11g) following the combined effects of weak northeasterly winds (Figure 2.11c) and the northwestward ocean currents (Figure 2.11k). Along the western parts of the ice edge, very strong basal and lateral melt driven by strong ice-ocean heat fluxes consumes ice transported into this region. From there, the Bering Slope Current carries ice towards the coast, where the Kamchatka Current transports the ice across Shirshov Ridge and along the coast of the Kamchatka Peninsula (Figure 2.11g and k). Along the eastern edge of the Bering Shelf, there is less ice near the coast (Figure 2.11g) associated with warmer air temperatures

(Figure 2.11c).

In summer, there is almost no ice in the Bering Sea. Only a very small amount of ice exists along the coast of the Gulf of Anadyr (Figure 2.3d). Basal/lateral melt from the warm ocean surface (Figure 2.11l) and weak surface melt from warm air (Figure 2.11d) occur there. Ice moves northeastward through the Anadyr Strait and Bering Strait (Figure 2.11h) following the ocean currents (Figure 2.11l).

2.5.2 Local forcing of sea ice variability

Now we consider the local forcing of the seasonal cycle of ice volume change for two sites in the northern ice growth region and in the southern ice melt region in section 2.4 (the two sites are marked on Figure 2.1). First we consider thermal forcings: surface heat flux between the atmosphere and the ice, and oceanic heat flux between the ocean and the ice. Positive heat flux is towards the ice. The formulae for calculating the surface heat fand oceanic heat fluxes are described in Appendix. As shown in Figure 2.12, in the north, the seasonal mean surface heat flux correlates well with the seasonal cycle of thermodynamic tendency (Figure 2.8 and Figure 2.12); in the south, oceanic heat flux climatology coincides with the seasonal thermodynamic ice volume tendency (Figure 2.8 and Figure 2.12). Second we consider the mechanical forcing: wind stress and ocean stress. The wind stress agrees with the seasonal dynamic ice volume tendency in general (Figure 2.8 and Figure 2.12). In all, on a seasonal basis, the thermodynamic ice volume change in the north is dominated by ice growth, which is driven by surface heat flux between the ice and the atmosphere; along the southern ice edge, ice thermodynamics is mainly basal melt driven by the ocean heat flux into ice. The dynamic ice transport is largely associated with wind stress.

2.5.3 Sea ice heat budget

We also examine the seasonal mean heat budget for sea ice. Net surface heat flux between the ice and the atmosphere is the sum of net shortwave radiation, net longwave radiation, latent heat flux and sensible heat flux. Latent heat flux

is the flux of heat between the ice and the atmosphere that is associated with sublimation of ice or deposition of water vapor. Sensible heat flux is the flux of heat associated with the difference between air potential temperature and the surface temperature of snow or snow-free ice. Oceanic heat flux is associated with the difference between sea surface temperature and freezing temperature.

As shown in Figure 2.13a, the climatological winter mean net surface heat flux is very large in the northern Bering Sea, with the largest heat loss from the ice to the atmosphere occurring in the coastal regions. As shown in Figure 2.13d, the heat flux from the ocean to the ice dominates the southwestern ice cover, with the largest values occurring along the western ice edge due to the warm Bering Slope Current that flows from the southeast into this region. Among the components of the net surface heat flux, sensible heat flux and net longwave radiation are important, while the net shortwave radiation and latent heat flux are insignificant. Sensible heat flux is large in coastal regions, and is hence largely responsible for the co-located extreme net surface heat flux (Figure 2.13f). Net longwave radiation contributes to the net surface heat flux on an overall basin scale (Figure 2.13e). In spring, the ocean heat flux acts over a large area especially in the western ice-covered area (Figure 2.13j). There is very weak net surface heat flux in the north (Figure 2.13g), as a result of relatively strong net shortwave heating (Figure 2.13h) and net longwave cooling (Figure 2.13k), weak sensible heat warming in the south and cooling in the north (Figure 2.13l), and very weak latent heat warming in the north (Figure 2.13i).

2.5.4 Sea ice force balance

In this section we quantify the sea-ice force balance in the Bering Sea to understand how the dominant balance changes between winter and spring. The momentum equation for sea ice consists of five stresses on the ice: wind stress, ocean stress, internal ice stress, Coriolis stress, and stress due to sea surface slope.

$$m\frac{\partial \mathbf{u}}{\partial t} = \overrightarrow{\tau_a} + \overrightarrow{\tau_w} + \nabla \cdot \sigma - \hat{k} \times mf\mathbf{u} - mg\nabla H_0 \tag{2.5}$$

where m is the combined mass of ice and snow per unit area, $\overrightarrow{\tau_a}$ and $\overrightarrow{\tau_w}$ are the wind stress on ice and the ocean stress on ice, $\nabla \cdot \sigma$ is the internal ice stress, $-\hat{k} \times mf\mathbf{u}$ is the stress due to Coriolis effects, and $-mg\nabla H_0$ is the stress due to sea surface slope (sea surface height H_0 is relative to the geoid). Monthly mean wind stress on the ice, ocean stress on the ice, internal ice stress, Coriolis stress are archived in the model output. We reconstruct the stress due to sea surface slope, based on model outputs of sea surface height, ice thickness, and snow thickness.

The magnitudes of wind stress on the ice, ocean stress on the ice, stress due to Coriolis effects, internal ice stress, stress due to sea surface slope, and their sum in winter and spring are compared in Figure 2.14a-f and Figure 2.15a-f. In winter, the wind stress and the ocean stress are very large and have similar magnitudes and spatial distribution; the ocean stress is slightly weaker than the wind stress especially near the coasts, as shown in Figure 2.14a,b. The internal ice stress (Figure 2.14d) is very large in the southern part of the Gulf of Anadyr and north of St Laurence Island, and is small in the central and southern ice-covered area. The Coriolis stress (Figure 2.14c) and the stress due to the sea surface slope (Figure 2.14e) are the smallest among these stress terms, but the stress due to sea surface slope is significant in some local spots near land e.g. near the Bering Strait (Figure 2.14e). These five stresses balance with nearly zero net stress everywhere in the Bering Sea (Figure 2.14f), indicating that sea ice motion is in quasi-steady state. In spring, wind stress and ocean stress are much smaller than in winter, and they attain their maximum values in the western ice-covered area, as shown in Figure 2.15a,b. The ocean stress is generally weaker than the wind stress. The internal ice stress (Figure 2.15d) is largely reduced, and is only important in the southern Gulf of Anadyr, immediately north of St Lawrence Island and near the Bering Strait, where its magnitude is similar to the magnitude of wind stress. The Coriolis stress (Figure 2.15c) and the stress due to sea surface slope (Figure 2.15e) are very weak. Sea ice is in almost perfect stress balance in spring (Figure 2.15f).

Since the largest two stresses (wind and ocean) are nearly counterbalancing each other (not shown), indicating wind-driven ice flow, with ocean drag, it is useful to examine the residual sum of these two terms in relation to the other (smaller)

stress terms. In Figure 2.14g-j and Figure 2.15g-j, we compare this residual sum to internal ice stress, Coriolis stress, and stress due to sea surface slope for winter and spring climatological means. The winter residual sum (Figure 2.14g) has a very similar magnitude and spatial distribution as internal ice stress (Figure 2.14i). Near the southern part of the Gulf of Anadyr and north of St Laurence Island, these two terms are very large (Figure 2.14g,i). In the southern and central ice covered area, though Coriolis stress (Figure 2.14h) is small, it is comparable with internal ice stress (Figure 2.14i) and the residual sum (Figure 2.14g). In spring, internal ice stress (Figure 2.15i) and the residual sum (Figure 2.15g) are weaker versions of those in winter. In the southern and central ice covered area, internal ice stress (Figure 2.15i), the residual sum (Figure 2.15g), and Coriolis stress (Figure 2.15h) have very similar magnitudes.

In summary, the wind stress is the largest stress, and the ocean stress is the second largest. These two stress terms have similar magnitudes and spatial distribution. The internal ice stress can be important at some local spots near the land boundaries in the north, and is small in the central and southern ice-covered area. The sum of wind stress and ocean stress has a very similar magnitude and spatial distribution to internal ice stress. Coriolis stress and the stress due to sea surface slope are small, but Coriolis stress has a magnitude close to internal ice stress and sum of wind stress and ocean along the ice edge. The sum of these five stresses is almost zero, producing nearly steady sea ice motion.

2.6 Summary and Discussion

We evaluated the skill, dynamic balances, and thermodynamic balances in 1/10-degree POP-CICE in regard to its representation of the seasonal cycle of sea ice in the Bering Sea for the time period 1980-89. We found good agreement between simulated and observed sea ice concentration in each season, except for a bias towards less ice than observed (cf. Danielson et al. (2011)). Since winter is the season with the greatest amount of sea ice, and since the annual-mean structure is most similar to that of winter, we present a schematic broad-scale depiction of the

dominant processes controlling Bering Sea ice structure in wintertime in Figure 2.16.

This schematic indicates how ice is created, transported and melted in winter. In the northern Bering Sea, the northeasterly wind brings cold air, which freezes the ocean surface, causing ice to grow there. The wind also opens coastal polynyas where the ice growth rate attains its maximum values. South of St. Lawrence Island, wind stress drives ice to move southwestward, so that ice is transported from the north to the southwestern ice-covered area (Pease, 1980; McNutt, 1981a,b). Along the southern ice edge, especially in the west, ice is melted by warm ocean water. These warm waters are carried by the Bering Slope Current flowing northwestward, resulting in the S-shaped asymmetric pattern seen in the ice edge. This general picture is consistent with a conveyor belt with the northern source, the southern sink, and the intermediate zone where ice is transported southward by northerly winds (Muench and Ahlnas, 1976; Pease, 1980).

We also examined the driving forcing of seasonal cycle of sea ice in the Bering Sea, including heat budget and force balance for sea ice. Seasonal thermodynamic ice volume change is dominated by surface heat flux between the atmosphere and the ice in the north, and by heat flux from the ocean to the ice along the southern ice edge especially on the western side. Sea ice motion is largely associated with wind stress. Internal ice stress is large near the land boundaries in the north, and is small in the central and southern ice-covered area.

The dynamic ice transport acts in opposition to the thermodynamic terms locally throughout the ice-covered months (Figure 2.8). As shown in the monthly climatology plot in Figure 2.8, dynamic tendency and thermodynamic tendency are opposite to each other with similar magnitudes, leaving a small residual net tendency of ice volume, both in the northern growth region and in the southwestern melt region. Yet dynamic ice transport also plays a role in enhancing the thermodynamic growth in the northern regions in winter as ice is transported out of the region where it is formed, which promotes further ice growth there. Likewise, ice is dynamically transported into the southern warmer ocean regions where it is melted, so that more ice transport contributes to a larger ice melt rate near

the ice edge. In winter, the process of ice growth, transport, and melt reaches its maximum when the strong northeasterly winds drive the strongest southwestward ice transport. However, integrated over the whole Bering Sea, the seasonal cycle of total ice volume tendency is dominated by the thermodynamic tendency, and the contribution of the dynamic tendency is relatively small, as shown in Figure 2.9.

The thermodynamic and dynamic tendencies of ice volume exhibit opposite-signed dipole patterns in their spatial distributions (Figure 2.4 2.5 2.6 2.7). The 1980-89 annual-mean net ice volume tendency reveals that these two terms are nearly in balance everywhere. Overall, thermodynamic volume changes dominate in the north in fall and winter through producing ice, and they also dominate in the southwest in spring through melting ice. Dynamic changes dominate the ice volume increase near the western ice edge in fall and winter through ice influx, as well as the ice volume decrease in the north in spring through ice transport out of the northern region.

The dynamic balance is largely associated with the wind forcing, while the thermodynamic balance involves several aspects of the atmospheric and oceanic system. Polynyas occur along the coast in the north produced by northerly winds, and cold air temperature promotes ice growth in the northern Bering Sea. The Bering Slope Current brings warm water northwestward towards the western ice edge where wind-driven ice import occurs, and ice melts there significantly. This competition of the atmospheric wind and the ocean current largely controls the S-shaped structure of the ice edge location.

The thermodynamic and dynamic balances presented in this paper are broadly consistent with other studies. Bitz et al. (2005) show a very similar spatial distribution of thermodynamic and dynamic ice volume tendencies in winter. Zhang et al. (2010) show less east-west asymmetry in thermodynamic volume changes in winter, though their north-south distribution of growth and melt and dynamic ice transport in winter broadly agree with our results. Zhang and Rothrock (2001) show that the dynamic and thermodynamic effects of sea ice in the Arctic Ocean are also opposite.

Our analysis has demonstrated the skill of POP-CICE in representing the observed seasonal cycle of sea ice concentration in the Bering Sea during 1980-1989. The model allows a clear depiction of the important balances controlling the sea ice variability. Further work is needed to evaluate the anomalous characteristics of sea ice evolution in this region, including the impacts of anomalous winds, surface heat fluxes, fluctuating currents and mesoscale eddy effects, which will be the topic of a future study.

Acknowledgments

Funding was provided by NSF (OCE-0960770) and DOE (DE-FG0205ER641 19). The ocean/sea-ice simulation was conducted using computer resources provided by the Climate Simulation Laboratory at NCAR's Computational and Information Systems Laboratory, sponsored by the National Science Foundation and other agencies.

Chapter 2 is in preparation for submission to Ocean Dynamics. Linghan Li, Julie L McClean, Arthur J Miller, Ian Eisenman, and Myrl C Hendershott, 2013. The dissertation author was the primary investigator and author of Chapter 2.

References

Bitz, Cecilia M and Lipscomb, William H. An energy-conserving thermodynamic model of sea ice. *Journal of Geophysical Research: Oceans (1978–2012)*, 104 (C7):15669–15677, 1999.

Bitz, CM, Holland, MM, Hunke, EC, and Moritz, RE. Maintenance of the sea-ice edge. *Journal of climate*, 18(15):2903–2921, 2005.

Comiso, J. Bootstrap sea ice concentrations from nimbus–7 smmr and dmsp ssm/i–ssmis, version 2, 2000.

Danielson, Seth, Curchitser, Enrique, Hedstrom, Kate, Weingartner, Thomas, and Stabeno, Phyllis. On ocean and sea ice modes of variability in the bering sea. *Journal of Geophysical Research: Oceans (1978–2012)*, 116(C12), 2011.

Griffies, Stephen M and Greatbatch, Richard J. Physical processes that impact the evolution of global mean sea level in ocean climate models. *Ocean Modelling*, 51:37–72, 2012.

Hunke, EC and Dukowicz, JK. An elastic-viscous-plastic model for sea ice dynamics. *Journal of Physical Oceanography*, 27(9):1849–1867, 1997.

Hunke, Elizabeth, Maltrud, Mathew, and Hecht, Matthew. On the grid dependence of lateral mixing parameterizations for global ocean simulations. *Ocean Modelling*, 20(2):115–133, 2008.

Hunt, George L, Coyle, Kenneth O, Eisner, Lisa B, Farley, Edward V, Heintz, Ron A, Mueter, Franz, Napp, Jeffrey M, Overland, James E, Ressler, Patrick H, Salo, Sigrid, and others, . Climate impacts on eastern bering sea foodwebs: a synthesis of new data and an assessment of the oscillating control hypothesis. *ICES Journal of Marine Science: Journal du Conseil*, 68(6):1230–1243, 2011.

Ivanova, Detelina P, McClean, Julie L, and Hunke, Elizabeth C. Interaction of ocean temperature advection, surface heat fluxes and sea ice in the marginal ice zone during the north atlantic oscillation in the 1990s: A modeling study. *Journal of Geophysical Research: Oceans (1978–2012)*, 117(C2), 2012.

Johnson, Gregory C, Stabeno, Phyllis J, and Riser, Stephen C. The bering slope current system revisited. *Journal of physical oceanography*, 34(2):384–398, 2004.

Large, William George and Yeager, Stephen G. The global climatology of an interannually varying air-sea flux data set *Climate Dynamics*, 33:341–364, 2009.

Maslanik, James A, Serreze, Mark C, and Barry, Roger G. Recent decreases in arctic summer ice cover and linkages to atmospheric circulation anomalies. *Geophysical Research Letters*, 23(13):1677–1680, 1996.

McClean, Julie L, Papadopoulos, Caroline, Yulaeva, Elena, and Bailey, David. High resolution CESM: A 40-year CORE forced global coupled 0.1-deg ocean/sea-ice simulation. CESM Workshop 2013, Breckenridge CO, June 2013.

McNutt, Lyn. Ice conditions in the eastern bering sea from noaa and landsat imagery: Winter conditions 1974, 1976, 1977, 1979. 1981a.

McNutt, S Lyn. Remote sensing analysis of ice growth and distribution in the eastern bering sea. *The eastern Bering Sea shelf: Oceanography and resources*, 1:141–166, 1981b.

Muench, RD and Ahlnas, K. Ice movement and distribution in the bering sea from march to june 1974. *Journal of Geophysical Research*, 81(24):4467–4476, 1976.

Parkinson, Claire L, Comiso, Josefino C, Zwally, H Jay, Cavalieri, Donald J, Gloersen, Per, and Campbell, Willaim J. *Arctic sea ice, 1973-1976: Satellite passive-microwave observations*, volume 489. Scientific and Technical Information Branch, National Aeronautics and Space Administration Washington, DC, 1987.

Pease, Carol H. Eastern bering sea ice processes. *Monthly Weather Review*, 108 (12):2015–2023, 1980.

Prasad, TG, McClean, Julie L, Hunke, Elizabeth C, Semtner, Albert J, and Ivanova, Detelina. A numerical study of the western cosmonaut polynya in a coupled ocean–sea ice model. *Journal of Geophysical Research: Oceans (1978–2012)*, 110(C10), 2005.

Stabeno, PJ, Bond, NA, Kachel, NB, Salo, SA, and Schumacher, JD. On the temporal variability of the physical environment over the south-eastern bering sea. *Fisheries Oceanography*, 10(1):81–98, 2001.

Wang, Jia, Hu, Haoguo, Mizobata, Kohei, and Saitoh, Sei-ichi. Seasonal variations of sea ice and ocean circulation in the bering sea: A model-data fusion study. *Journal of Geophysical Research: Oceans (1978–2012)*, 114(C2), 2009.

Wang, Muyin, Overland, James E, and Stabeno, Phyllis. Future climate of the bering and chukchi seas projected by global climate models. *Deep Sea Research Part II: Topical Studies in Oceanography*, 65:46–57, 2012.

Zhang, Jinlun and Rothrock, Drew. A thickness and enthalpy distribution sea-ice model. *Journal of physical oceanography*, 31(10):2986–3001, 2001.

Zhang, Jinlun, Woodgate, Rebecca, and Moritz, Richard. Sea ice response to atmospheric and oceanic forcing in the bering sea. *Journal of Physical Oceanography*, 40(8):1729–1747, 2010.

Table 2.1: Model-Observation comparison of seasonal mean values. Ice area and mean concentration (area/extent) are computed for ice concentration > 15% Rms error (normalized by Rms obs) and correlation are computed over the area where both model > 0% and obs > 0% (parenthetical values where either model > 0% or obs > 0%)

	Fall	Winter	Spring	Summer
Model Ice Area ($10^5 km^2$)	0.77	4.7	2.5	0.0076
Obs Ice Area ($10^5 km^2$)	1.0	5.5	2.6	.00007
Model Mean Ice Conc	0.44	0.78	0.55	0.26
Obs Mean Ice Conc	0.42	0.76	0.51	0.06
Rms error Ice Conc	0.43 (0.43)	0.16 (0.16)	0.22 (0.22)	4.9 (30.)
Correlation Ice Conc	0.81 (0.85)	0.97 (0.98)	0.94 (0.96)	-0.26 (0.03)

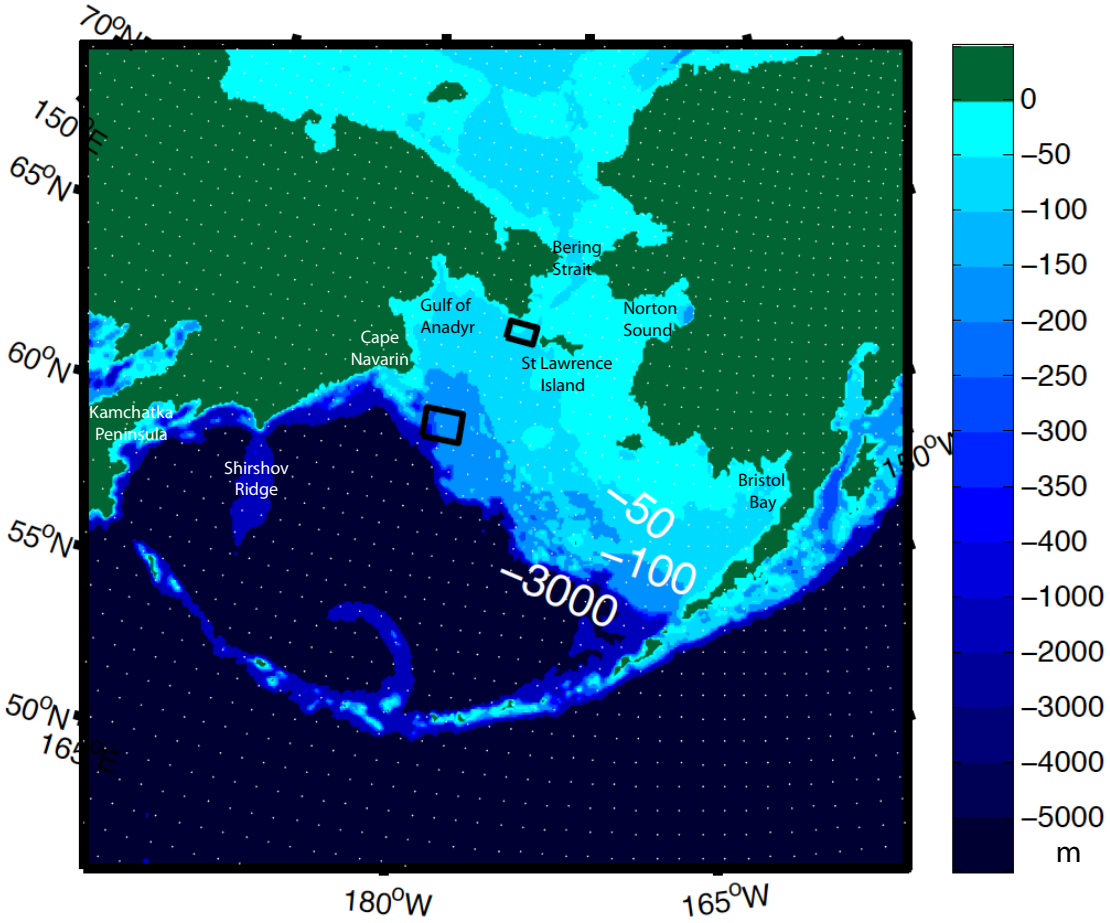

Figure 2.1: Bathymetry of the Bering Sea (contours) and the model T-grid points (white dots) subsampled every 10 points. The bathymetry is from POP-CICE model output of ocean depth at T-grid points. 2 black boxes show 2 study areas for Figure 2.8. Locations of places mentioned in the text are shown.

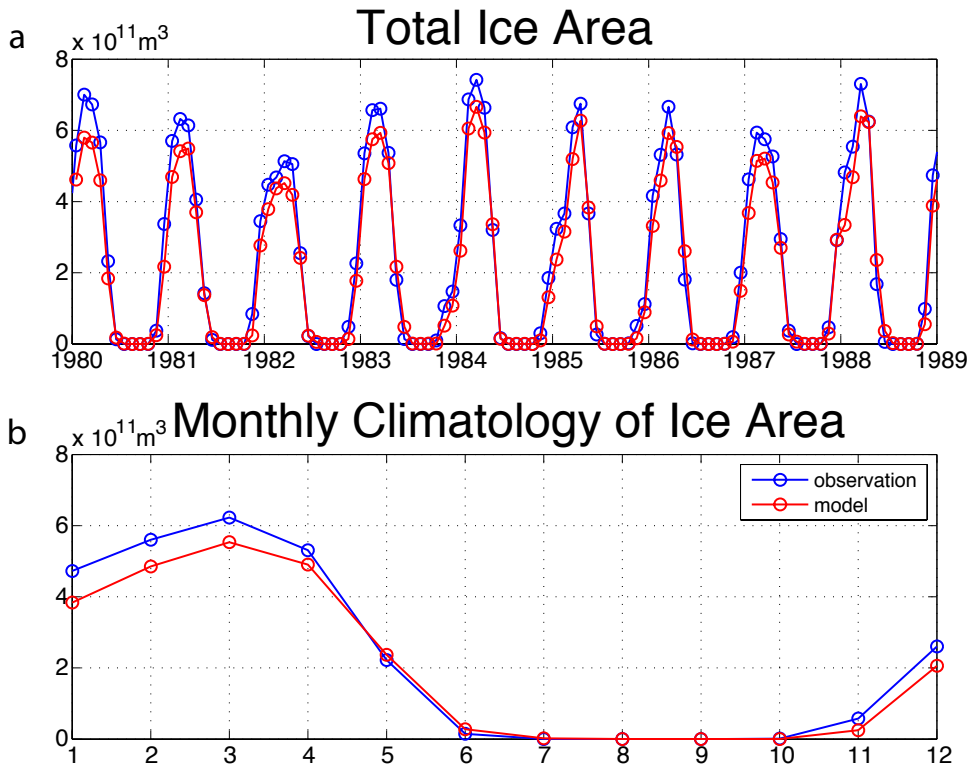

Figure 2.2: (a) Total ice area in the Bering Sea for POP-CICE model (red) and satellite passive microwave observations (blue) for each month (circles) from 1980-1989. Total ice area is computed as the sum of fractional ice coverage area in each grid cell for areas with ice concentration larger than 15%. (b) Monthly mean seasonal cycle of total ice area for model (red) and observations (blue).

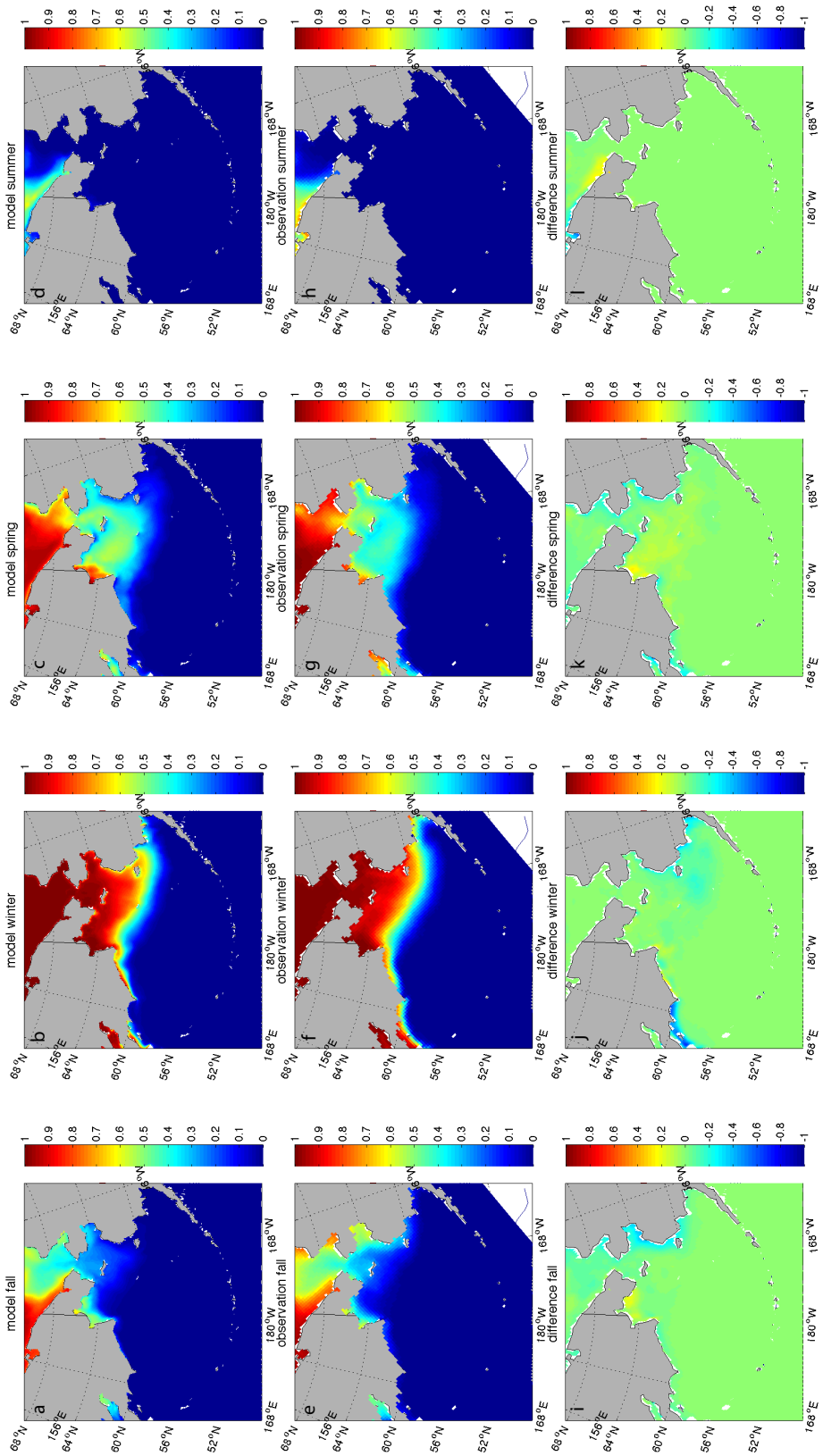

Figure 2.3: Ice concentrations from POP-CICE model (top a-d), Bootstrap satellite passive microwave observations (middle e-h), and difference between model and observation (bottom i-l). Seasonal means (fall, winter, spring and summer) of ice concentrations (1980-1989) from model and observation and their difference are shown from left to right.

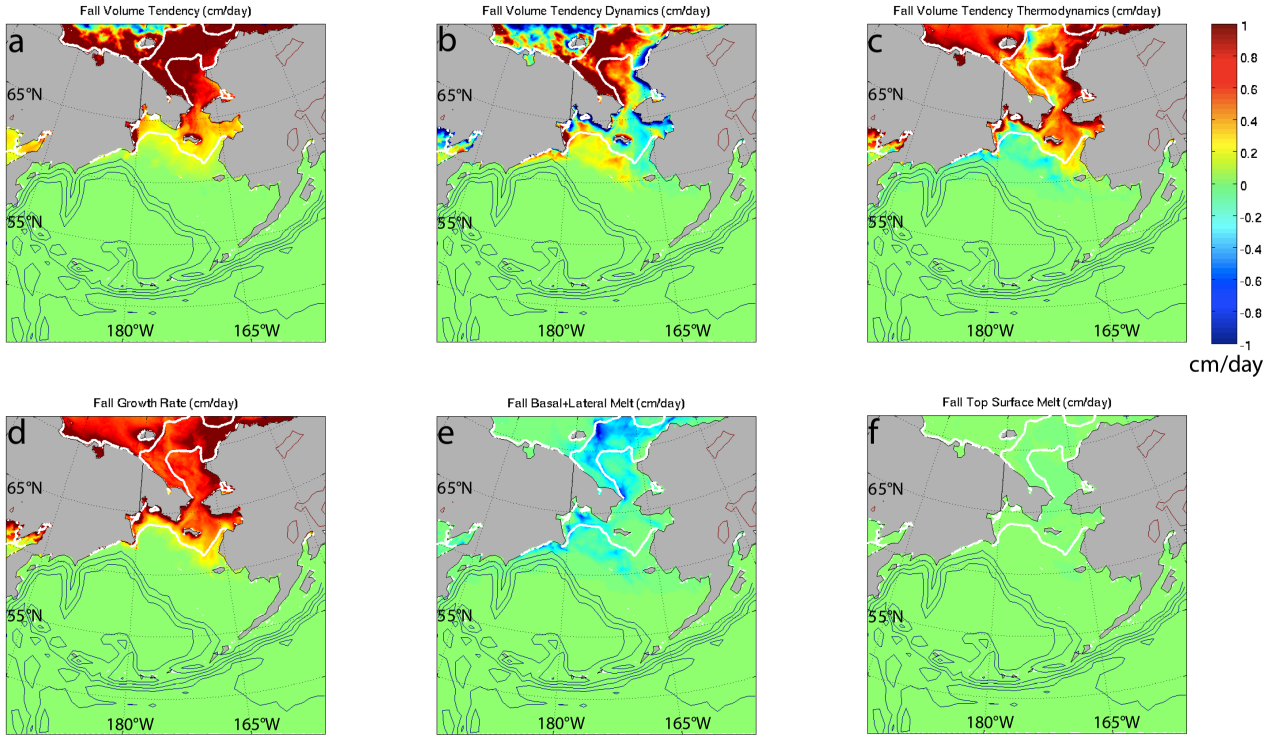

Figure 2.4: (a) Fall mean ice volume tendency $\frac{\partial V}{\partial t}$ (sum of dynamic tendency and thermodynamic tendency), (b) dynamic tendency $\frac{\partial V_D}{\partial t}$, and (c) thermodynamic (basal melt rate, lateral melt rate, plus surface melt rate) tendency $\frac{\partial V_T}{\partial t}$, (d) ice growth rate G (sum of frazil ice growth, congelation ice growth, and snow ice formation), (e) basal plus lateral melt rate M_{BL}, and (f) surface melt rate M_S. Note melt rates in (e) and (f) are depicted as negative values. White lines represent contours of 15%, 50%, and 85% ice concentrations. Volume is normalized by the grid cell area, giving units of thickness (cm) for each panel.

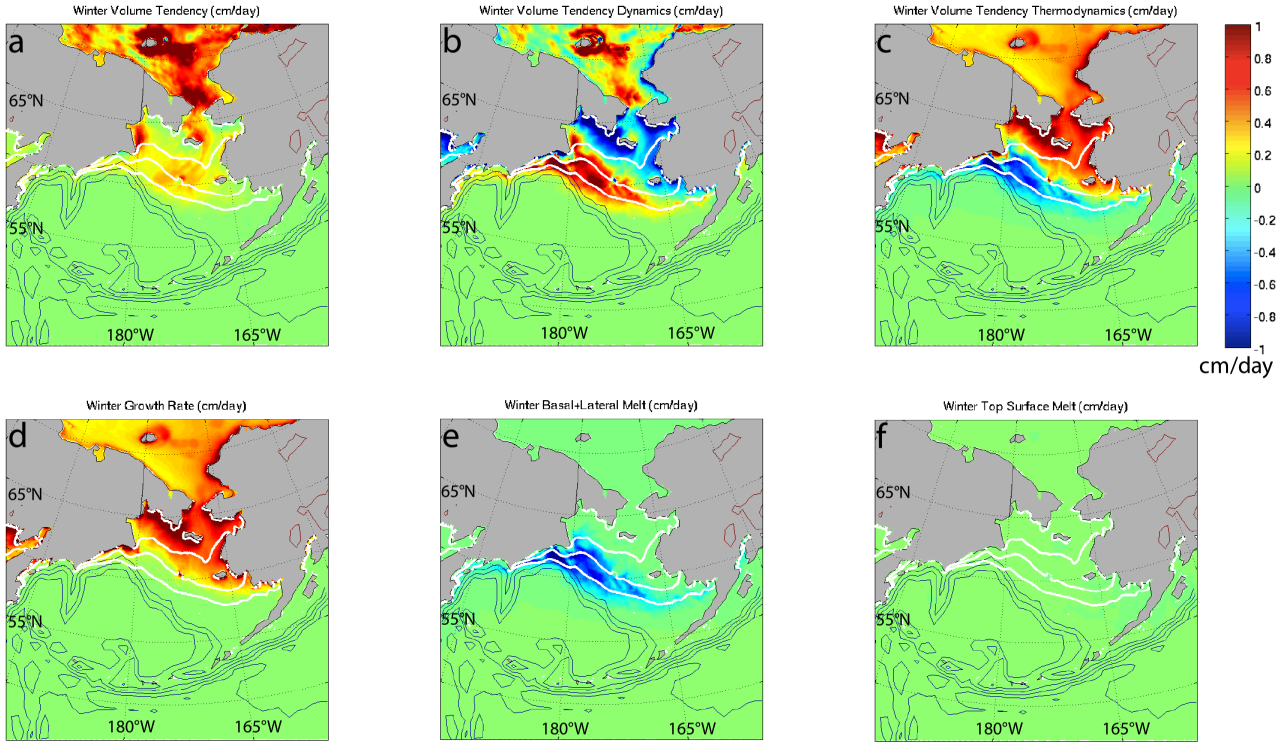

Figure 2.5: (a) Winter mean ice volume tendency $\frac{\partial V}{\partial t}$, (b) dynamic tendency $\frac{\partial V_D}{\partial t}$, and (c) thermodynamic tendency $\frac{\partial V_T}{\partial t}$, (d) ice growth rate G, (e) basal plus lateral melt rate M_{BL}, and (f) surface melt rate M_S. Note melt rates in (e) and (f) are depicted as negative values. White lines represent ice concentration contours of 15%, 50%, and 85%. Volume is normalized by the grid cell area, giving units of thickness (cm) for each panel.

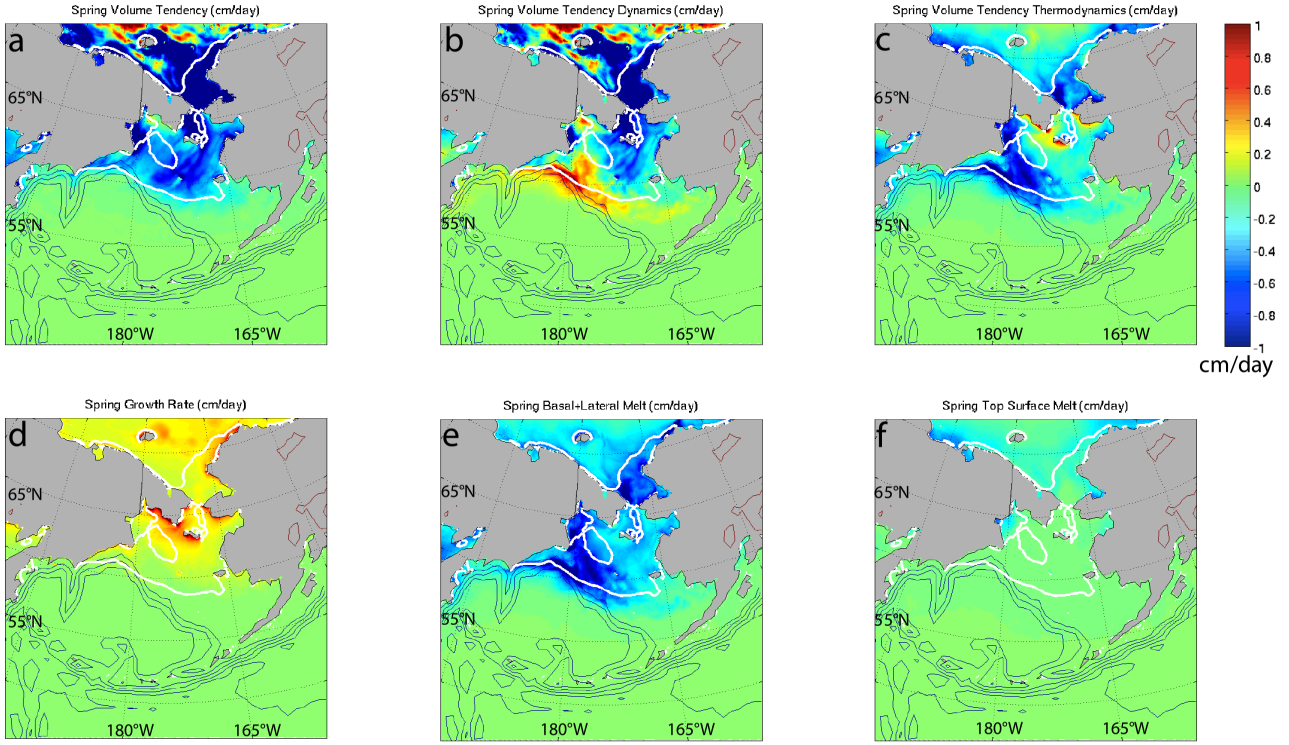

Figure 2.6: (a) Spring mean ice volume tendency $\frac{\partial V}{\partial t}$, (b) dynamic tendency $\frac{\partial V_D}{\partial t}$, and (c) thermodynamic tendency $\frac{\partial V_T}{\partial t}$, (d) ice growth rate G, (e) basal plus lateral melt rate M_{BL}, and (f) surface melt rate M_S. Note melt rates in (e) and (f) are depicted as negative values. White lines represent ice concentration contours of 15%, 50%, and 85%. Volume is normalized by the grid cell area, giving units of thickness (cm) for each panel.

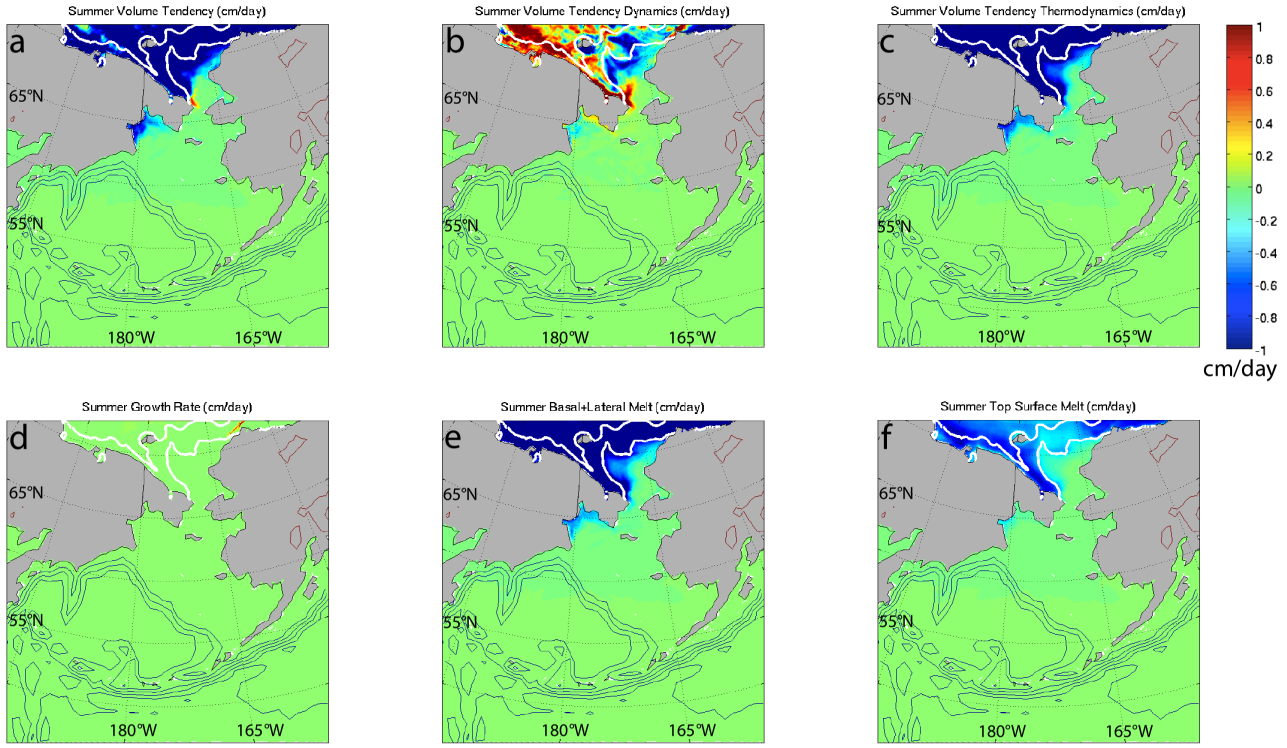

Figure 2.7: (a) Summer mean ice volume tendency $\frac{\partial V}{\partial t}$, (b) dynamic tendency $\frac{\partial V_D}{\partial t}$, and (c) thermodynamic tendency $\frac{\partial V_T}{\partial t}$, (d) ice growth rate G, (e) basal plus lateral melt rate M_{BL}, and (f) surface melt rate M_S. Note melt rates in (e) and (f) are depicted as negative values. White lines represent ice concentration contours of 15%, 50%, and 85%. Volume is normalized by the grid cell area, giving units of thickness (cm) for each panel.

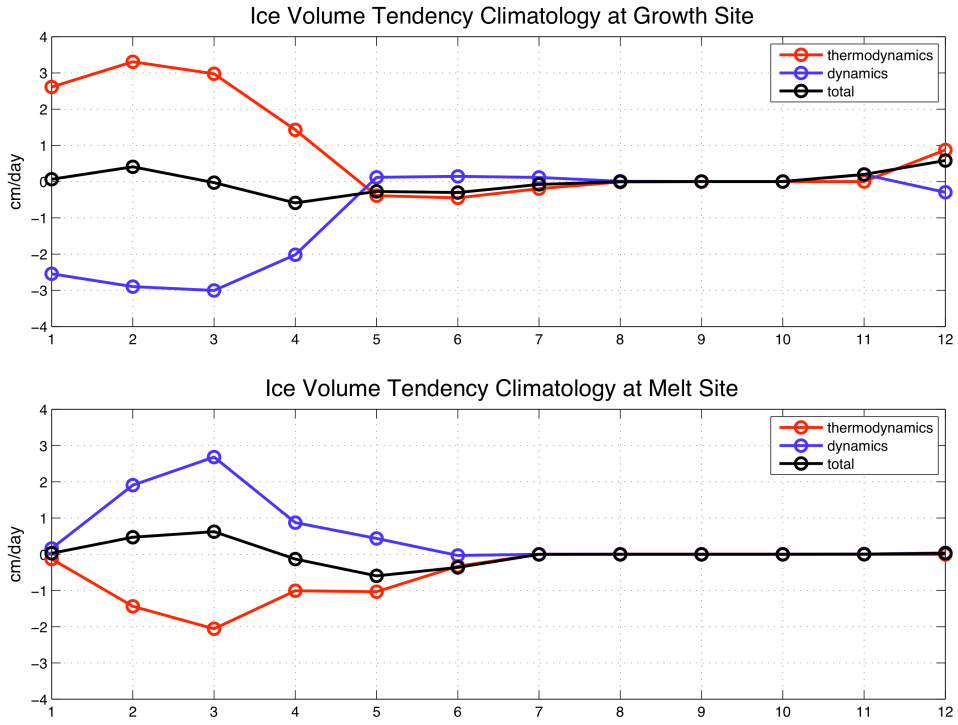

Figure 2.8: Monthly climatology of thermodynamic, dynamic, and total ice volume tendencies averaged in each of the 2 boxes (shown in Figure 2.1) in the key growth and melt areas.

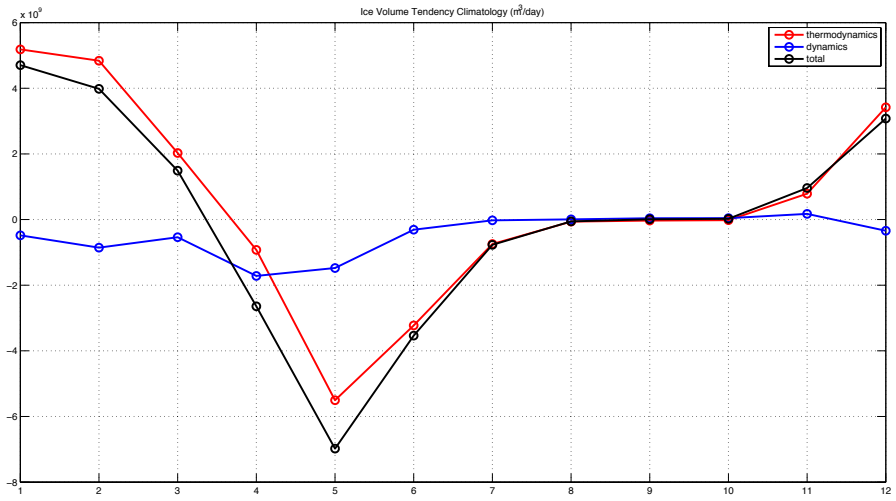

Figure 2.9: Monthly climatology of thermodynamic, dynamic, and total ice volume tendencies summed over all the grid cells in the Bering Sea.

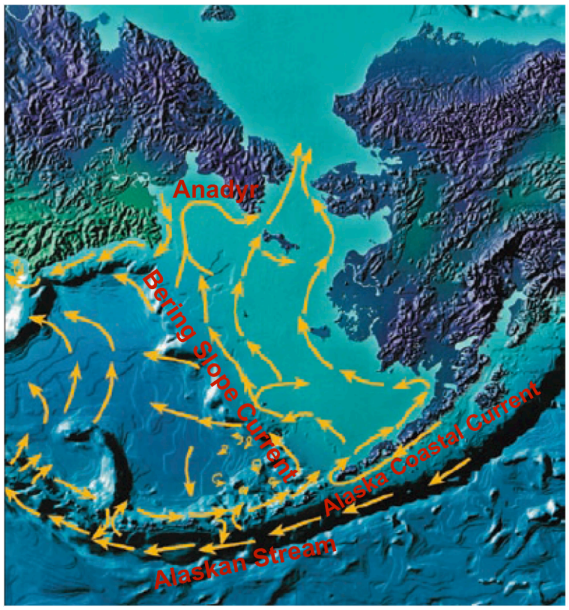

Figure 2.10: Major ocean currents in the Bering Sea (modified from Figure 30.4 of Stabeno et al., 1999a; image by Karen Birchfield, NOAA Pacific Marine Environmental Laboratory).

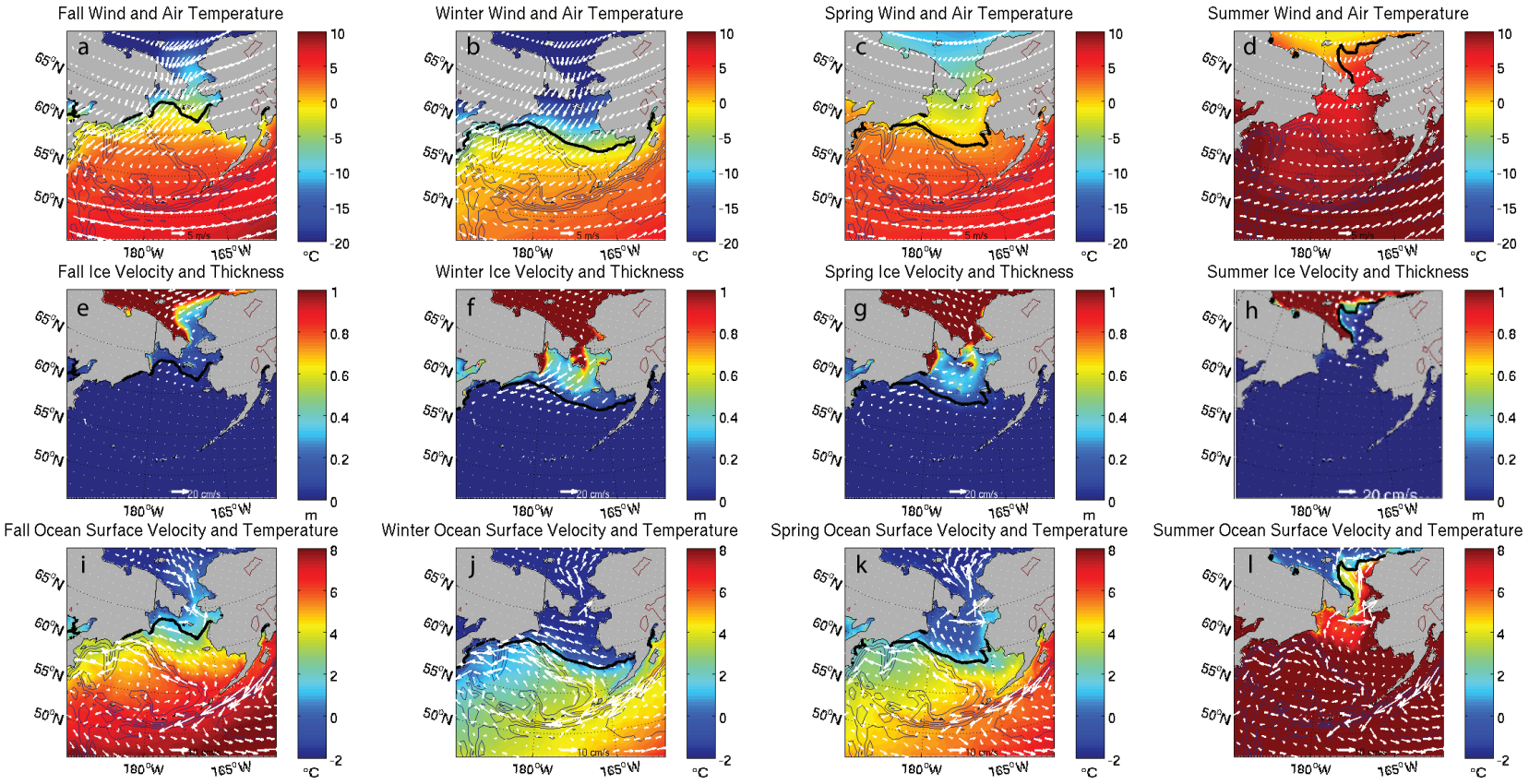

Figure 2.11: Seasonal mean of (top a-d) atmospheric wind and temperature, (middle e-h) ice velocity and thickness, and (bottom i-l) ocean surface velocity and temperature for (left to right) fall, winter, spring and summer. 15% ice concentration contour is shown in black.

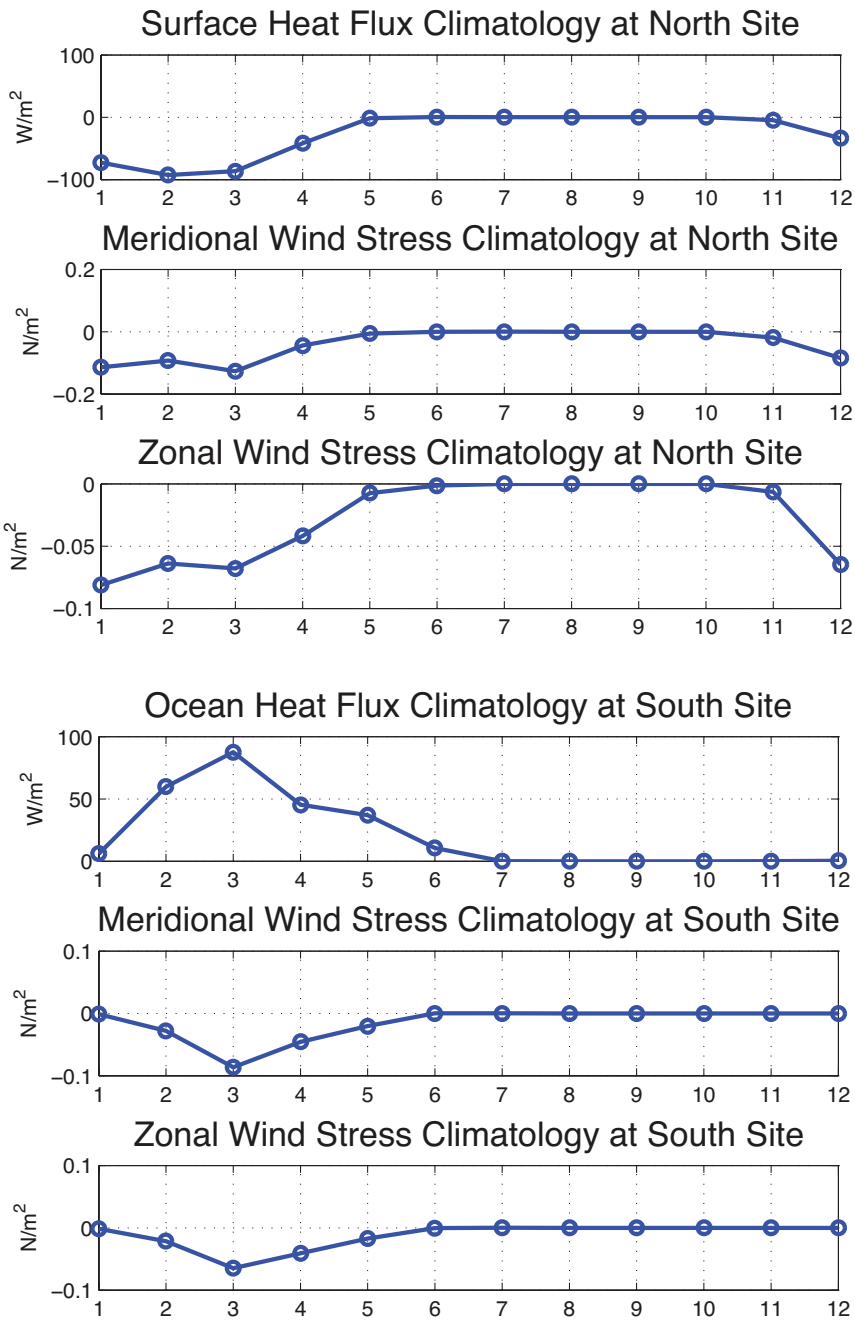

Figure 2.12: Monthly climatology of surface/ocean heat flux and wind stress on ice averaged in 2 boxes in the north and in the south (shown in Figure 2.1).

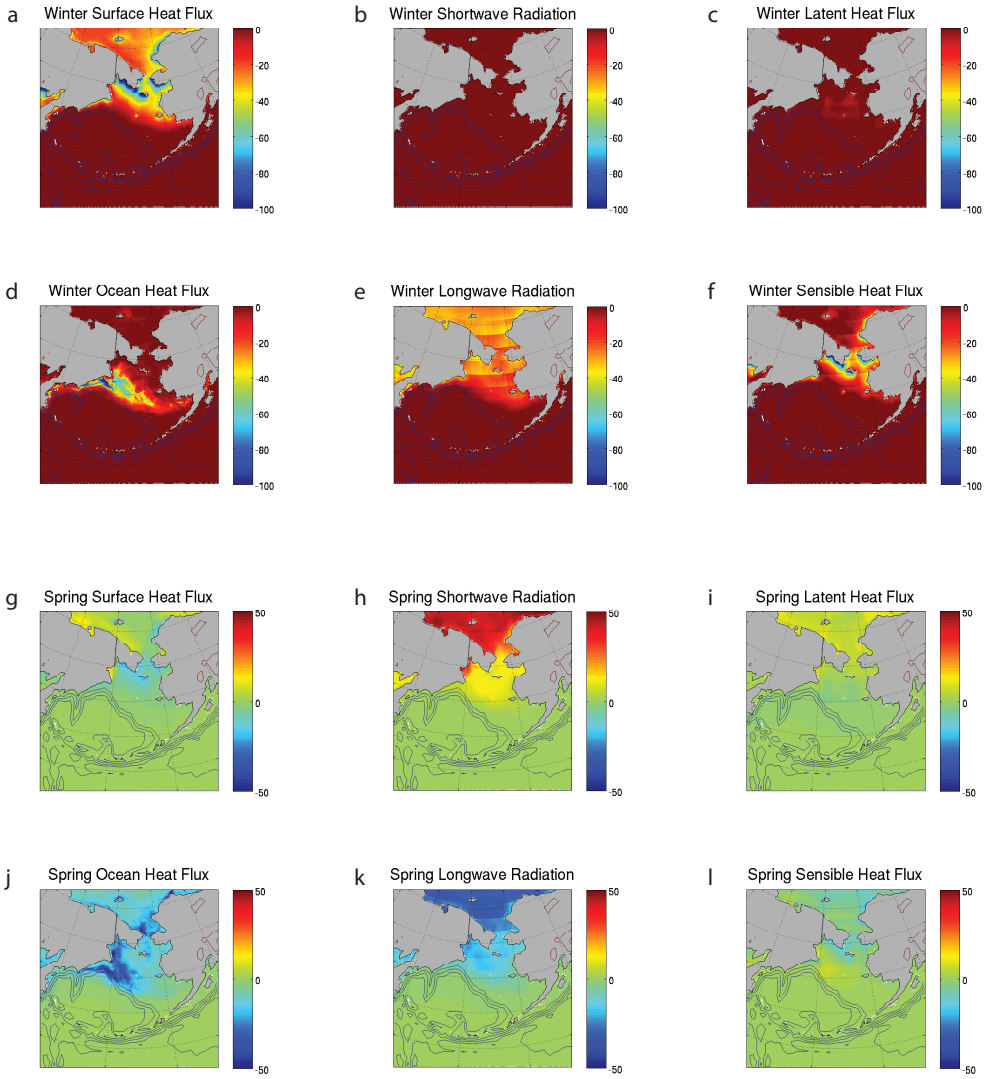

Figure 2.13: (a) Winter net surface heat flux, (b) winter net shortwave radiation, (c) winter latent heat flux, (d) winter ocean heat flux, (e) winter net longwave radiation, (f) winter sensible heat flux, (g) spring net surface heat flux, (h) spring net shortwave radiation, (i) spring latent heat flux, (j) spring ocean heat flux, (k) spring net longwave radiation, (l) spring sensible heat flux. The positive heat flux is downward.

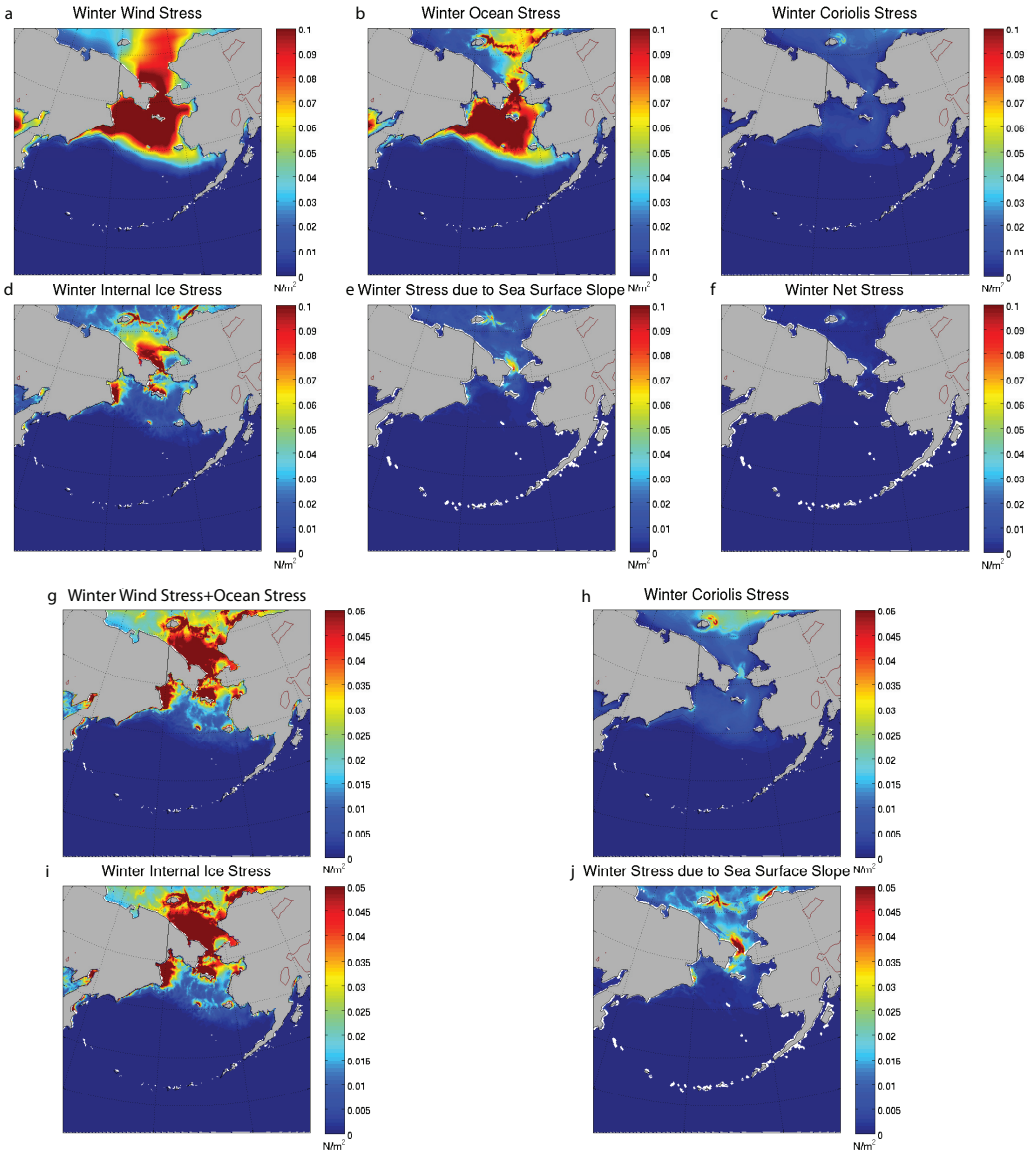

Figure 2.14: Magnitudes of winter wind stress on ice (a), ocean stress on ice (b), Coriolis stress (c), internal ice stress (d), stress due to sea surface slope (e), and net stress (f). Magnitudes of sum of wind stress and ocean stress (g), Coriolis stress (h), internal ice stress (i), and stress due to sea surface slope in winter (j).

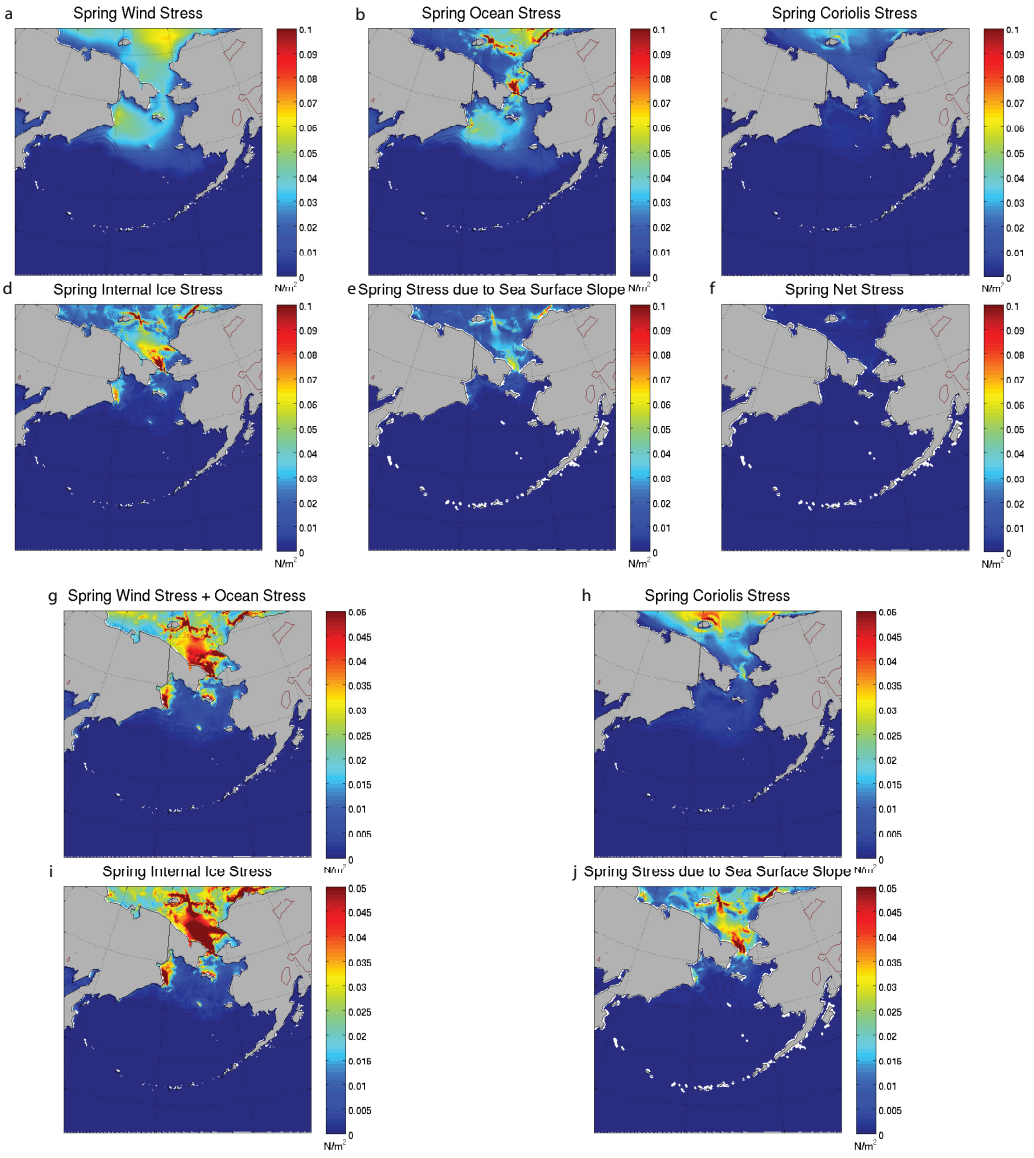

Figure 2.15: Magnitudes of spring wind stress on ice (a), ocean stress on ice (b), Coriolis stress (c), internal ice stress (d), stress due to sea surface slope (e), and net stress (f). Magnitudes of sum of wind stress and ocean stress (g), Coriolis stress (h), internal ice stress (i), and stress due to sea surface slope in spring (j).

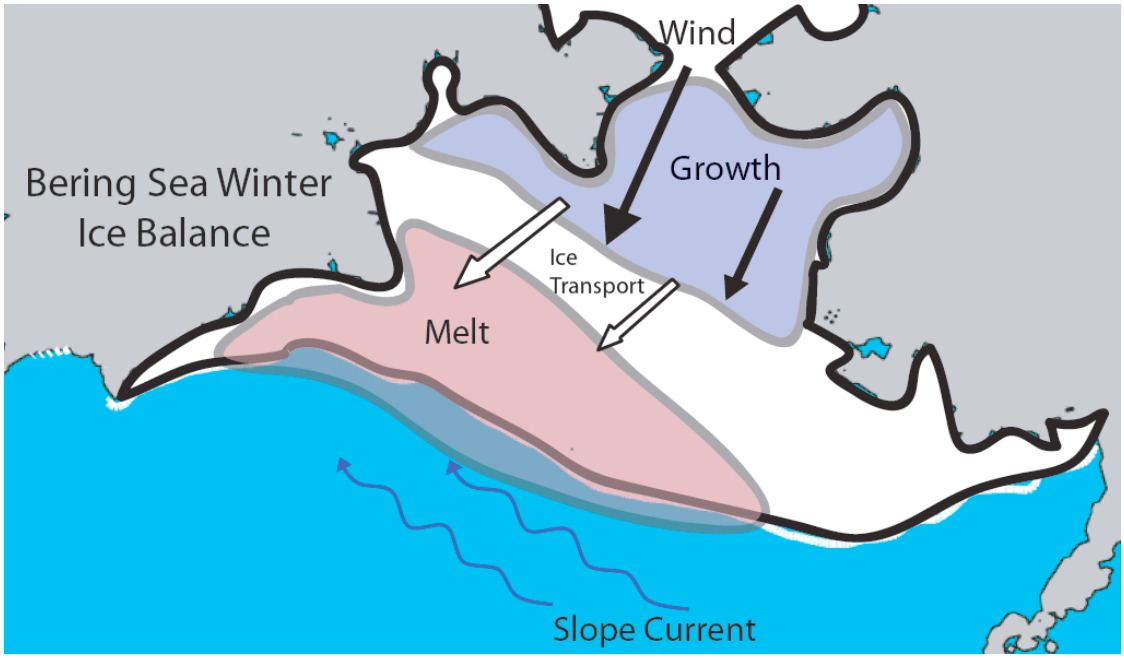

Figure 2.16: Schematic of the large-scale Bering Sea winter sea ice balance summarizing our results. Cold northeasterly wind (black arrows) drives the strongest ice growth (lavender) in the northeast. Ice moves (white arrows) southwestward towards the strongest melting region (rose), which is warmed by the Bering Slope Current (blue arrows). These patterns drive the basin-wide asymmetry and the S-shaped ice edge. The modeled winter sea ice balance is shown in **Figure 2.5.**

Chapter 3

Thermodynamic and Dynamic Controls on Sea Ice Variability in the Bering Sea

A high-resolution (0.1 degree) ocean-sea ice model (POP-CICE) is compared with observations and studied to determine the basin-scale and local balances controlling the variability of sea ice in the Bering Sea in the time period 1980-1989. The model produces variations in total ice area anomalies that are highly correlated with observations. The corresponding variations in the model ice volume are largely controlled by thermodynamic forcing by surface heat flux, which in turn is dominated by sensible heat flux. This indicates that surface air temperature, which is specified from observations in the CORE2 forcing, strongly controls the ice volume tendency in this simulation.

While thermodynamic processes dominate the variations in ice volume change in the Bering Sea on the large scale, dynamic processes are important on the local scale near ice margins (both oceanic and land), where dynamic and thermodynamic ice volume changes have opposite signs with large and similar amplitudes. The thermodynamic ice volume change is dominated by surface heat flux with the atmosphere, except near the southern ice edge where it is largely controlled by ocean-ice heat flux. Ice motion is generally consistent with winds driving the flow, except near certain straits in the north where ice motion largely follows ocean

currents. For example, the modeled climatological ice volume transport out of the Bering Strait for January-May, $146 km^3 yr^{-1}$, and its high month-to-month variability, are consistent with the range of published field measurements.

Two key climate events, strong ice growth with cold air temperature and northerly wind in Feb 1984 and weak ice growth with warm air temperature and southerly wind in Feb 1989, are studied in detail. While the processes controlling the ice changes are generally similar to those in other years, these events clearly reveal the characteristic spatial patterns of ice growth anomalies in the north accompanied by ice melt anomalies along the ice edge in the south, with dynamic anomalies transporting ice from the north to the south. These two climate events are associated with the position of the Aleutian Low, which appears to be regulated by local processes rather than broad-scale climate events.

3.1 Introduction

Seasonal sea ice cover plays a key role in physical-biological interactions in the Bering Sea. The advance and retreat of sea ice has a major influence on biological productivity and the marine ecosystem of the eastern Bering Sea by affecting light, water temperature and the availability of substrate. Furthermore, the Bering Sea is where Pacific Ocean water flows into the Arctic Ocean. Thus the sea ice and ocean conditions in the Bering Sea could affect the downstream Chukchi Sea and the Arctic Ocean, and may play a role in the recent precipitous decrease in summer ice there.

Sea ice in the Bering Sea exhibits significant seasonal, interannual and decadal variability. The seasonal variation of sea ice in the Bering Sea is large, with the seasonal range of the ice edge location in the south-north direction being as large as 1700 km. The maximum ice extent in winter can cover nearly the entire continental shelf, however in the summer the Bering Sea is essentially ice free and the ice edge retreats to the Chukchi Sea. The observed interannual variation of ice extent is about 25% of the seasonal range (Niebauer, 1983, 1998; Stabeno et al., 1998). The eastern Bering Sea showed the largest nonseasonal variation in

sea ice extent during 1953-1977 among the marginal seas around the Arctic Ocean (Walsh and Johnson, 1979). On longer time scales, North Pacific climate regime shifts occurred in 1977 and 1989 (Niebauer, 1998; Hare and Mantua, 2000), and the Bering Sea ice experienced several different sea ice regime states in recent decades: 1972-1976 was cold, 1977-1988 was warm, and 1989-2001 was cool (Stabeno et al., 2001). Interestingly, the winter sea ice in the Bering Sea is increasing in the most recent years, while the Arctic sea ice is decreasing rapidly in summer. This means the range of the seasonal cycle of sea ice in the Bering Sea-Chukchi Sea system has recently become larger.

Both thermodynamic and dynamic processes contribute to sea ice mass balance. The thermodynamic ice growth and melt is determined by heat fluxes between the ice and the atmosphere, and between the ice and the ocean. It is also tightly related to ice thickness. Sea ice thickness evolves slowly due to thermodynamics and can be changed rapidly by dynamic ice transport. The dynamic ice motion in the Bering Sea is largely driven by wind stress, and ice strength is also related to ice thickness. The relatively thin sea ice in the Bering Sea can respond to variations in thermodynamic and dynamic forcings easily. Although the sea ice mass budget for the Arctic has been studied (Walsh et al., 1985; Zhang et al., 2000; Bitz et al., 2005; Holland et al., 2010), an understanding of the thermodynamic and dynamic contributions to the ice volume change in the Bering Sea is still limited (Walsh et al., 1985; Bitz et al., 2005; Zhang et al., 2010; Danielson et al., 2011).

The observed winter climatology of sea ice cover in the Bering Sea has been described as a conveyor belt mechanism, where ice is formed in the north, drifts southward under the influence of northerly winds, and is melted by the ocean along the southern ice edge (Muench and Ahlnas, 1976; Pease, 1980). Li et al. (2013) quantified this mechanism using an ice-ocean model hindcast, which also allowed an explanation of the spatial structures of the seasonal variations associated with this mechanism. The large seasonal cycle of ice extent is largely associated with solar radiation absorbed by the ocean (Bitz et al., 2005). Li et al. (2013) show that modeled seasonal thermodynamic ice volume change is dominated by surface heat exchange with the atmosphere in the north and oceanic heat flux into ice along the

southern ice edge, with dynamic ice transport largely associated with wind stress.

The climate forcing of sea ice interannual variability in the Bering Sea has been studied extensively. Zhang et al. (2010) focused on interannual sea ice variations in the Bering Sea, which they found to be dominated by wind-driven changes in ice transport and the ocean thermal front in the southern Bering Sea. On a large scale, the interannual variability of sea ice in the Bering Sea is mainly driven by atmospheric forcing especially in winter (Walsh and Johnson, 1979; Walsh and Sater, 1981; Niebauer, 1980, 1983, 1988; Niebauer and Day, 1989; Niebauer, 1998; Rogers, 1981; Overland and Pease, 1982; Sasaki and Minobe, 2005). The winter atmospheric conditions over the Bering Sea (surface air temperature and winds) and the Bering Sea ice cover are mainly determined by the position of Aleutian Low (Rogers, 1981; Cavalieri and Parkinson, 1987; Niebauer, 1998; Rodionov et al., 2005, 2007). The winter air temperature and sea ice extent are also related to storm tracks associated with the strength of the Aleutian Low (Overland and Pease, 1982; Rodionov et al., 2007). Additionally, the local atmospheric wind variability, associated with large geopotential height anomalies over Alaska and large temperature anomalies over the northern Bering Sea, is also important (Sasaki and Minobe, 2005). On a larger scale, the ice concentration anomalies in the Bering Sea and the Sea of Okhotsk tend to be opposite as a result of atmosphere circulation variations one month earlier (Niebauer, 1983; Cavalieri and Parkinson, 1987; Fang and Wallace, 1994; Deser et al., 2000). Furthermore, the Bering Sea experiences atmospheric teleconnections from ENSO (El Nino/Southern Oscillation) and PNA (the Pacific North-American pattern) (Niebauer, 1980, 1988; Niebauer and Day, 1989; Niebauer, 1998; Overland et al., 1999), the Arctic Oscillation (e.g. Overland et al. (1999)), the NPO (North Pacific Oscillation) / WP (Western Pacific) pattern (Rogers, 1981; Fang and Wallace, 1994; Linkin and Nigam, 2008; Matthewman and Magnusdottir, 2011), the East Asia-North Pacific winter climate (Liu et al., 2007) and the East Asian summer monsoon (Zhao et al., 2004).

Here we address the driving mechanisms of sea ice variability in the Bering Sea and quantify the relative roles of thermodynamics and dynamics for winter months from 1980-1989. We use a high-resolution (0.1 degree) global coupled

POP-CICE model forced with CORE2 interannually varying atmosphere forcing. We focus on partitioning the ice volume change into thermodynamic and dynamic components, and investigating the relationship between anomalies of ice variability and anomalies of atmospheric and oceanic conditions. The results yield a comprehensive depiction of the physical processes of sea ice variability in the Bering Sea as revealed in a high-resolution ice-ocean model. The results reveal the importance of thermodynamics on the large scale in the long term and dynamics locally near the ice margins in the short term. Thermodynamic ice volume change is controlled by surface heat flux with the atmosphere especially in the north, and by oceanic heat flux near the ice edge in the south. Ice motion is generally consistent with wind stress acting as the driving agent, except near certain straits in the north.

Section 3.2 describes the ice-ocean model. Section 3.3 shows the results of the relationship of sea ice interannual variability in the Bering Sea with external forcings from the perspective of thermodynamics and dynamics separately. Section 3.4 is the discussion. Section 3.5 is the conclusion.

3.2 Method

We use output from a fine resolution (1/10-degree) global coupled ocean/sea-ice model configured in the Community Earth System (CESM) framework (McClean et al., 2013). This coupled ocean/sea-ice model consists of the Los Alamos National Laboratory Parallel Ocean Program (POP) and the Los Alamos Sea Ice Model (CICE). This model uses a tripole grid with poles in Canada, Russia and Antarctica. Figure 3.1 shows the ocean model bathymetry of the Bering Sea and the model T grid points subsampled every 10 points.

CICE utilizes an energy-conserving thermodynamic sea ice model by Bitz and Lipscomb (1999) to compute ice/snow growth and melt rates. CICE has one snow layer and four ice layers. CICE uses a subgridscale ice thickness distribution with five ice thickness categories: $0.00m \sim 0.60m$, $0.60m \sim 1.40m$, $1.40m \sim 2.40m$, $2.40m \sim 3.60m$, $> 3.60m$. For each ice thickness category, the model calculates the ice and snow thickness changes and vertical temperature profiles

based on vertical radiative, turbulent and conductive heat fluxes. The model considers the effect of brine pockets on specific heat and thermal conductivity due to internal melting and freezing. The vertical salinity profile is prescribed as a constant. CICE use the elastic-viscous-plastic (EVP) sea ice dynamic model by Hunke and Dukowicz (1997) to compute ice velocity. The ice momentum equation involves 5 stresses: wind stress, ocean stress, internal ice stress, Coriolis stress, and stress due to sea surface slope. CICE uses an incremental remapping advection scheme. The important ice thermodynamic and dynamic equations used by CICE are summarized in the Appendix.

POP is a z-level ocean general circulation model which solves the three-dimensional primitive equations for ocean temperature, salinity and momentum. It has an implicit free surface. It uses partial bottom cells for better representation of flow over the bottom boundary. POP has 42 levels of thickness, from 10 m thick in the uppermost layer to 250 m thick in the deep ocean. The horizontal resolution is around 6 km in the Bering Sea. POP and CICE are coupled via an external flux coupler.

This model run is forced with Coordinated Ocean-ice Reference Experiment version 2 (CORE2) interannually varying atmospheric forcing from 1970-1989 (Large and Yeager, 2009). CORE 2 includes 6-hourly (1948-2006) surface wind velocity, specific humidity and air temperature based on NCEP reanalysis, daily radiation (1984-2006) and monthly precipitation (1979-2006) from satellite observations. Climatological mean annual cycles are used for radiation (1948-1983) and precipitation (1948-1978) before satellite observational periods. Some data sets are adjusted to satellite and in situ observations in the mean. For example, NCEP winds are adjusted to QuikSCAT satellite scatterometer winds (2000-2004): wind speed is increased almost everywhere, but wind direction is not corrected. Fluxes of heat, momentum and fresh-water at the surface are calculated interactively with the model variables of SST, ice/snow surface temperature, and ice surface roughness. CORE2 is on T62 grid with a horizontal resolution of $\sim 100km$ (east-west) and $\sim 200km$ (north-south) in the Bering Sea. This CORE2 forcing dataset was also used by Danielson et al. (2011) to drive Bering Sea hindcasts with the Regional

Ocean Modeling System (Haidvogel et al., 2008).

We explicitly distinguish thermodynamic and dynamic ice volume tendencies, which are saved as monthly averages during the model integration. We investigate the interannual variability of ice and atmosphere/ocean conditions from 1980-1989. We mainly consider the anomalous fields after the climatological seasonal cycle is removed based on computing monthly means.

We use satellite passive microwave observations of sea ice concentration on a 25 km grid for model validation. We used Bootstrap Sea Ice Concentrations from Nimbus-7 SMMR and DMSP SSM/I-SSMIS, which is publicly available at National Snow and Ice Data Center (Comiso, 2000).

3.3 Results

3.3.1 Variability of sea ice and climatic forcing over the entire ice cover of the Bering Sea

Sea ice mass budget

The modeled total ice area in the Bering Sea (the sum of ice concentration multiplied by the grid cell area for grid cells where ice concentration is at least 15%) averaged for each month from 1980-1989, and the ice area anomaly after the monthly climatological seasonal mean is removed are shown in Figure 3.2. They are compared with observed ice area derived from satellite observations of sea ice concentration (fractional ice cover in each grid cell). The model captures the observed ice area variability very well on both seasonal and non-seasonal time scales, with correlation for the latter quantity of 0.95. Though the model underestimates seasonal mean ice area during winter months (Figure 3.2a), the amplitude of the winter anomalies matches the observations reasonably well (Figure 3.2b).

As shown in Figure 3.3a,b, the simulated total ice volume in the Bering Sea for 1980-1989 displays large interannual variability. The lowest ice volume winter maxima occur in 1982 and 1989 ($\sim 3.2 \times 10^{11} m^3$) and the highest winter maxima occur in 1984 and 1988 ($\sim 5.4 \times 10^{11} m^3$); opposite extremes can occur in consec-

utive years, e.g., in 1988 and 1989. The time series of ice volume anomalies (with monthly climatology subtracted) shows that the large anomalies are concentrated in winter and spring when the ice volume is large, and could occur in different months during these seasons. The largest negative anomaly occurs in February 1985, and the largest positive anomaly occurs in March 1984. We note that the timing of ice growth is important. Usually early ice growth leads to a lower winter maximum later, e.g. in the winter of 1989, while late ice growth leads to a larger winter maximum, e.g. in the winters of 1984 and 1985. This produces winter dipole structures in the time series of the ice volume anomalies.

Next we consider ice volume tendency (partial time derivative of ice volume), which is directly related to atmospheric and oceanic forcings. We partition the ice volume change into thermodynamic and dynamic components. Thermodynamic ice volume tendency is the ice volume change due to ice growth (including congelation ice growth, frazil ice growth and snow ice formation) and ice melt at the bottom, surface and lateral sides of sea ice, where positive/negative value means ice volume increase/decrease due to thermodynamic processes. Dynamic ice volume tendency is the ice volume change due to ice motion, where positive/negative value means ice volume increase/decrease resulting from ice transport into/out of a certain area. The net ice volume tendency is the sum of thermodynamic ice volume tendency and dynamic ice volume tendency.

The net, thermodynamic and dynamic ice volume tendencies summed over the ice-covered area for the whole Bering Sea and their anomalies are calculated for each month from 1980-1989. As shown in Figure 3.4a, in general, the net ice volume tendency is dominated by thermodynamic ice volume tendency, and the contribution of ice dynamics is relatively small except for some key anomaly events. For example, in February 1989, dynamic tendency is 3.5 times as large as thermodynamic tendency but with an opposite sign, hence the net total ice volume change is more related to the ice dynamics.

In terms of anomalies (with the monthly climatological mean removed), net ice volume change is more consistent with thermodynamics in general, but dynamics are important in some cases such as in February 1989 (Figure 3.4b). Dynamic

anomalies are generally a little weaker than thermodynamic anomalies in magnitude, but can be stronger such as in February 1989. Dynamic and thermodynamic anomalies usually have opposing signs, but in some large anomaly events such as in February 1984 and February 1989, these two components occur with the same sign, producing extreme net tendency anomalies.

The ice volume tendencies manifest large variations from year to year especially in winter and spring when ice is abundant. In February 1984, thermodynamic, dynamic and net ice volume tendency anomalies all reach their most positive values during 1980-1989. In February 1989, anomalies of net and dynamic ice volume tendencies attain their most negative values, and thermodynamic tendency anomaly is also very negative. Detailed examination of these two large anomaly events is presented later.

It is interesting to note that the ice volume anomaly variability has approximately a 1-month lag relative to the ice volume tendency anomaly (highest correlation -0.61 with 1 month lag), and is smoother in time than the ice volume tendency anomaly. As shown in this section, the ice volume tendency anomaly is dominated by its thermodynamic component. In the next section we will show that thermodynamic tendency responds to its thermal forcing from the atmosphere nearly simultaneously. Thus the ice volume anomaly responds to thermal forcing with a 1-month lag. This is consistent with previously published estimations of ice response times, roughly 2-6 weeks (Fang and Wallace, 1994; Deser et al., 2000).

Sea ice heat budget

As shown in the last section, the net ice volume tendency for the whole Bering Sea is dominated by thermodynamic ice volume tendency. Here we show that winter thermodynamic ice volume tendency is mainly controlled by net surface heat flux (between the ice and the atmosphere) and surface air temperature. Surface air temperature and net surface heat flux are averaged over the ice-covered area in the Bering Sea, and then their anomalies are calculated, as shown in Figures 3.5 and 3.6. Surface air temperature and surface heat flux anomalies have high correlations with thermodynamic ice volume tendency anomaly in winter,

with correlations of -0.74 and -0.68, respectively, at zero lag.

The surface air temperature changes rapidly, and has large variations, as shown in Figure 3.5. The coldest February air temperature ($\sim -25\ ^\circ$ C) occurring in 1984 and the warmest February air temperature ($\sim -5\ ^\circ$ C) occurring in 1989, correspond to the two largest ice volume tendency anomalies (with opposite signs) in Figure 3.4b. This suggests that surface air temperature strongly controls ice volume tendency.

We further partition the net surface heat flux into its four components: shortwave radiation, longwave radiation, latent heat flux and sensible heat flux (Figure 3.6a). The net shortwave radiation is approximated as the difference of absorbed solar radiation (incoming solar radiation minus reflected solar radiation) and solar radiation penetrating into the ocean, which includes solar radiation absorbed both at surface and in the ice interior. It is more exact to consider the difference of absorbed solar radiation and solar radiation penetrating into the ice away from the upper ice surface for the surface heat flux budget, but that term was not archived as part of the model output. The net shortwave radiation (Figure 3.6a) consequently includes an internal component that is large in spring and summer, but is not very important in winter. The net longwave radiation is the sum of the incoming longwave radiation, which is specified in the atmospheric forcing, and the outgoing longwave radiation, which is calculated as blackbody radiation based on the ice/snow surface temperature.

As shown in Figure 3.6a, sensible heat flux visually correlates very closely with net surface heat flux. During the fall and winter seasons, sensible heat flux and net longwave radiation dominate net surface heat flux, while net shortwave radiation and latent heat flux are insignificant. In spring, high values of shortwave radiation nearly balance longwave radiation while turbulent fluxes are small. The solar radiation is very stable from year to year. As shown in Figure 3.6b, the interannual variability of net surface heat flux is dominated by that of sensible heat flux, with a high correlation coefficient of 0.83. Latent heat flux anomalies also correlate well with net surface heat flux anomalies, having a correlation of 0.71, but with very small relative magnitude. Longwave radiation variation generally

opposes net surface heat flux variation as a negative feedback. Sensible heat flux, latent heat flux and outgoing longwave radiation are all computed interactively based on the surface temperature of snow-free ice or snow, so that net surface heat flux should have a clear relationship with surface air temperature. In fact, the net surface heat flux variation has a 0.60 correlation with surface air temperature variation, including all months, which increases to 0.88 for winter months.

The main results of the surface heat flux budget analysis for Bering Sea ice are summarized as follows:

1) Sensible heat flux dominates net surface heat flux.

2) Longwave radiation is secondly important.

3) Shortwave radiation is not important in fall and winter when ice grows and reaches its maximum, but is more important for spring ice retreat.

4) Latent heat flux has the smallest magnitude among the surface heat flux components, but correlates well with net surface heat flux.

5) The net surface heat flux variability can be largely explained by the surface air temperature anomaly especially in winter.

Sea ice force balance

In this section, the force balance of sea ice is analyzed. Sea ice motion is driven by several forces. The momentum equation for sea ice involves five stresses on the ice: wind stress, ocean stress, internal ice stress, Coriolis stress, and stress due to sea surface slope.

$$m\frac{\partial \mathbf{u}}{\partial t} = \overrightarrow{\tau_a} + \overrightarrow{\tau_w} + \nabla \cdot \sigma - \hat{k} \times mf\mathbf{u} - mg\nabla H_0 \tag{3.1}$$

where m is the combined mass of ice and snow per unit area, $\overrightarrow{\tau_a}$ and $\overrightarrow{\tau_w}$ are the wind stress on ice and the ocean stress on ice, $\nabla \cdot \sigma$ is the internal ice stress, $-\hat{k} \times mf\mathbf{u}$ is the stress due to Coriolis effects, and $-mg\nabla H_0$ is the stress due to sea surface slope (sea surface height H_0 is relative to the geoid). Monthly mean wind stress on the ice, ocean stress on the ice, internal ice stress, Coriolis stress are archived in the model output. We construct the stress due to sea surface slope, based on model outputs of sea surface height, ice thickness, and snow thickness.

We construct time series of ice velocity, wind stress, ocean stress, Coriolis stress, internal ice stress, stress due to sea surface slope and net stress averaged over the ice-covered area and time series of their anomalies after seasonal cycles are removed (Figure 3.7). The ice velocity correlates well with wind stress simultaneously, especially in the meridional direction (compare Figure 3.7c and the red curve in Figure 3.7a, also compare Figure 3.7i and the red curve in Figure 3.7g). As shown in Figure 3.7a,b, wind stress is the largest term, and the oppositely directed ocean stress is slightly weaker. The internal ice stress is usually the third largest term, in the opposite direction to the wind stress, and can be as large as the ocean stress in the meridional direction, such as during the February 1989 anomaly event. The internal ice stress plays a more important role in the zonal direction than in the meridional direction. This is due to the geometry of the Bering Sea, in that the Bering Sea is bounded by land in the east-west direction, and in the south it is open ocean. Ice typically moves southwestward (Figure 3.7c,d). Thus ice has more compression near the western land boundary, and moves more freely to the south. It should be noted that this is the spatial average of internal ice stress, which is quite inhomogeneous in space. So the actual values near the key land boundaries are even larger than this mean value, and the values are small over the central and southern ice-covered region. Coriolis stress and the stress due to sea surface slope are insignificant. The net stress of these five stresses is nearly zero, indicating a force equilibrium and nearly steady motion of the sea ice on the monthly mean timescale. This means the dynamic response time scale of sea ice is shorter than one month. This is in contrast to the approximately one-month lagged response of ice volume to external heat fluxes.

Since the largest two stresses (wind and ocean) are nearly counterbalancing each other, it is useful to examine the residual sum of these two terms in relation to the other (smaller) stress terms. In Figure 3.7e,f, we compare this residual sum to the Coriolis stress, internal ice stress, and stress due to sea surface slope averaged over the ice-covered area and their anomalies. The residual sum is usually in the same direction as the wind, indicating wind-driven ice flow, with ocean drag, on the large scale. Internal ice stress also opposes the residual sum, resisting ice motion,

consistent with the wind-driven mechanism. Small stress terms Coriolis stress and stress due to sea surface slope have similar magnitudes.

Our results are consistent with previous work in the Arctic Ocean by Steele et al. (1997). They show that ice acceleration is almost zero for timescales much larger than a day, that the Coriolis stress and stress due to sea surface slope are small, and that the largest stress terms are wind stress, ocean stress and internal ice stress.

Our results imply that Bering sea ice motion is largely driven by wind stress, especially along the ice edge where sea ice is close to a freely drifting state. This is consistent with other studies (Thorndike and Colony, 1982; Reynolds et al., 1985; Kimura and Wakatsuchi, 2000, 2001). Thorndike and Colony (1982) showed that the wind (estimated geostrophically from sea-level pressure) explains a large fraction of the variance of ice velocity in the central Arctic on short time scales, while the long term (several month) averaged ice motion has equal contributions from the geostrophic wind and the mean ocean circulation. Reynolds et al. (1985) show that in the open ocean sea ice moves to the right of surface wind at an angle of 30° at approximate 4% of the wind speed at 3 m. Kimura and Wakatsuchi (2000, 2001) show a high correlation of sea ice motion and wind along the ice edge in the Bering Sea on daily timescales.

Here we can also evaluate the free drift assumption for Bering sea ice motion away from land (Pease and Overland, 1984; Reynolds et al., 1985; Connolley et al., 2004). The steady state of ice velocity is a good approximation, because the net stress is nearly zero everywhere in the Bering Sea as previously shown here. Ignoring the stress due to sea surface slope is reasonable, except in certain northern coastal regions. However, the internal ice stress is only small in the central and southern ice-covered area; it can be very important at some local spots near the land boundaries in the north. Although these previous studies retain the Coriolis stress, we find here that this term is very small, and is only relatively important near the ice edge. Therefore, free drift of sea ice is valid in the central and southern ice-covered area in the Bering Sea, but is not valid in the northern regions near land.

3.3.2 Anomalous events

We next examine the two largest Bering Sea ice anomaly events in the time interval 1980-1989 that occur with opposite anomalous ice and atmosphere/ocean conditions.

February 1989

In February 1989, the ice volume tendency anomaly reached its most negative value over the 1980-1989 period. Figure 3.8 shows the spatial structures of ice variables so that we can determine the regional processes affecting this anomalous state. The net ice volume tendency anomaly is very negative over the extensive ice-covered area in the southern and central regions, and is very positive along the regions to the south of the land boundaries, as shown in Figure 3.8d. This pattern is driven by the combined forcing of anomalous warm air and anomalous southerly wind, as shown in Figure 3.9a.

The southerly wind (Figure 3.9a) drives ice transport northward (Figure 3.8c). This causes a negative dynamic tendency anomaly in the south and middle of the ice-covered area, and a positive dynamic tendency anomaly near the northern coasts and islands (Figure 3.8f). The ice transport anomaly through the Bering Strait is towards the Arctic Ocean (Figure 3.8c), and this causes the total dynamic tendency anomaly in the Bering Sea to be very negative (Figure 3.8f).

The wind stress anomaly on the ice (Figure 3.9b) and the ocean stress anomaly on the ice (Figure 3.9d) have opposing signs with very similar magnitude. As shown in Figure 3.8c and 3.9d, the spatial distribution of the magnitude of the ice velocity anomaly is consistent with structures seen in the magnitude of the wind stress anomaly. The direction of the ice velocity anomaly is rotated to the right of the wind stress anomaly with an angle of approximately 30°. This indicates that the wind stress anomaly drives the ice motion anomaly, and the ocean stress anomaly resists the ice motion anomaly and almost balances the wind stress anomaly.

The thermodynamic tendency anomaly consists of an ice volume decrease in the north and an ice volume increase along the southern ice edge due to thermodynamics, as shown in Figure 3.8e. This can be best understood by partitioning

the thermodynamic tendency anomaly into ice growth anomalies (including congelation ice growth, frazil ice growth and snow ice formation; not shown here) and ice melt anomalies (including basal ice melt, lateral ice melt and top ice melt; not shown here). We find that the northern negative anomaly of thermodynamic tendency is due to congelation ice growth, and the southern positive anomaly is dominated by basal ice melt. This dipole pattern of thermodynamic tendency anomaly corresponds to the air-ice heat flux anomaly (acting in the north, Figure 3.9b) and the ocean-ice heat flux anomaly (acting in the south, Figure 3.9d) very well. The 15% ice concentration contour approximately marks the boundary of these two regions. We can see that the atmospheric thermal forcing acts weakly over the extensive ice-covered region but very strongly around the northern coastal polynyas, and oceanic thermal forcing works in a narrow band around the ice edge.

Warm surface air temperature (Figure 3.9a) can reduce surface heat flux from ice to atmosphere (Figure 3.9b) and thus suppress ice growth (Figure 3.8e). This occurs on the large scale almost everywhere over the ice-covered area in the Bering Sea. Also, dynamical ice thickening due to ice motion against the northern coasts of the Bering Sea (Figure 3.8f) further weakens air-ice heat flux (Figure 3.9b) and ice growth (Figure 3.8e) there to a large degree. On the other hand, the ice retreat away from the warm ocean water in the south (Figure 3.8c), especially away from the warm Bering Slope Current, causes reduced bottom ice melting from the ocean (Figure 3.8e) because less ice is left to melt.

February 1984

In February 1984, the ice volume tendency anomaly is the most positive during the 1980-1989 period. The net ice volume tendency anomaly is very positive almost everywhere in the ice-covered area, as shown in Figure 3.10d. Thermodynamically, ice is growing anomalously in the extensive ice interior in the middle and north, and is melting anomalously along a narrow band around the ice edge (Figure 3.10e). Dynamically, ice is anomalously transported away from the southern side of land and into the southern ice edge region (Figure 3.10c,f). Comparing the net ice volume tendency and thermodynamic/dynamic tendencies (Figure 3.10d,e,f), we can see that in the ice interior thermodynamics is a little stronger than dynam-

ics while around the coastal polynyas thermodynamics is nearly in balance with dynamics, and dynamics dominate along the ice edge.

The anomaly of southward ice motion (Figure 3.10c) is driven by a northerly wind anomaly (Figure 3.11a). The anomalously cold surface air temperature (Figure 3.11a) promotes larger heat loss from ice to atmosphere (Figure 3.11b) and thus larger ice growth rate in the north especially around the coastal polynyas (Figure 3.10e). Ice advection into the southern warm ocean (Figure 3.10c,f) produces larger basal melt rate along the ice edge (Figure 3.10e). The cooling of sea surface temperature around the ice edge (Figure 3.11c) might be the consequence of the ice bottom melting there (Figure 3.10e).

Atmosphere Circulation

The position of the Aleutian Low largely determines ice variations in the Bering Sea (Rogers, 1981; Cavalieri and Parkinson, 1987; Niebauer, 1998; Rodionov et al., 2005, 2007). The winter sea ice extent is also associated with storm tracks (Overland and Pease, 1982; Rodionov et al., 2007), and the local atmospheric variability related to winds (Sasaki and Minobe, 2005).

On the large scale, a very high sea level pressure anomaly ($\sim$20 hPa higher than normal) occurs in Feb 1989, centered near the Gulf of Alaska, as shown in Figure 3.9e. There is also anomalous low pressure over the Arctic especially on the Siberian side in Feb 1989 (Figure 3.9e). These sea level pressure anomalies induce anomalous southerly winds over the Bering Sea in Figure 3.9a. The high pressure anomaly can already be seen clearly over Alaska in Jan 1989, and it moves to the west and becomes much weaker in March 1989. In contrast, anomalous low pressure in the east and anomalous high pressure in the northwest (Figure 3.11e), favoring anomalous northerly winds (Figure 3.11a), occur in Feb 1984 when ice volume tendency is highest (Figure 3.10d).

These two anomalous events are associated with substantially different patterns of the Aleutian Low (Figure 3.9 and Figure 3.11). In Feb 1989, the Aleutian Low was centered at the southwestern corner of the Bering Sea, while in Feb 1984, the Aleutian Low had two split centers, one around the Gulf of Alaska, and the other further southwest of the Aleutian Islands (further south of the case in Feb

1984). The total distribution of sea level pressure produces anomalous southerly wind in Feb 1989 (Figure 3.9a) and anomalous northerly wind in Feb 1984 (Figure 3.11a).

Our results closely resemble the study by Rodionov et al. (2005, 2007). The warm event in Feb 1989 is classified as W1 type of atmospheric circulation, and the cold event in Feb 1984 as C1 type in Table 1 of their paper. Type W1 is defined as Aleutian Low with one single center located north of 51° N and between 156 ° W and 173 ° W. Type C1 is a split Aleutian Low with western center south of 52 ° N and eastern center not further east than 140 ° W. These types correspond to warm and cold surface air temperatures for winter months in the Bering Sea very well. W1 type is related to transient storms, where most storms enter the Bering Sea along the secondary storm track off the Siberian coast, and fewer enter along the primary storm track in the central and eastern North Pacific. C1 type is accompanied by eastward extension of a stronger Siberian High. C1 has storms penetrating not so far north as W1 along the Siberian coast, and has northerly flow on the east periphery of the upper atmospheric ridge. Additionally, they show that the climate indices for the North Pacific (NP, PDO and PNA) poorly represent the winter air temperatures in the Bering Sea. Instead, the warm event in Feb 1989 is associated with an enhanced storm track off the Siberian coast. This implies local forcing of the anomalous event from the intrinsic variability due to storm tracks, rather than from large-scale climate variations.

3.3.3 Local forcing of ice variation

Integrating the characteristics of ice over the entire basin can often mask the local importance of various terms in the balances. Some terms may have spatial averages that are small even though they exhibit large-scale structures, which are regionally important. To better understand the relationship between ice variables and environmental conditions, we focus on two key locations in the Bering Sea (Figure 3.1), one in the northern "growth region" (a $90km \times 60km$ box centered at 63.76 ° N, 173.01 ° W) and one in the southern "melt" region (a $127km \times 100km$ box centered at 60.89 ° N, 178.31 ° W). These two points are examples of the large

growth rate near the northern coastal polynyas and the large melt rate near the southern ice edge, under the additional influence of strong advective affects.

Local mass budget

When considering the local climate forcing of ice variability, it is useful to separate thermodynamic and dynamic ice volume tendencies, which exhibit large interannual variability while the net ice volume tendency remains relatively stable. The separation of thermodynamics and dynamics can distinguish ice response to thermal and mechanical forcings.

At the northern site (Figure 3.12), the thermodynamic process is dominated by ice growth (Figure 3.12b), and ice is transported out of this region in winter (see the blue curve in Figure 3.12a). During fall and spring, when the ice edge passes through this site, ice melting becomes important (Figure 3.12b), but the winter season is the focus of this section. When the external disturbance is large enough, the ice response is very obvious. In the warm winters of 1982 and 1989, both the thermodynamic ice growth and the dynamic ice transport out of the region are weakened (Figure 3.12a). In contrast, in the cold winters of 1983 and 1984, ice growth and ice advection are strengthened (Figure 3.12a). These anomaly events can be explained by the atmospheric forcing. As shown in Figure 3.13a,b, in the winters of 1982 and 1989, the surface air temperature is warmer than normal (Figure 3.13b), the surface heat fluxes are weaker (Figure 3.13a), and consequently the ice growth is suppressed (Figure 3.12b). Additionally, prominent anomalous southerly winds (Figure 3.13c,d) reduce the ice transport out of this region (Figure 3.12a). In contrast, in the winters of 1983 and 1984, colder air temperature (Figure 3.13b), stronger surface heat flux (Figure 3.13a) and stronger northerly winds (Figure 3.13c,d) produce more ice growth and more ice transport (Figure 3.12a).

Next we quantify how ice variables and processes are related to environmental conditions at this location. Surface heat flux and surface air temperature (Figure 3.13a,b) correlate very well with thermodynamic ice volume change (Figure 3.12a,c). The correlation between surface heat flux anomaly and thermodynamic tendency anomaly is high for all months, -0.92, and even higher for winter months

(-0.98). The correlation between surface air temperature anomaly and thermodynamic tendency anomaly is lower than this, -0.68 for all months, and -0.73 for winter. This suggests that air temperature is not the only thing controlling the ice growth in this region, although its effect is clearly strong.

The ice transport out of this northern region (Figure 3.12a,c) is suppressed by southerly wind anomalies (Figure 3.13c,d), and promoted by northerly wind anomalies. Wind stress largely drives ice motion. This is evident in the high correlation, 0.89, between the meridional ice velocity and meridional wind stress (not shown here).

At this northern site, the anomalies of thermodynamic and dynamic ice volume tendencies are opposite in sign with similar magnitudes and a correlation coefficient of -0.67, as shown in Figure 3.12c. These two effects nearly balance each other, leaving a small sum. The small residual tends to be dominated by the dynamic term, with a correlation of 0.78. This is indicative of there being a stable ice cover in winter here every year, with small changes being disturbed by the broad-scale wind forcing and brought back to normal conditions by the thermodynamic effects. However, the exception to this generalization is the large anomaly event of the 1989 winter when the net ice volume tendency is dominated by thermodynamics. In that event, warm air (Figure 3.13b) contributes to lower ice growth, while southerly winds (Figure 3.13c) restore the normal ice conditions by advective affects.

The southwestern site (Figure 3.14) is near the ice edge in winter, and is dominated by dynamic ice transport into this region and ice bottom melt in winter (very weak ice growth occurs in winter) (Figure 3.14a,b). During the winters of 1982 and 1989 when southerly winds blow (Figure 3.15c), both weakened ice transport inflow from the north and less local basal melting occur (Figure 3.14a) because southerly winds push ice to move northward and less ice is left for melting at this local site. During the winters when stronger northerly winds blow such as in 1980, 1983 and 1987 (Figure 3.15c), both ice transport into this site and basal melting increase (Figure 3.14a).

At this southwestern site close to the ice edge, ice dynamical effects in

winter are significant (Figure 3.14a) due to large winds around this area and the free drifting ice there. Ice motion is largely driven by wind stress, based on the very high correlation (> 0.9) between ice velocity and wind stress (not shown here). There is also high correlation between zonal ice velocity and zonal ocean velocity especially in winter (0.72). This is because open water between ice floes is dominated by east-west Ekman transport forced by the north-south wind fluctuations. These currents, acting in the 10 m thick surface grid box, thereby advect the sparsely covered ice field that is embedded in this flow at each grid point.

At this southwestern ice edge in winter, the ice response to atmospheric thermal forcing (Figure 3.15a,b) is evident but not so obvious as in the north. The correlation of the surface air temperature anomaly with thermodynamic ice volume tendency anomaly is 0.51 (0.60 in winter), not as high as in the northern site. Because near the southwestern ice edge the thermodynamic effect is dominated by ice bottom melting from warm ocean water, the thermodynamic ice volume tendency would be expected to be associated with oceanic forcing (Figure 3.16a). Indeed, the oceanic heat flux anomaly (Figure 3.16a) and thermodynamic tendency anomaly (red curve in Figure 3.14c) have a high correlation, 0.99, indicating that oceanic heat flux controls ice melting around the ice edge. Note also that positive ocean zonal velocity anomalies occur before the positive sea surface temperature anomalies in the 1982 and 1989 low ice years (not shown here), indicating anomalous oceanic heat advection from the warm Bering Slope Current to the ice edge and/or from the deep basin onto the shelf.

The anti-correlation between dynamics and thermodynamics, and the dominance of dynamics in the net ice volume change are prominent along this southwestern ice edge. As shown in Figure 3.14c, the anomalies of thermodynamic and dynamic tendencies have a high correlation, -0.87, for year-round behavior, and extremely high correlation, -0.98, for winter months. The net ice volume tendency anomaly correlates well with dynamic tendency anomaly, with a correlation of 0.66 (0.83 for winter).

The net ice volume tendency near the ice edge (Figure 3.14) has larger interannual variability than the net ice volume tendency in the north (Figure 3.12),

implying the ice edge is less stable and may be more sensitive to climate forcing than the ice interior. Because the ice along the ice edge is thin, sea ice there can respond to climate forcing easily. Because the ice response time along the ice edge is so short (less than one month), the ice velocity anomaly has a high simultaneous correlation (0.95) with wind stress anomaly; the winter ice volume anomaly also has simultaneous correlation of -0.89 with surface heat flux anomaly. This explains the lack of a lag here that was found in the northern box, where the response time is slower for thicker ice.

In summary, for these characteristic local sites near ice margins with either land or ocean, surface heat flux and surface air temperature correlate well with thermodynamic ice volume change especially in the north, while oceanic heat flux controls ice melt around the ice edge in the south. Wind stress largely drives ice motion especially in the meridional direction. The anti-correlation between dynamic and thermodynamic ice volume changes is strong in both locations, but strongest in the south. Dynamic processes dominate the net ice volume change anomalies at both of these local sites near two very different ice margins. But the net changes are very small in the north, where there is lots of ice by the land boundary, and are quite large in the south, where there is little ice by the ocean boundary.

Local ice heat budget

The local budget of surface heat flux shows its dependence on location. At the northern growth site (Figure 3.17), net surface heat flux (Figure 3.17a) and its anomaly (Figure 3.17b) are dominated by sensible heat flux from December to April when ice is abundant, indicating the important role of air temperature on surface heat flux. Both the shortwave and the longwave radiation are relatively stable from year to year, but shortwave radiation is only significant in spring and summer while longwave radiation is important in winter and spring. The net surface heat flux is negative during winter months, and then is nearly zero in late spring and summer. Both net surface heat flux and sensible heat flux are small in the 1982 and 1989 warm winters, and large in the 1983 and 1984 cold winters.

These anomalies of surface heat flux could explain the weak ice growth in 1982 and 1989 and strong ice growth in 1983 and 1984 (Figure 3.12), and are consistent with warm air temperature in 1982 and 1989 and cold air temperature in 1983 and 1984 (Figure 3.13).

In contrast, at the southern melt site (Figure 3.18), winter net surface heat flux is small and negative, and is mainly determined by the balance of negative longwave radiation, negative latent heat flux and positive sensible heat flux in winter. The sensible heat flux is always positive along the ice edge where air temperature is warmer than ice surface temperature. The interannual variability of net surface heat flux still correlates well with the sensible heat flux anomaly. Because sensible heat flux, latent heat flux and longwave radiation are all dependent on ice surface temperature, significant correlations also exist between them.

In summary, on monthly to interannual time scales, sensible heat flux controls net surface heat flux. The surface heat flux with the atmosphere is more important in the northern growth region than near the southern ice edge. In the north, net surface heat flux is dominated by sensible heat flux during winter months; along the ice edge, winter net surface heat flux is the combined effect of longwave radiation, latent heat flux and sensible heat flux.

Local ice force balance

We also consider the force balances at these two different local sites and their relations to ice motion there. The stresses on the sea ice consist of wind stress on the ice, ocean stress on the ice, Coriolis stress, internal ice stress, and stress due to sea surface slope.

For the northern site, as shown in Figure 3.19a,b, these five stresses are nearly in balance, producing nearly zero net stress. The dominant stresses are wind stress and ocean stress with opposite directions and similar magnitudes (Figure 3.19a,b). In the meridional direction, wind stress is slightly stronger than the ocean stress (Figure 3.19a). The meridional ice velocity (Figure 3.19c) is consistent with the meridional wind stress (red curve in Figure 3.19a). However, in the zonal direction, the ocean stress is slightly stronger than the wind stress (Figure 3.19b),

and the zonal ice velocity (Figure 3.19d) is more consistent with the zonal ocean stress (blue curve in Figure 3.19b). This indicates that at some northern spots near narrow straits such as this site, the zonal ice velocity is more related to ocean stress, while the meridional ice velocity is consistent with wind stress. The internal ice stress is significant in this high ice concentration area (Figure 3.19a,b), and generally resists ice motion there (Figure 3.19c,d). It is noted that the meridional stress due to sea surface slope is significant at this northern site (magenta curve in Figure 3.19a), where the relatively large sea surface slope drives northward ocean flow and resists southward ice motion.

At this northern site, the sum of wind stress and ocean stress is on the same order with some other small stress terms, as shown in Figure 3.19e,f. In the meridional direction (Figure 3.19e), northward internal ice stress and stress due to sea surface slope are opposed by the southward residual of wind stress and ocean stress, and Coriolis stress. Note that the northward stress due to sea surface slope is as strong as the meridional internal ice stress. The meridional Coriolis stress is also large due to fast zonal ice motion through the strait. In the zonal direction (Figure 3.19f), it is mainly the balance between internal ice stress and the residual sum of wind stress and ocean stress.

For the southern site, the stress quasi-equilibrium also holds (Figure 3.20a,b). The ice velocity (Figure 3.20c,d) is very consistent with the wind stress (red curves in Figure 3.20a,b), which is almost balanced by the opposite ocean stress (blue curves in Figure 3.20a,b). The internal ice stress is weak and southward in winter (Figure 3.20a,b). There is nearly no stress due to sea surface slope (Figure 3.20a,b), implying a relatively flat sea surface corresponding to the geoid near the open ocean. In the meridional direction (Figure 3.20a,e), wind stress is nearly balanced by ocean stress. The northward Coriolis stress balances southward internal ice stress. In the zonal direction (Figure 3.20f), the residual sum of wind stress and ocean stress largely balances Coriolis stress.

In summary, wind stress on the ice, ocean stress on the ice, Coriolis stress, internal ice stress, and stress due to sea surface slope are almost in balance, producing nearly steady ice motion. The ice motion is largely driven by the wind stress

especially in the meridional direction, almost balanced by the opposite ocean stress. At some northern spots near narrow straits, the ice motion follows the direction of the ocean stress. The internal ice stress can be important at some local spots near the land boundaries in the north (largely balanced by the sum of wind stress and ocean stress), resisting the ice motion, and is small in the central and southern ice-covered area. Coriolis stress and the stress due to sea surface slope are small, but Coriolis stress is relatively important along the ice edge in the south, and the meridional stress due to sea surface slope can be significant in the north near land.

3.3.4 Sea ice transport through the Bering Strait

The ice transport through the Bering Strait provides a form of freshwater and energy flux between the Bering Sea and the Arctic Ocean, and influences the amount of freshwater and heat of the upper layer of the western Arctic Ocean.

The model saved the monthly mean ice mass transport on the northern side and on the eastern side for each grid cell. The ice volume transport through the Bering Strait is calculated (monthly 1980-1989), as shown in Figure 3.21a. Based on the climatology (Figure 3.21b), the ice transport through the Bering Strait is mainly northward (reaching a maximum in April) with the exception of November when ice is transported southward. In other words, the Bering Sea is providing sea ice to the Arctic Ocean in winter and spring even though the wind is blowing southward. This could be explained by the very large northward ocean velocity near the Bering Strait. But at the beginning of the ice season, ice is advected from the Arctic Ocean to the Bering Sea and contributes partially to the initial ice seen in the Bering Sea. On the other hand, the ice transport through the Bering Strait shows large interannual variability, as shown in Figure 3.21a. Notably, in Feb 1989, the northward ice transport is extremely high when strong southerly winds dominate the region. In contrast, in Feb 1984, the southward ice transport is the largest during this time period, when the northerly wind is very strong. This indicates that ocean currents drive the climatological mean ice transport through the Bering Strait, while the winds cause the anomalies of ice transport.

As expected, the ice volume transport through the Bering Strait (Figure

3.21a) agrees well with the dynamic ice volume tendency integrated over the whole Bering Sea (blue curve in Figure 3.4a). The dynamic ice volume tendency in the Bering Sea is determined by the ice transport at the boundaries of the Bering Sea. The Bering Strait is the most important boundary. At other boundaries with the open ocean, there is almost no ice transport. Note that there is a tiny amount of ice transport along the coast of the Kamchatka Peninsula, but that amount is insignificant relative to the ice transport through the Bering Strait. Therefore, the ice transport through Bering Strait essentially indicates the integrated Bering Sea ice volume change due to dynamics.

The modeled ice volume transport through the Bering Strait is consistent with the range of field measurements by Woodgate and Aagaard (2005) and Travers (2012). They provide estimates of the Bering Strait ice flux to be $\sim 130 \pm 90 km^3 yr^{-1}$ for the winter of 1990-1991 and $\sim 190 \pm 50 km^3 yr^{-1}$ for the winter of 2007-2008. POP-CICE model estimates the climatological winter mean (Jan-May 1980-1989) ice transport through the Bering Strait to be $146 km^3 yr^{-1}$, very consistent with these observations. However, the observations in 1990-1991 show high month-to-month variability, with almost no ice transport in Dec 1990, southward ice transport at the beginning of 1991 peaking in February, a switch from northward to southward in March, and northward ice transport since April, reaching a maximum in late May. In contrast, the modeled 10-year climatology shows weak southward ice transport in Nov, and consistent northward ice transport from Dec to June, reaching a maximum in April. But the month-to-month variability of the model can exhibit a similar range of values as the observations. For example, in the winter of 1984, the model produces a similar strong southward transport in February and strong northward transport in May as in the observed winter of 1991. The large interannual variability of ice transport through the Bering Strait therefore needs to be carefully considered when computing a climatology.

3.4 Discussion

In the Bering Sea, ice volume tendency is dominated by thermodynamic processes on the large scale, while dynamic effects are important locally, especially near the ice margins with ocean and land. Local thermodynamic and dynamic ice volume tendencies usually have opposite signs with similar magnitudes, producing stable ice volume. However, the anomalies of thermodynamic and dynamic tendencies can have the same sign to produce extreme anomalous events. Near the ice margins, the net ice volume change is usually dominated by dynamics. The dynamic effect is largely weakened by thermodynamics in the long term; dynamics rapidly initiate ice variations, and thermodynamics slowly bring the situation back to normal. So thermodynamics tends to be more important on long timescales, and dynamics tends to be more important on short timescales. The anti-correlation between thermodynamic and dynamic tendencies, and the dominance of dynamics, occurs more prominently near the southern ice edge where ice varies a lot, and less so near the northern coastal polynyas where ice is stable. In the ice interior, the dynamic effect is very small, and the thermodynamic effect determines the net ice volume change.

Thermodynamic ice volume tendency correlates well with surface heat flux and surface air temperature in winter on the large scale. Locally in the central and northern parts of the Bering Sea, air-ice heat flux controls ice growth, while ocean-ice heat flux controls basal ice melting around the southern ice edge. Surface heat flux between the ice and the atmosphere is dominated by sensible heat flux, and net longwave radiation is also large.

Monthly mean ice motion is nearly in phase with wind stress, especially in the meridional direction. Ocean stress can be important in driving ice motion near narrow straits in the north. Wind stress and ocean stress have similar and large magnitudes with opposing signs. Internal ice stress is large near the land boundaries in the north, and is small in the central and southern ice-covered area. The Coriolis stress and the stress due to sea surface slope are generally small.

The local and regional atmospheric and oceanic forcing of Bering Sea ice was also examined to determine the details of the local balances controlling ice.

Our results are generally consistent with other studies. Some studies show that the climatic forcing of the Bering Sea ice variability arises from local processes (Fang and Wallace, 1994; Sasaki and Minobe, 2005), rather than being associated with any prominent large-scale remote climate indices. Wind anomalies over the Bering Sea are important for the interannual variability of sea ice. Many studies indicate the correspondence of anomalous northerly wind and more sea ice in the Bering Sea (Niebauer, 1980; Walsh and Sater, 1981; Fang and Wallace, 1994; Sasaki and Minobe, 2005). At the same time, surface air temperature anomalies are related to advection by winds on the large scale (e.g. Deser et al. (2000)).

It is interesting to consider sea ice response time to external forcings. Our results show that ice volume anomalies generally respond to thermal forcing, e.g., surface heat flux, with a 1-month lag (see section 3.1.1 and 3.1.2). However, ice motion responds on a faster timescale (days to weeks) to mechanical forcing, e.g., wind stress, producing ice velocities that are nearly in phase with monthly mean winds. Although Sasaki and Minobe (2005) show that local wind anomalies lead sea ice concentration anomalies by 1 month, this may be due to the thermodynamic effect driven by the winds. Similarly, Fang and Wallace (1994) show that the Western Pacific pattern in 500 hPa heights leads sea ice in the Bering Sea by 1 month, which also could be explained by the concomitant thermodynamic forcing. Lastly, Walsh and Sater (1981) show that atmosphere forcing averaged over the 3-4 months prior to maximum ice extent correlates well with sea ice variation, which is consistent with the results found here if the antecedent month dominates that 3-4 month average and if thermodynamics control the response.

In terms of spatial distributions, the thermodynamic processes affect the large-scale ice volume change quite uniformly over the ice-covered area, and thus the integrated effect is large. In contrast, dynamic effects produce small-scale features, and are more important near the ice margins with ocean and land than in the ice interior. Therefore, both in time and in space, thermodynamics contribute to low frequency ice variations, and dynamics contribute to higher frequency variations of sea ice in the Bering Sea.

The interactions between sea ice thickness and thermodynamic and dy-

namic processes are also considered. Both thermodynamic and dynamic processes cause ice thickness to change, and ultimately determine the ice thickness. On the other hand, ice thickness influences the thermodynamic and dynamic ice volume tendencies in different ways. Thin ice grows faster thermodynamically, and thick ice contributes to larger dynamic ice transport. Thus, dynamic ice transport is important for thick ice, such as the sea ice in the central Arctic Ocean. Thermodynamics is important for thin ice, such as the sea ice in the marginal ice zones. As a marginal ice zone, the Bering Sea has thin seasonal sea ice. So thermodynamics dominate the sea ice variability in the Bering Sea.

Our results are consistent with Walsh et al. (1985)'s result that thermodynamic processes contribute more to ice anomalies near the ice edge. Their Figure 15 shows that the thermodynamic processes dominate the seasonal cycle of ice mass change in the Bering Sea, small dynamic effect opposes thermodynamic effect on the annual mean basis, and ice is transported from the eastern to the western Bering Sea. Their Figure 17 shows that even on the interannual time scale, thermodynamic processes correlate well with the ice mass change both in the western and in the eastern Bering Sea. This is in contrast to the Arctic, where dynamics dominate in winter, spring and fall, and thermodynamics dominate in summer.

3.5 Conclusion

Using a high-resolution ice-ocean model, the basin-scale and local balances of sea ice in the Bering Sea have been examined. The model produces variations in total ice area anomalies that are highly correlated with observations. The variations in the model ice volume are largely controlled by thermodynamic forcing by surface heat flux, which in turn is dominated by sensible heat flux. This indicates that surface air temperature, which is specified from observations in the CORE2 forcing, strongly controls ice volume tendency. This also explains the similarly high levels of skill for ice area hindcasts that were obtained by Danielson et al. (2011).

Thermodynamic processes dominate the variations in ice volume change in

the Bering Sea on the large scale. In contrast, dynamic processes are important on the local scale near ice margins (both oceanic and land), where local dynamic and thermodynamic ice volume changes have opposite signs with large and similar amplitudes. The thermodynamic ice volume change is dominated by surface heat flux between the ice and the atmosphere, except near the southern ice edge where it is largely controlled by ocean-ice heat flux. Ice motion is generally consistent with winds driving the flow, but ice motion largely follows ocean currents near certain straits in the north. For example, the modeled climatological ice volume transport out of the Bering Strait in winter (Jan-May), $146 km^3 yr^{-1}$, and its high month-to-month variability, are consistent with the range of field measurements by Woodgate and Aagaard (2005) and Travers (2012).

Two key climate events, strong ice growth with cold air temperature and northerly wind in Feb 1984 and weak ice growth with warm air temperature and southerly wind in Feb 1989, are studied in detail. The processes controlling the ice changes are generally similar to those in other years. These events reveal spatial patterns of ice growth anomalies in the north accompanied by ice melt anomalies along the ice edge in the south, and dynamic anomalies transporting ice from the north to the south. These climate events are associated with the position of the Aleutian Low, which appears to be regulated by local processes rather than broad-scale climate events (Rodionov et al., 2005, 2007).

This study of interannual ice variations in the Bering Sea for 1980-1989 can form a baseline for a longer-term ice variability study, including changes in the 1990's and 2000's, as well as including the impacts of global warming. We also plan to study the mesoscale eddy effects through comparison of high-resolution and low-resolution versions of the model, with higher-frequency temporal sampling of the simulations.

Acknowledgments

Funding was provided by NSF (OCE-0960770) and DOE (DE-FG0205ER641 19). The ocean/sea-ice simulation was conducted using computer resources pro-

vided by the Climate Simulation Laboratory at NCAR's Computational and Information Systems Laboratory, sponsored by the National Science Foundation and other agencies.

Chapter 3 is in preparation for submission to Dynamics of Atmospheres and Oceans. Linghan Li, Arthur J Miller, Julie L McClean, Ian Eisenman, and Myrl C Hendershott, 2013. The dissertation author was the primary investigator and author of Chapter 3.

References

Bitz, Cecilia M and Lipscomb, William H. An energy-conserving thermodynamic model of sea ice. *Journal of Geophysical Research: Oceans (1978–2012)*, 104 (C7):15669–15677, 1999.

Bitz, CM; Holland, MM; Hunke, EC, and Moritz, RE. Maintenance of the sea-ice edge. *Journal of climate*, 18(15):2903–2921, 2005.

Cavalieri, DJ and Parkinson, CL. On the relationship between atmospheric circulation and the fluctuations in the sea ice extents of the bering and okhotsk seas. *Journal of Geophysical Research: Oceans (1978–2012)*, 92(C7):7141–7162, 1987.

Comiso, JC. Bootstrap Sea Ice Concentrations from Nimbus-7 SMMR and DMSP SSM/I-SSMIS. Version 2. Boulder, Colorado USA: NASA DAAC at the National Snow and Ice Data Center, 2000, updated 2012.

Connolley, WM; Gregory, JM; Hunke, E, and McLaren, AJ. On the consistent scaling of terms in the sea-ice dynamics equation. *Journal of physical oceanography*, 34(7):1776–1780, 2004.

Danielson, Seth; Curchitser, Enrique; Hedstrom, Kate; Weingartner, Thomas, and Stabeno, Phyllis. On ocean and sea ice modes of variability in the bering sea. *Journal of Geophysical Research: Oceans (1978–2012)*, 116(C12), 2011.

Deser, Clara; Walsh, John E, and Timlin, Michael S. Arctic sea ice variability in the context of recent atmospheric circulation trends. *Journal of Climate*, 13(3): 617–633, 2000.

Fang, Zhifang and Wallace, John M. Arctic sea ice variability on a timescale of weeks and its relation to atmospheric forcing. *Journal of Climate*, 7(12):1897–1914, 1994.

Haidvogel, Dale B; Arango, H; Budgell, WP; Cornuelle, BD; Curchitser, E; Di Lorenzo, E; Fennel, K; Geyer, WR; Hermann, AJ; Lanerolle, L, and others, . Ocean forecasting in terrain-following coordinates: Formulation and skill assessment of the regional ocean modeling system. *Journal of Computational Physics*, 227(7):3595–3624, 2008.

Hare, Steven R and Mantua, Nathan J. Empirical evidence for north pacific regime shifts in 1977 and 1989. *Progress in oceanography*, 47(2):103–145, 2000.

Holland, Marika M; Serreze, Mark C, and Stroeve, Julienne. The sea ice mass budget of the arctic and its future change as simulated by coupled climate models. *Climate Dynamics*, 34(2-3):185–200, 2010.

Hunke, EC and Dukowicz, JK. An elastic-viscous-plastic model for sea ice dynamics. *Journal of Physical Oceanography*, 27(9):1849–1867, 1997.

Kimura, Noriaki and Wakatsuchi, Masaaki. Relationship between sea-ice motion and geostrophic wind in the northern hemisphere. *Geophysical research letters*, 27(22):3735–3738, 2000.

Kimura, Noriaki and Wakatsuchi, Masaaki. Mechanisms for the variation of sea ice extent in the northern hemisphere. *Journal of Geophysical Research: Oceans (1978–2012)*, 106(C12):31319–31331, 2001.

Large, WG and Yeager, SG. The global climatology of an interannually varying air–sea flux data set. *Climate Dynamics*, 33(2-3):341–364, 2009.

Li, Linghan; McClean, Julie L; Miller, Art J; Eisenman, Ian, and Hendershott, Myrl C. Thermodynamic and dynamic controls on the seasonal cycle of sea ice in the Bering Sea. *Ocean Dynamics*, in preparation, 2013.

Linkin, Megan E and Nigam, Sumant. The north pacific oscillation-west pacific teleconnection pattern: Mature-phase structure and winter impacts. *Journal of Climate*, 21(9):1979–1997, 2008.

Liu, Zhengyu; Liu, Yun; Wu, Lixin, and Jacob, R. Seasonal and long-term atmospheric responses to reemerging north pacific ocean variability: A combined dynamical and statistical assessment*. *Journal of Climate*, 20(6):955–980, 2007.

Matthewman, N Joss and Magnusdottir, Gudrun. Observed interaction between pacific sea ice and the western pacific pattern on intraseasonal time scales. *Journal of Climate*, 24(19):5031–5042, 2011.

McClean, Julie L, Papadopoulos, Caroline, Yulaeva, Elena, and Bailey, David. High resolution CESM: A 40-year CORE forced global coupled 0.1-deg ocean/sea-ice simulation. CESM Workshop 2013, Breckenridge CO, June 2013.

Muench, RD and Ahlnas, K. Ice movement and distribution in the bering sea from march to june 1974. *Journal of Geophysical Research*, 81(24):4467–4476, 1976.

Niebauer, HJ. Sea ice and temperature variability in the eastern bering sea and the relation to atmospheric fluctuations. *Journal of Geophysical Research: Oceans (1978–2012)*, 85(C12):7507–7515, 1980.

Niebauer, HJ. Multiyear sea ice variability in the eastern bering sea: An update. *Journal of Geophysical Research*, 88(C5):2733–2742, 1983.

Niebauer, HJ. Effects of el nino-southern oscillation and north pacific weather patterns on interannual variability in the subarctic bering sea. *Journal of Geophysical Research: Oceans (1978–2012)*, 93(C5):5051–5068, 1988.

Niebauer, HJ. Variability in bering sea ice cover as affected by a regime shift in the north pacific in the period 1947–1996. *Journal of Geophysical Research: Oceans (1978–2012)*, 103(C12):27717–27737, 1998.

Niebauer, HJ and Day, Robert H. Causes of interannual variability in the sea ice cover of the eastern bering sea. *GeoJournal*, 18(1):45–59, 1989.

Overland, James E and Pease, Carol H. Cyclone climatology of the bering sea and its relation to sea ice extent. *Monthly Weather Review*, 110(1):5–13, 1982.

Overland, James E; Adams, Jennifer Miletta, and Bond, Nicholas A. Decadal variability of the aleutian low and its relation to high-latitude circulation*. *Journal of Climate*, 12(5):1542–1548, 1999.

Pease, Carol H. Eastern bering sea ice processes. *Monthly Weather Review*, 108 (12):2015–2023, 1980.

Pease, CH and Overland, JE. An atmospherically driven sea-ice drift model for the bering sea. *Ann. Glaciol*, 5:111–114, 1984.

Reynolds, Michael; Pease, CH, and Overland, JE. Ice drift and regional meteorology in the southern bering sea: Results from mizex west. *Journal of Geophysical Research: Oceans (1978–2012)*, 90(C6):11967–11981, 1985.

Rodionov, SN; Overland, JE, and Bond, NA. The aleutian low and winter climatic conditions in the bering sea. part i: Classification*. *Journal of Climate*, 18(1): 160–177, 2005.

Rodionov, SN; Bond, NA, and Overland, JE. The aleutian low, storm tracks, and winter climate variability in the bering sea. *Deep Sea Research Part II: Topical Studies in Oceanography*, 54(23):2560–2577, 2007.

Rogers, Jeffery C. The north pacific oscillation. *Journal of Climatology*, 1(1): 39–57, 1981.

Sasaki, Yoshi N and Minobe, Shoshiro. Seasonally dependent interannual variability of sea ice in the bering sea and its relation to atmospheric fluctuations. *Journal of geophysical research*, 110(C5):C05011, 2005.

Stabeno, PJ; Schumacher, JD; Davis, RF, and Napp, JM. Under-ice observations of water column temperature, salinity and spring phytoplankton dynamics: Eastern bering sea shelf. *Journal of Marine Research*, 56(1):239–255, 1998.

Stabeno, PJ; Bond, NA; Kachel, NB; Salo, SA, and Schumacher, JD. On the temporal variability of the physical environment over the south-eastern bering sea. *Fisheries Oceanography*, 10(1):81–98, 2001.

Steele, Michael; Zhang, Jinlun; Rothrock, Drew, and Stern, Harry. The force balance of sea ice in a numerical model of the arctic ocean. *Journal of Geophysical Research: Oceans (1978–2012)*, 102(C9):21061–21079, 1997.

Thorndike, AS and Colony, R. Sea ice motion in response to geostrophic winds. *Journal of Geophysical Research: Oceans (1978–2012)*, 87(C8):5845–5852, 1982.

Travers, Cynthia Suzanne. *Quantifying Sea-Ice Volume Flux using Moored Instrumentation in the Bering Strait*. 85 pp., University of Washington, Seattle, 2012.

Walsh, John E and Johnson, Claudia M. An analysis of arctic sea ice fluctuations, 1953-77. *Journal of Physical Oceanography*, 9(3):580–591, 1979.

Walsh, John E and Sater, John E. Monthly and seasonal variability in the ocean-ice-atmosphere systems of the north pacific and the north atlantic. *Journal of Geophysical Research: Oceans (1978–2012)*, 86(C8):7425–7445, 1981.

Walsh, John E; Hibler, William D, and Ross, Becky. Numerical simulation of northern hemisphere sea ice variability, 1951–1980. *Journal of Geophysical Research: Oceans (1978–2012)*, 90(C3):4847–4865, 1985.

Woodgate, Rebecca A and Aagaard, Knut. Revising the bering strait freshwater flux into the arctic ocean. *Geophysical Research Letters*, 32(2), 2005.

Zhang, Jinlun; Rothrock, Drew, and Steele, Michael. Recent changes in arctic sea ice: The interplay between ice dynamics and thermodynamics. *Journal of Climate*, 13(17):3099–3114, 2000.

Zhang, Jinlun; Woodgate, Rebecca, and Moritz, Richard. Sea ice response to atmospheric and oceanic forcing in the bering sea. *Journal of Physical Oceanography*, 40(8):1729–1747, 2010.

Zhao, Ping; Zhang, Xiangdong; Zhou, Xiuji; Ikeda, Moto, and Yin, Yonghong. The sea ice extent anomaly in the north pacific and its impact on the east asian summer monsoon rainfall. *Journal of climate*, 17(17):3434–3447, 2004.

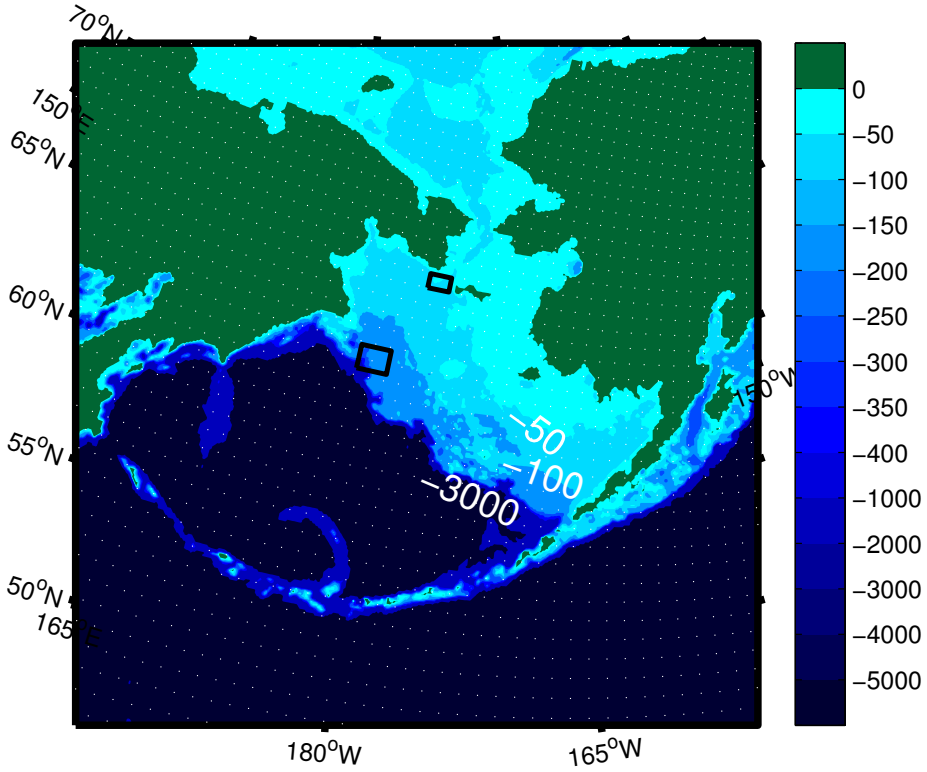

Figure 3.1: Bathymetry of the Bering Sea and the model grid points subsampled every 10 points. Two black boxes indicate the two key sites for studying local forcing of ice variations in Figure 3.12-3.20

.

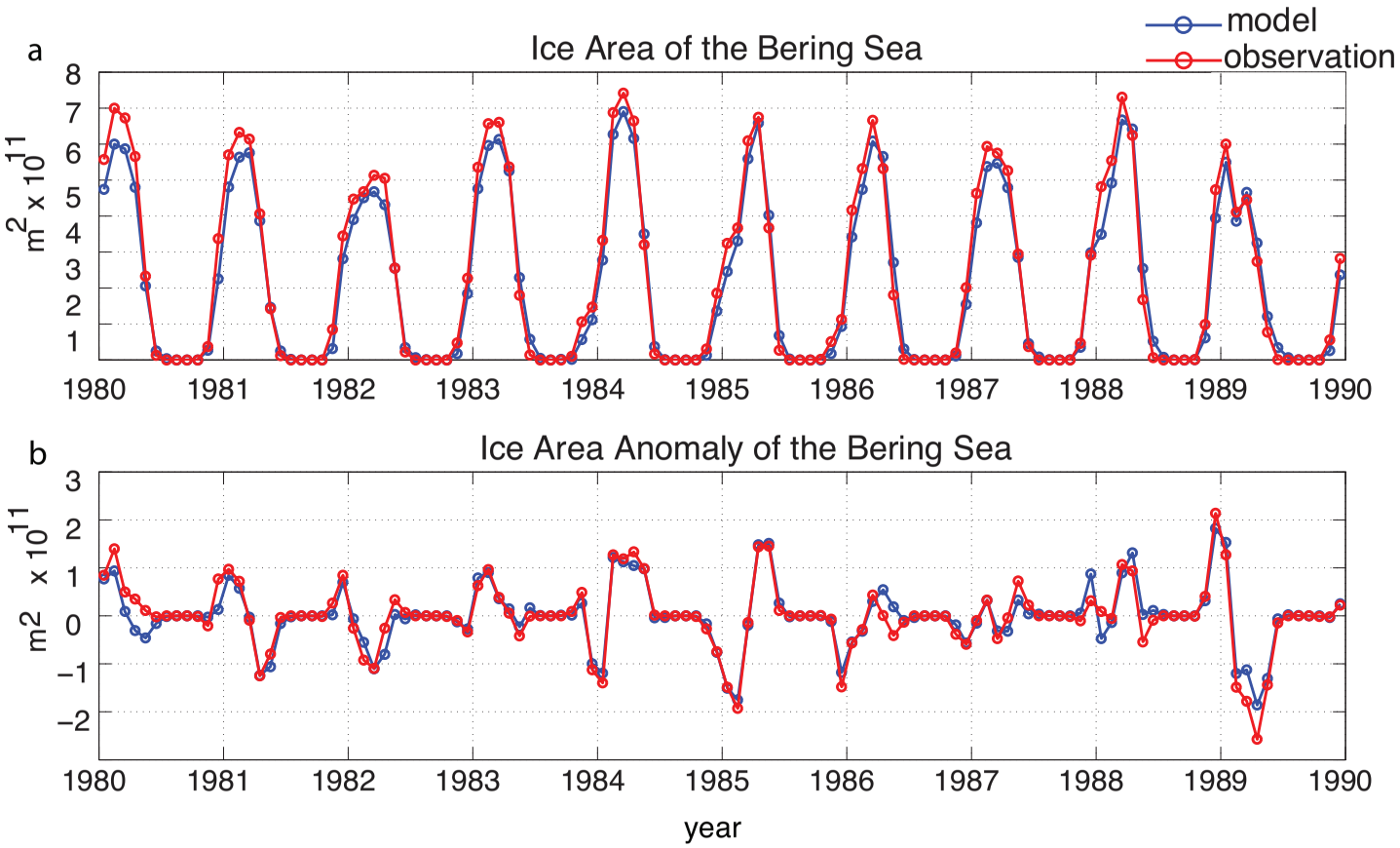

Figure 3.2: (a) Total ice areas of the Bering Sea from model (blue) and from satellite passive microwave observations (red). (b) Anomalies of ice area from model (blue) and from observations (red) after climatological seasonal cycles are removed.

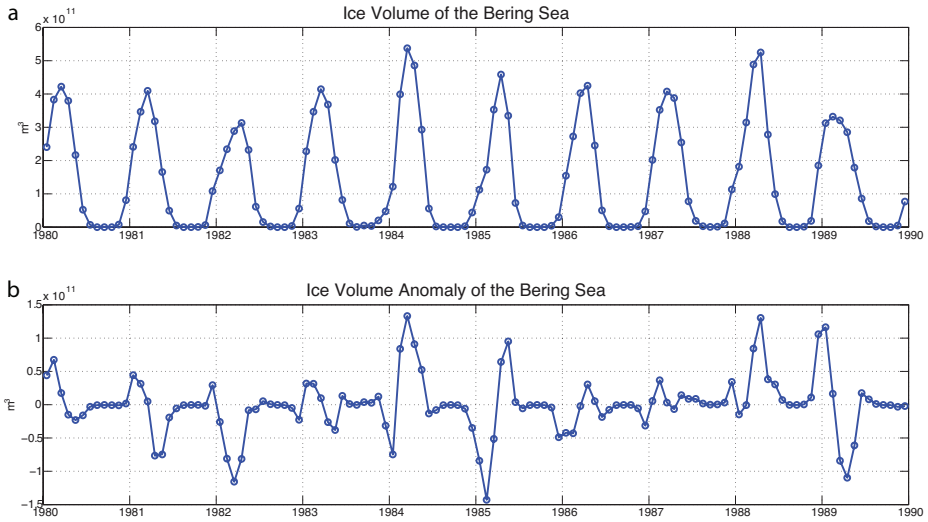

Figure 3.3: (a) Modeled total ice volume of the Bering Sea. (b) Anomaly of total ice volume of the Bering Sea.

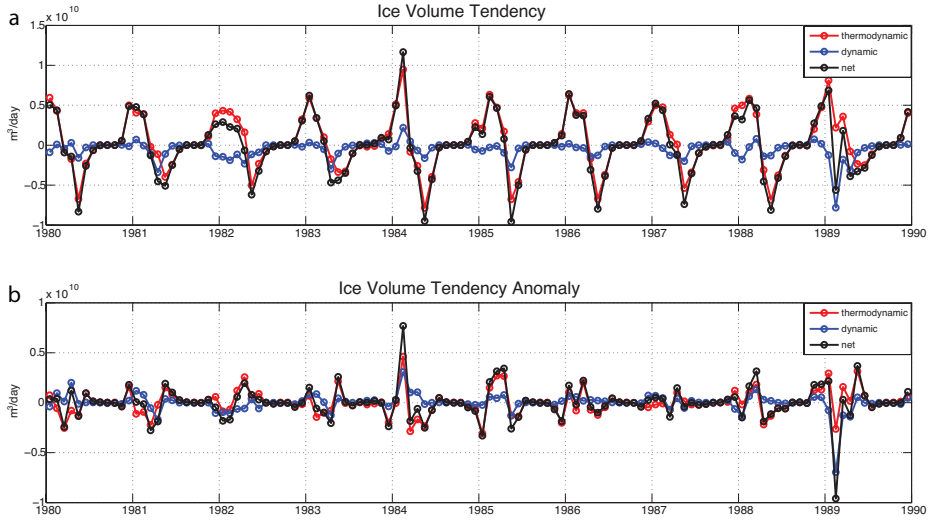

Figure 3.4: (a) Thermodynamic (red), dynamic (blue), and net (black) ice volume tendencies integrated over the entire Bering Sea. (b) Anomalies of thermodynamic (red), dynamic (blue), and net (black) ice volume tendencies integrated over the entire Bering Sea.

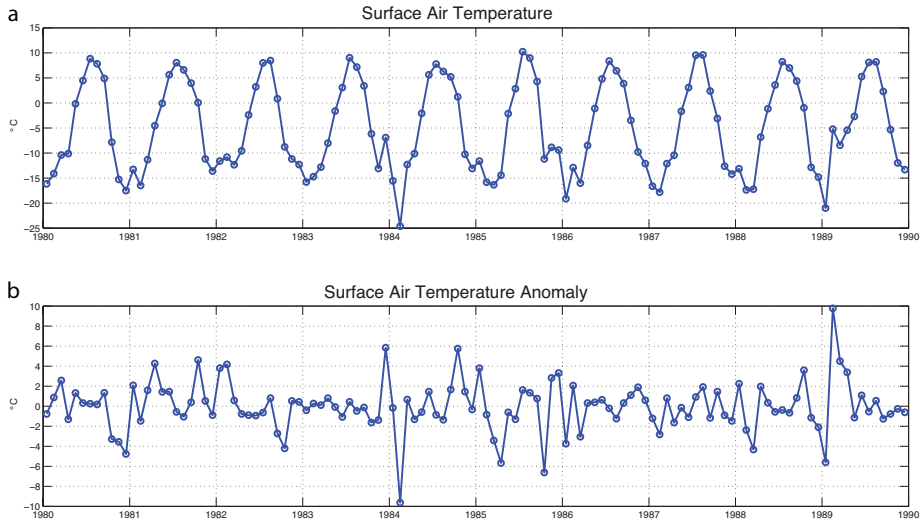

Figure 3.5: (a) Surface air temperature averaged over the ice-covered area of the Bering Sea. (b) Anomaly of surface air temperature averaged over the ice-covered area of the Bering Sea.

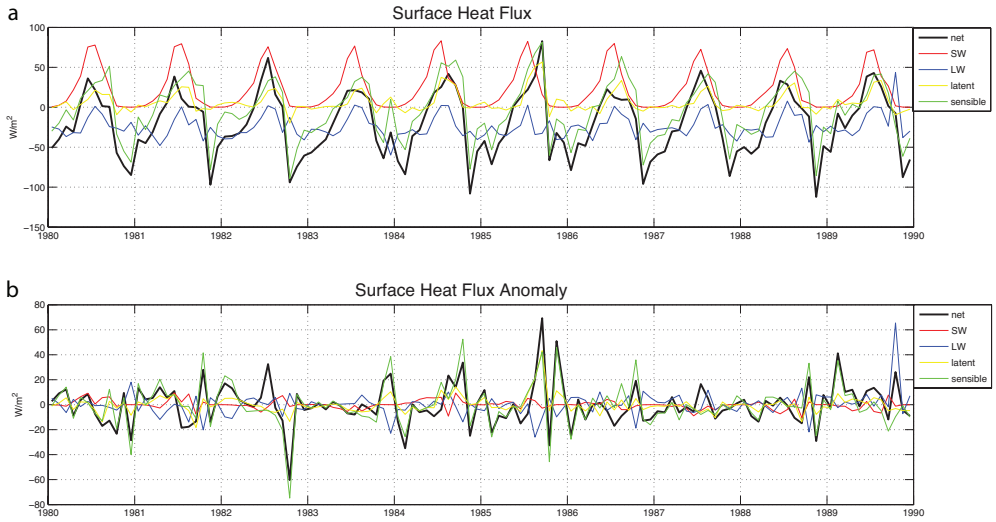

Figure 3.6: (a) Net surface heat flux (black), net shortwave radiation (red), net longwave radiation (blue), latent heat flux (yellow), and sensible heat flux (green) averaged over the ice-covered area of the Bering Sea. (b) Anomalies of net surface heat flux (black), net shortwave radiation (red), net longwave radiation (blue), latent heat flux (yellow), and sensible heat flux (green) averaged over the ice-covered area of the Bering Sea.

Figure 3.7: (a) Meridional components of wind stress on ice (red), ocean stress on ice (blue), Coriolis stress (green), internal ice stress (black), stress due to sea surface slope (magenta), and net stress (cyan) averaged over the ice-covered area of the Bering Sea. (b) Zonal components of wind stress on ice (red), ocean stress on ice (blue), Coriolis stress (green), internal ice stress (black), stress due to sea surface slope (magenta), and net stress (cyan) averaged over the ice-covered area of the Bering Sea. (c) Meridional ice velocity averaged over the ice-covered area of the Bering Sea. (d) Zonal ice velocity averaged over the ice-covered area of the Bering Sea. (e) Meridional components of the sum of wind stress and ocean stress (red), Coriolis stress (green), internal ice stress (black), stress due to sea surface slope (magenta), and net stress (cyan) averaged over the ice-covered area of the Bering Sea. (f) Zonal components of the sum of wind stress and ocean stress (red), Coriolis stress (green), internal ice stress (black), stress due to sea surface slope (magenta), and net stress (cyan) averaged over the ice-covered area of the Bering Sea. (g) Anomalies of meridional components of wind stress on ice (red), ocean stress on ice (blue), Coriolis stress (green), internal ice stress (black), stress due to sea surface slope (magenta), and net stress (cyan) averaged over the ice-covered area of the Bering Sea. (h) Anomalies of zonal components of wind stress on ice (red), ocean stress on ice (blue), Coriolis stress (green), internal ice stress (black), stress due to sea surface slope (magenta), and net stress (cyan) averaged over the ice-covered area of the Bering Sea. (i) Anomalies of meridional ice velocity averaged over the ice-covered area of the Bering Sea. (j) Anomalies of zonal ice velocity averaged over the ice-covered area of the Bering Sea. (k) Anomalies of meridional components of the sum of wind stress and ocean stress (red), Coriolis stress (green), internal ice stress (black), stress due to sea surface slope (magenta), and net stress (cyan) averaged over the ice-covered area of the Bering Sea. (l) Anomalies of zonal components of the sum of wind stress and ocean stress (red), Coriolis stress (green), internal ice stress (black), stress due to sea surface slope (magenta), and net stress (cyan) averaged over the ice-covered area of the Bering Sea.

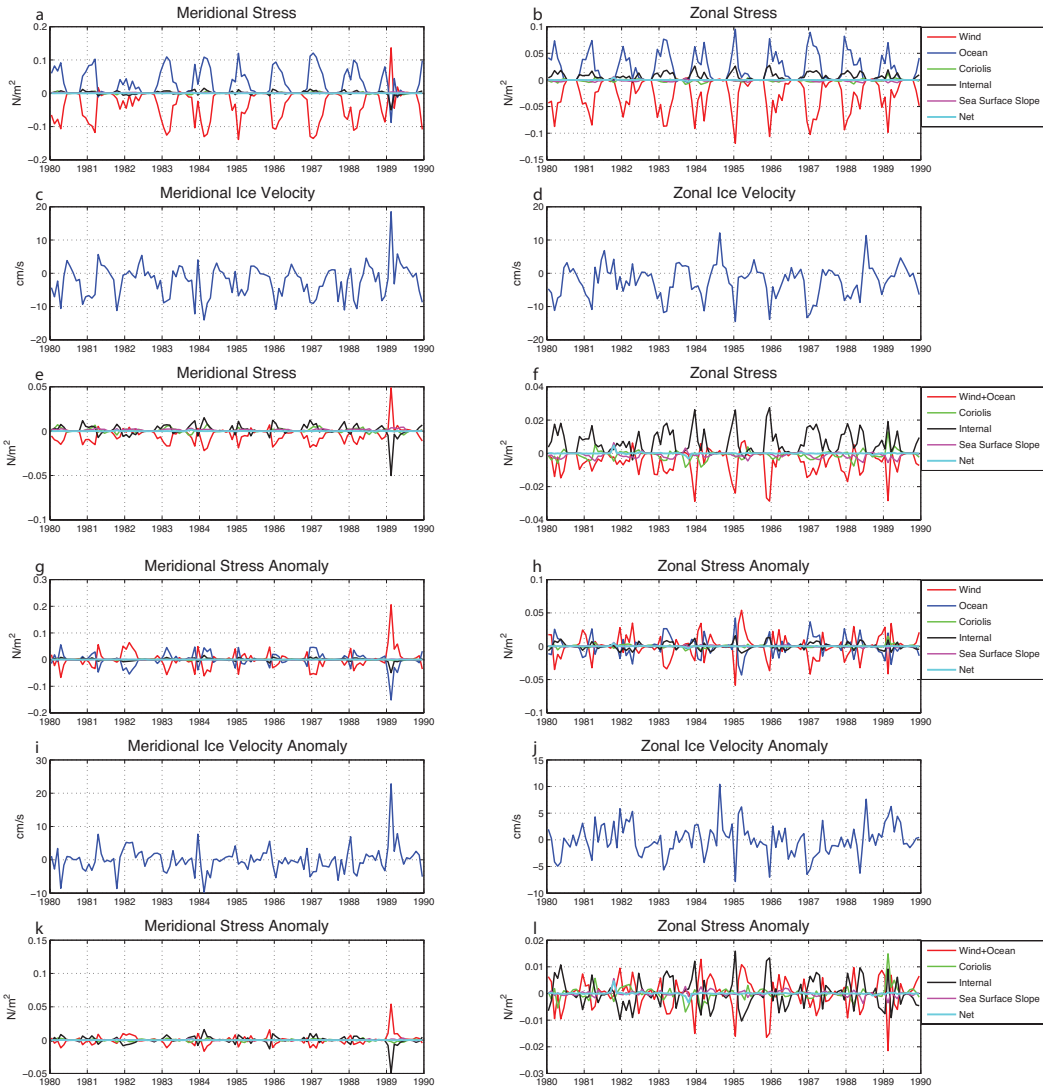
a
Meridional Stress
N/m2
b
Zonal Stress
N/m2
Wind
Ocean
Coriolis
Internal
Sea Surface Slope
Net
c
Meridional Ice Velocity
cm/s
d
Zonal Ice Velocity
cm/s
e
Meridional Stress
N/m2
f
Zonal Stress
N/m2
Wind+Ocean
Coriolis
Internal
Sea Surface Slope
Net
g
Meridional Stress Anomaly
N/m2
h
Zonal Stress Anomaly
N/m2
Wind
Ocean
Coriolis
Internal
Sea Surface Slope
Net
i
Meridional Ice Velocity Anomaly
cm/s
j
Zonal Ice Velocity Anomaly
cm/s
k
Meridional Stress Anomaly
N/m2
l
Zonal Stress Anomaly
N/m2
Wind+Ocean
Coriolis
Internal
Sea Surface Slope
Net
1980 1981 1982 1983 1984 1985 1986 1987 1988 1989 1990

Figure 3.7

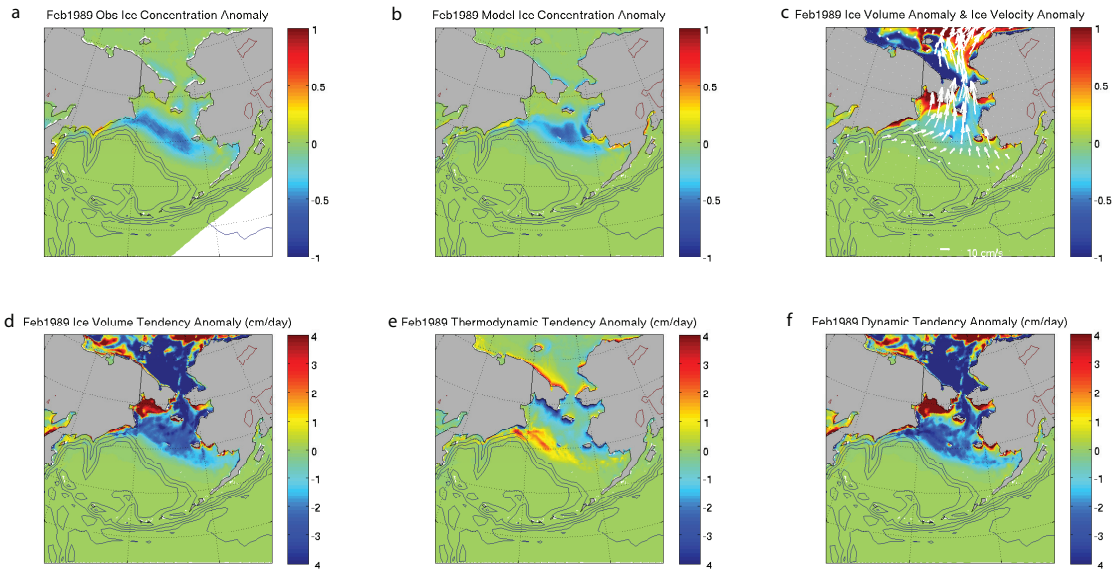

Figure 3.8: (a) February 1989 observed ice concentration anomaly, (b) modeled ice concentration anomaly, (c) ice volume anomaly and ice velocity anomaly, (d) net ice volume tendency anomaly, (e) thermodynamic ice volume tendency anomaly, and (f) dynamic ice volume tendency anomaly.

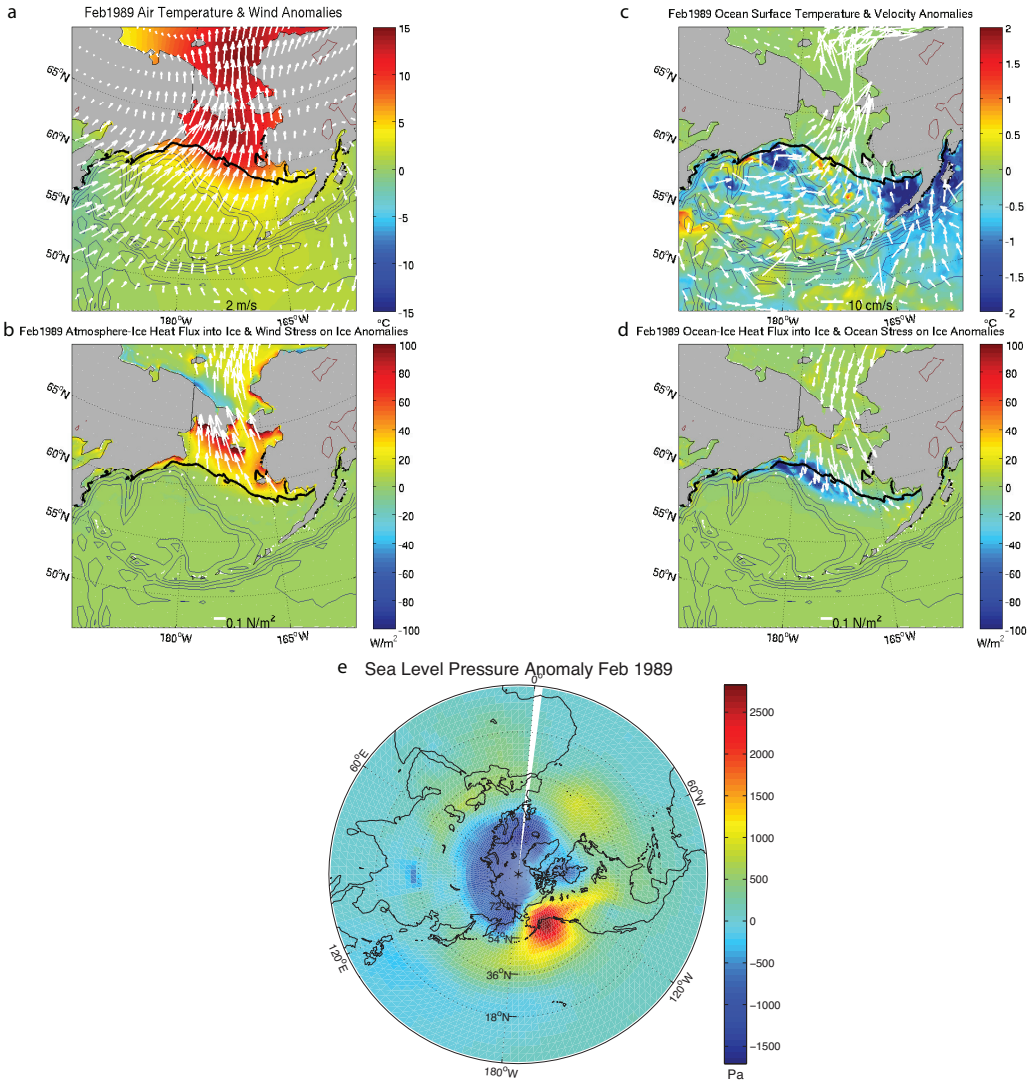

Figure 3.9: (a) February 1989 surface air temperature and wind anomalies, (b) air-ice heat flux and wind stress anomalies, (c) ocean surface temperature and velocity anomalies, (d) ocean-ice heat flux and ocean stress anomalies in the Bering Sea, and (e) sea level pressure anomaly in the northern hemisphere.

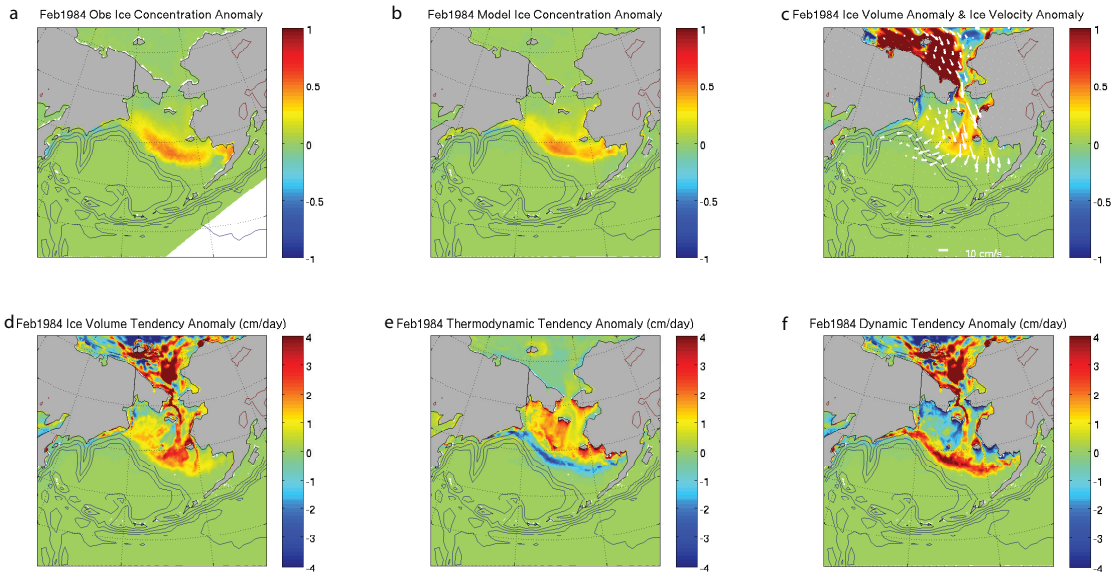

Figure 3.10: (a) February 1984 observed ice concentration anomaly, (b) modeled ice concentration anomaly, (c) ice volume anomaly and ice velocity anomaly, (d) net ice volume tendency anomaly, (e) thermodynamic ice volume tendency anomaly, and (f) dynamic ice volume tendency anomaly.

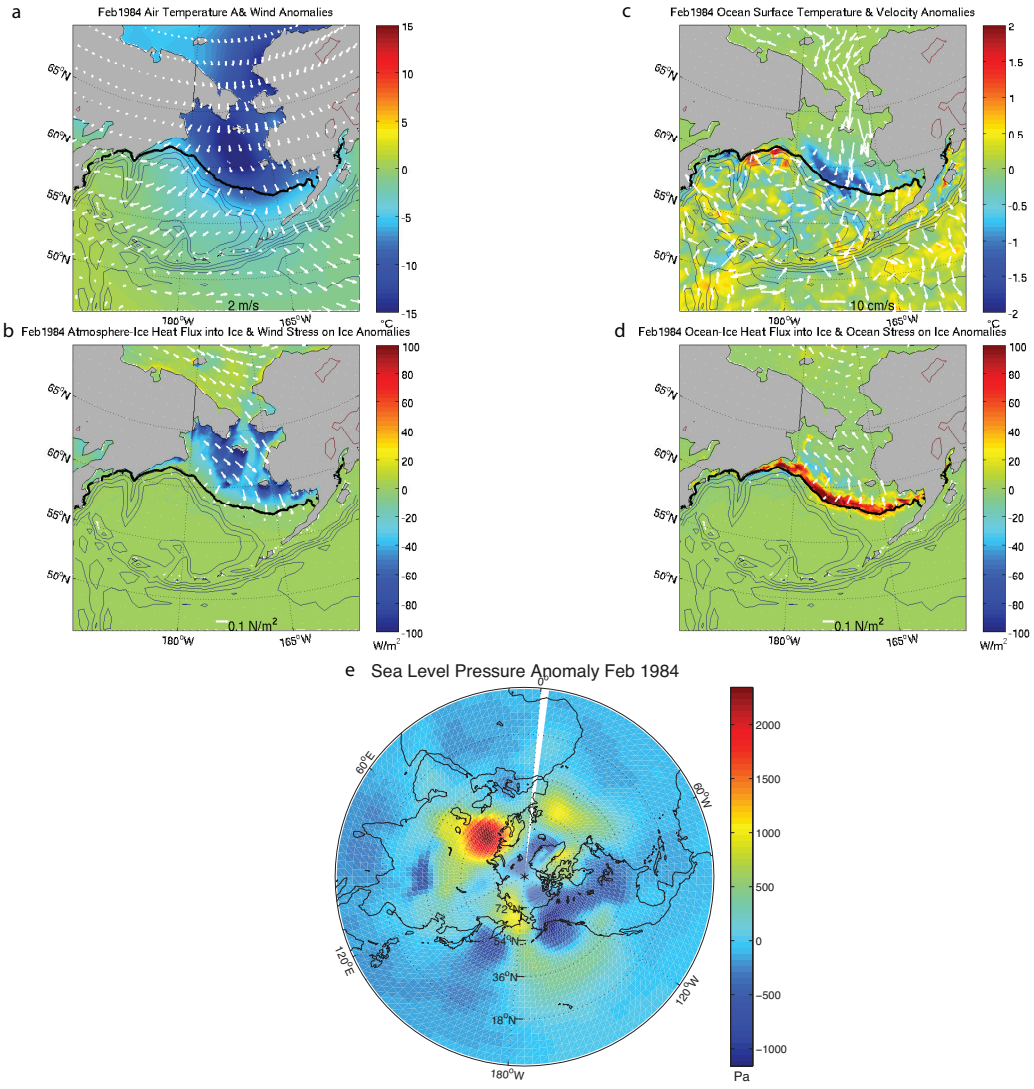

Figure 3.11: (a) February 1984 surface air temperature and wind anomalies, (b) air-ice heat flux and wind stress anomalies, (c) ocean surface temperature and velocity anomalies, (d) ocean-ice heat flux and ocean stress anomalies in the Bering Sea, and (e) sea level pressure anomaly in the northern hemisphere.

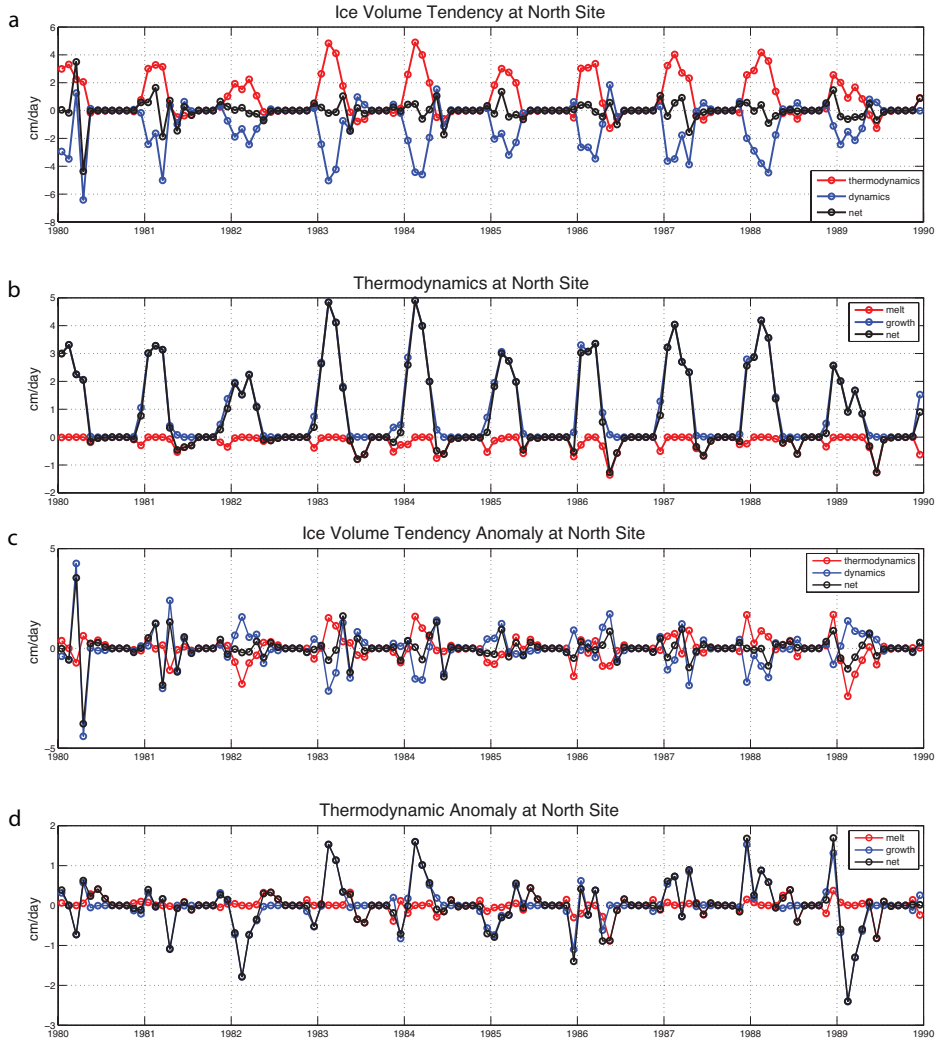

Figure 3.12: (a) Thermodynamic (red), dynamic (blue), and net (black) ice volume tendencies averaged over the northern box in Figure 3.1. (b) Ice melt rate (red), ice growth rate (blue), and net thermodynamic tendency (black) at north site. (c) Anomalies of thermodynamic (red), dynamic (blue), and net (black) ice volume tendencies at north site. (d) Anomalies of ice melt rate (red), ice growth rate (blue), and net thermodynamic tendency (black) at north site.

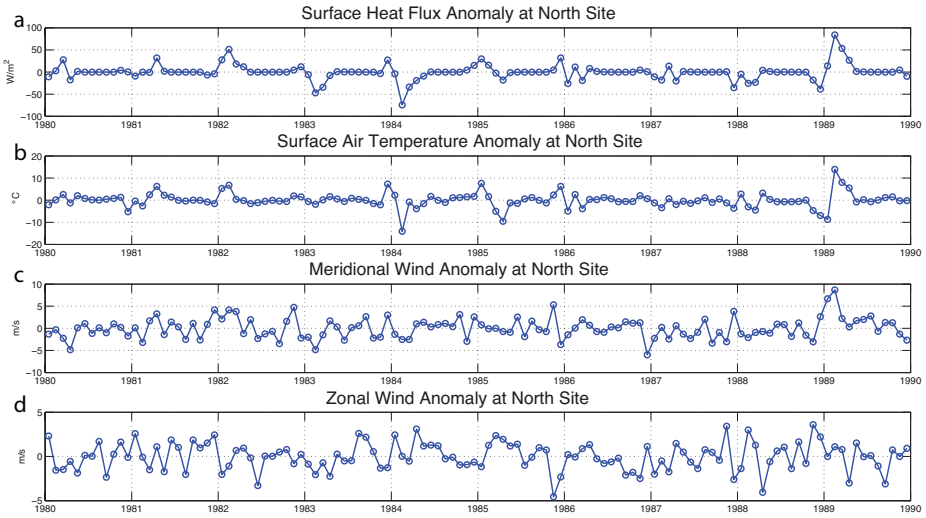

Figure 3.13: (a) Surface heat flux anomaly, (b) surface air temperature anomaly, (c) meridional wind anomaly, (d) zonal wind anomaly averaged over the northern box in Figure 3.1.

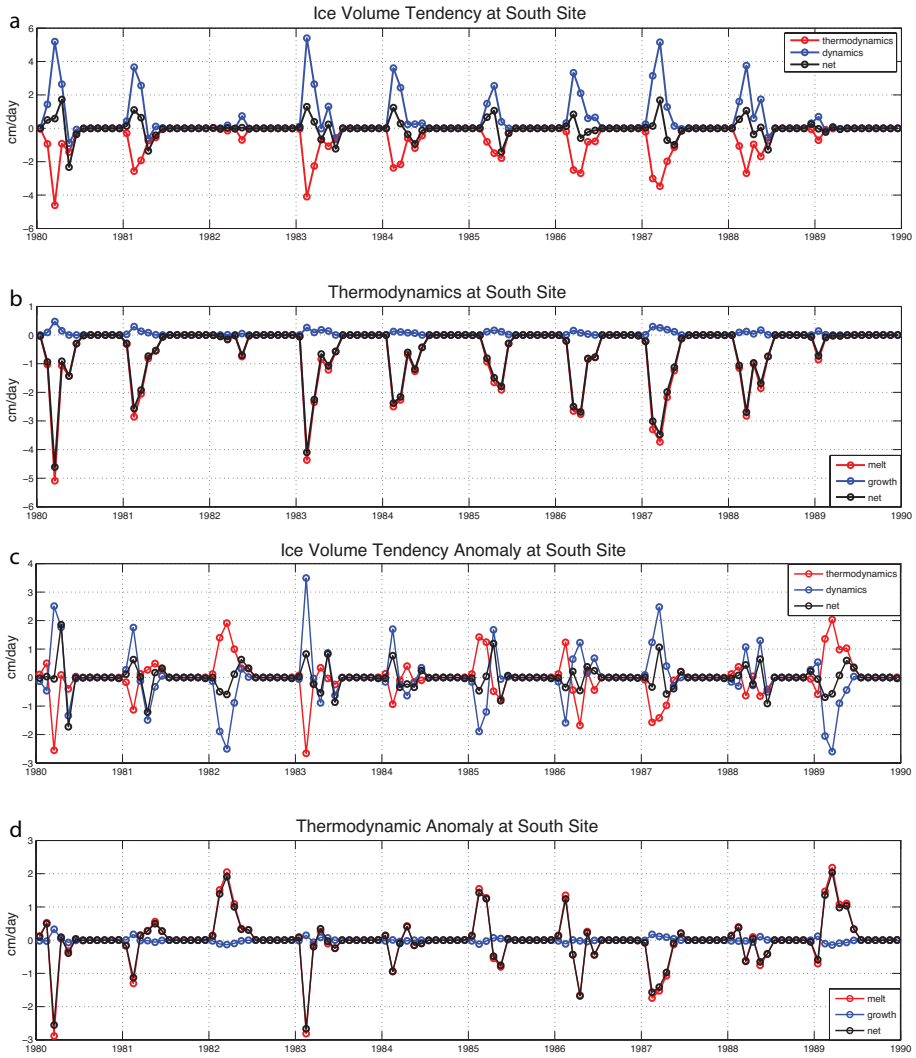

Figure 3.14: (a) Thermodynamic (red), dynamic (blue), and net (black) ice volume tendencies averaged over the southern box in Figure 3.1. (b) Ice melt rate (red), ice growth rate (blue), and net thermodynamic tendency (black) at south site. (c) Anomalies of thermodynamic (red), dynamic (blue), and net (black) ice volume tendencies at south site. (d) Anomalies of ice melt rate (red), ice growth rate (blue), and net thermodynamic tendency (black) at south site.

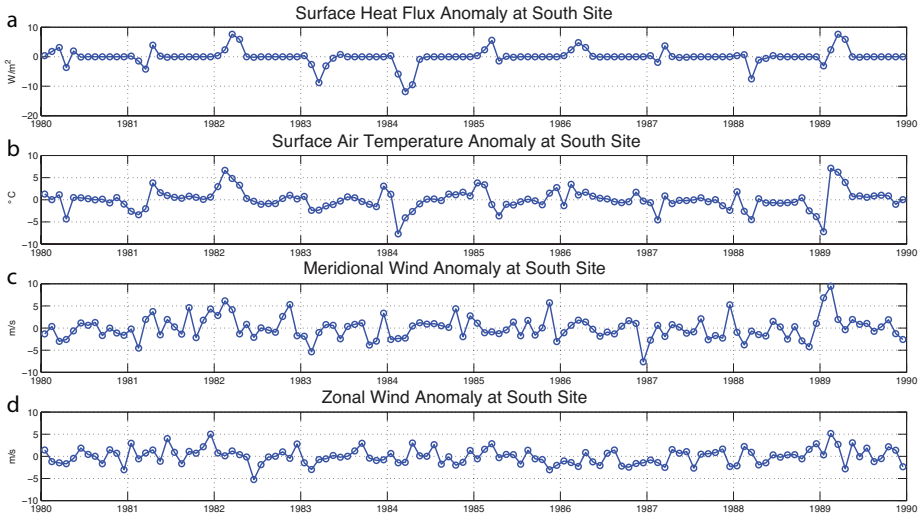

Figure 3.15: (a) Surface heat flux anomaly, (b) surface air temperature anomaly, (c) meridional wind anomaly, (d) zonal wind anomaly averaged over the southern box in Figure 3.1.

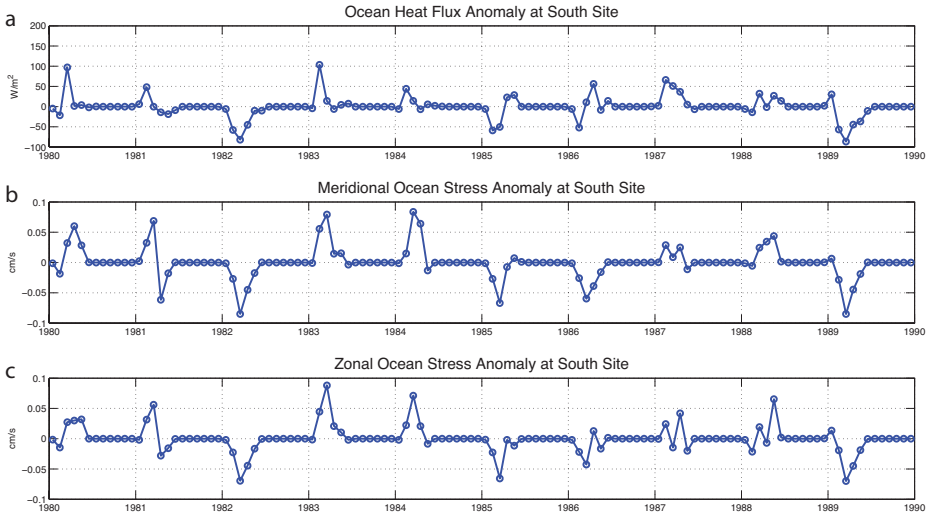

Figure 3.16: (a) Ocean heat flux anomaly, (b) meridional ocean stress anomaly, (c) zonal ocean stress anomaly averaged over the southern box in Figure 3.1.

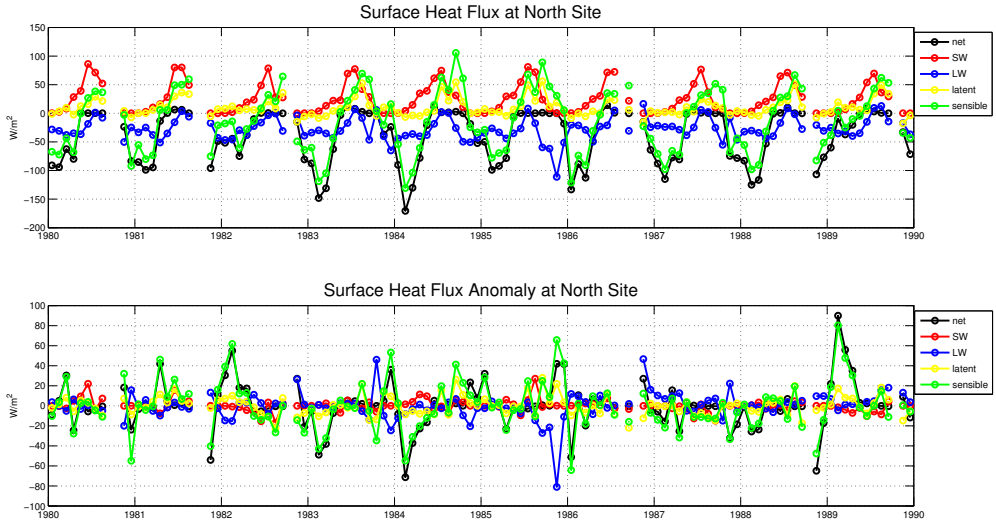

Figure 3.17: (a) Net surface heat flux (black), net shortwave radiation (red), net longwave radiation (blue), latent heat flux (yellow), and sensible heat flux (green) averaged over the northern box in Figure 3.1. (b) Anomalies of net surface heat flux (black), net shortwave radiation (red), net longwave radiation (blue), latent heat flux (yellow), and sensible heat flux (green) averaged over the northern box in Figure 3.1.

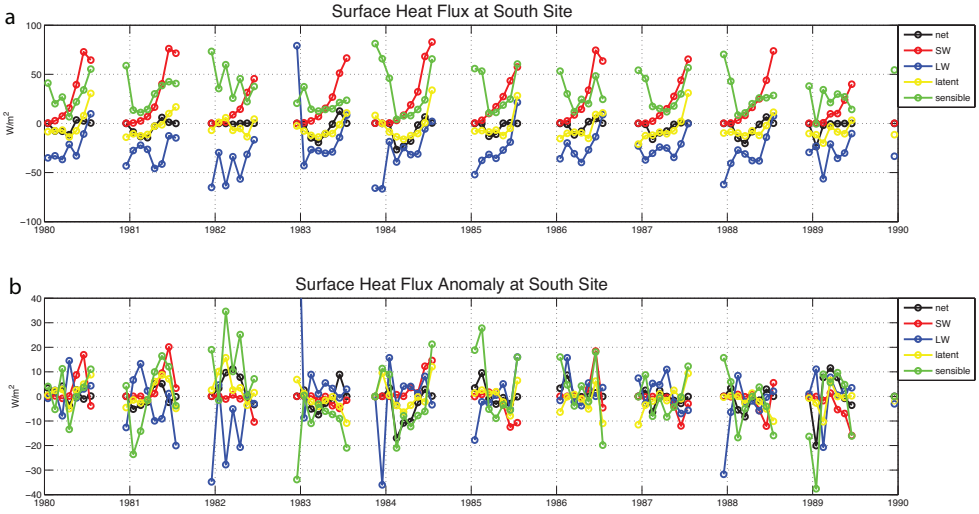

Figure 3.18: (a) Net surface heat flux (black), net shortwave radiation (red), net longwave radiation (blue), latent heat flux (yellow), and sensible heat flux (green) averaged over the southern box in Figure 3.1. (b) Anomalies of net surface heat flux (black), net shortwave radiation (red), net longwave radiation (blue), latent heat flux (yellow), and sensible heat flux (green) averaged over the southern box in Figure 3.1.

Figure 3.19: (a) Meridional components of wind stress on ice (red), ocean stress on ice (blue), Coriolis stress (green), internal ice stress (black), stress due to sea surface slope (magenta), and net stress (cyan) averaged over the northern box in Figure 3.1. (b) Zonal components of wind stress on ice (red), ocean stress on ice (blue), Coriolis stress (green), internal ice stress (black), stress due to sea surface slope (magenta), and net stress (cyan) averaged over the northern box in Figure 3.1. (c) Meridional ice velocity averaged over the northern box in Figure 3.1. (d) Zonal ice velocity averaged over the northern box in Figure 3.1. (e) Meridional components of the sum of wind stress and ocean stress (red), Coriolis stress (green), internal ice stress (black), stress due to sea surface slope (yellow), and net stress (blue) averaged over the northern box in Figure 3.1. (f) Zonal components of the sum of wind stress and ocean stress (red), Coriolis stress (green), internal ice stress (black), stress due to sea surface slope (yellow), and net stress (blue) averaged over the northern box in Figure 3.1. (g) Anomalies of meridional components of wind stress on ice (red), ocean stress on ice (blue), Coriolis stress (green), internal ice stress (black), stress due to sea surface slope (magenta), and net stress (cyan) averaged over the northern box in Figure 3.1. (h) Anomalies of zonal components of wind stress on ice (red), ocean stress on ice (blue), Coriolis stress (green), internal ice stress (black), stress due to sea surface slope (magenta), and net stress (cyan) averaged over the northern box in Figure 3.1. (i) Anomalies of meridional ice velocity averaged over the northern box in Figure 3.1. (j) Anomalies of zonal ice velocity averaged over the northern box in Figure 3.1. (k) Anomalies of meridional components of the sum of wind stress and ocean stress (red), Coriolis stress (green), internal ice stress (black), stress due to sea surface slope (yellow), and net stress (blue) averaged over the northern box in Figure 3.1. (l) Anomalies of zonal components of the sum of wind stress and ocean stress (red), Coriolis stress (green), internal ice stress (black), stress due to sea surface slope (yellow), and net stress (blue) averaged over the northern box in Figure 3.1.

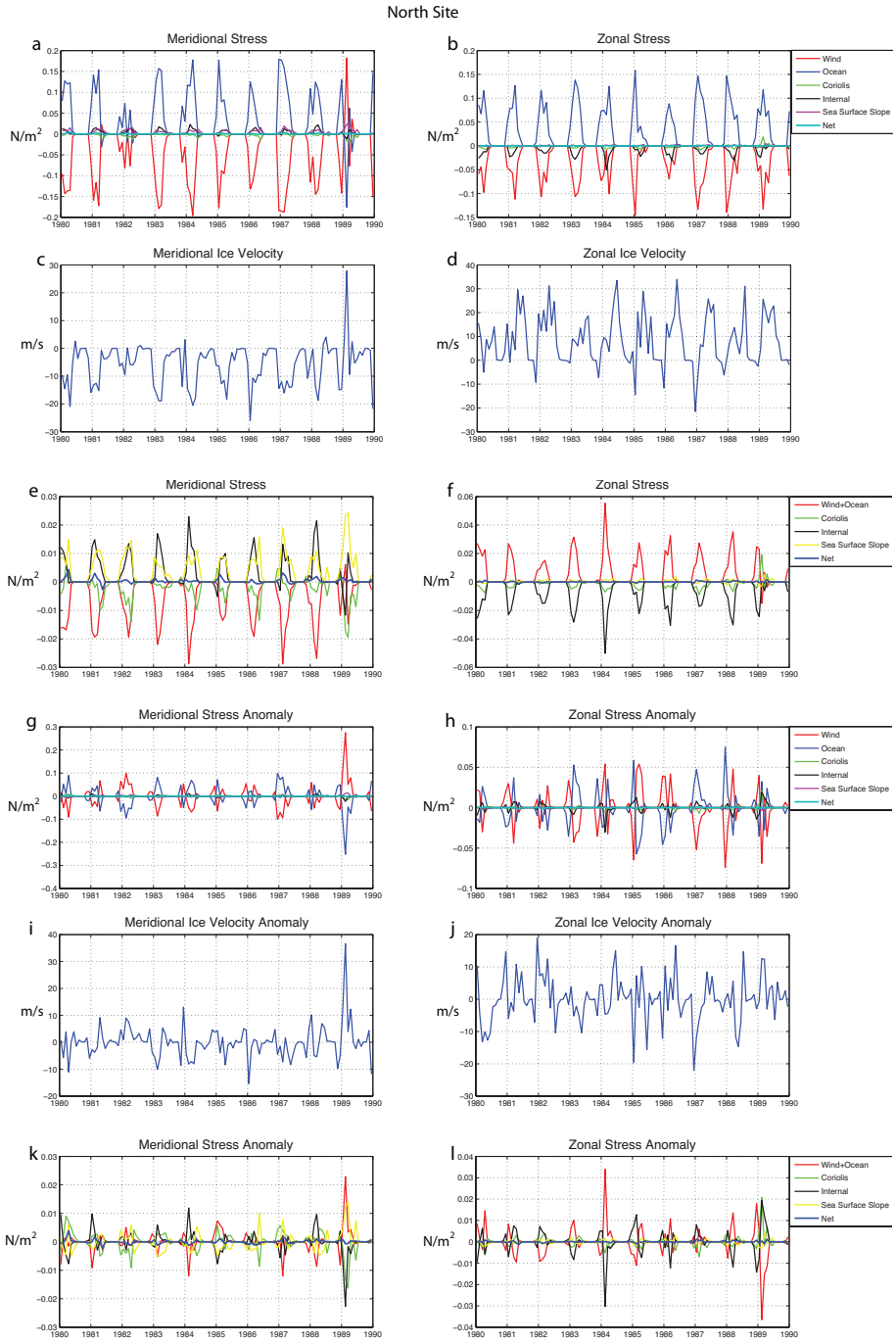
North Site
a
Meridional Stress
N/m2
b
Zonal Stress
N/m2
Wind
Ocean
Coriolis
Internal
Sea Surface Slope
Net
c
Meridional Ice Velocity
m/s
d
Zonal Ice Velocity
m/s
e
Meridional Stress
N/m2
f
Zonal Stress
N/m2
Wind+Ocean
Coriolis
Internal
Sea Surface Slope
Net
g
Meridional Stress Anomaly
N/m2
h
Zonal Stress Anomaly
N/m2
Wind
Ocean
Coriolis
Internal
Sea Surface Slope
Net
i
Meridional Ice Velocity Anomaly
m/s
j
Zonal Ice Velocity Anomaly
m/s
k
Meridional Stress Anomaly
N/m2
l
Zonal Stress Anomaly
N/m2
Wind+Ocean
Coriolis
Internal
Sea Surface Slope
Net

Figure 3.19

Figure 3.20: (a) Meridional components of wind stress on ice (red), ocean stress on ice (blue), Coriolis stress (green), internal ice stress (black), stress due to sea surface slope (magenta), and net stress (cyan) averaged over the southern box in Figure 3.1. (b) Zonal components of wind stress on ice (red), ocean stress on ice (blue), Coriolis stress (green), internal ice stress (black), stress due to sea surface slope (magenta), and net stress (cyan) averaged over the southern box in Figure 3.1. (c) Meridional ice velocity averaged over the southern box in Figure 3.1. (d) Zonal ice velocity averaged over the southern box in Figure 3.1. (e) Meridional components of the sum of wind stress and ocean stress (red), Coriolis stress (green), internal ice stress (black), stress due to sea surface slope (yellow), and net stress (blue) averaged over the southern box in Figure 3.1. (f) Zonal components of the sum of wind stress and ocean stress (red), Coriolis stress (green), internal ice stress (black), stress due to sea surface slope (yellow), and net stress (blue) averaged over the southern box in Figure 3.1. (g) Anomalies of meridional components of wind stress on ice (red), ocean stress on ice (blue), Coriolis stress (green), internal ice stress (black), stress due to sea surface slope (magenta), and net stress (cyan) averaged over the southern box in Figure 3.1. (h) Anomalies of zonal components of wind stress on ice (red), ocean stress on ice (blue), Coriolis stress (green), internal ice stress (black), stress due to sea surface slope (magenta), and net stress (cyan) averaged over the southern box in Figure 3.1. (i) Anomalies of meridional ice velocity averaged over the southern box in Figure 3.1. (j) Anomalies of zonal ice velocity averaged over the southern box in Figure 3.1. (k) Anomalies of meridional components of the sum of wind stress and ocean stress (red), Coriolis stress (green), internal ice stress (black), stress due to sea surface slope (yellow), and net stress (blue) averaged over the southern box in Figure 3.1. (l) Anomalies of zonal components of the sum of wind stress and ocean stress (red), Coriolis stress (green), internal ice stress (black), stress due to sea surface slope (yellow), and net stress (blue) averaged over the southern box in Figure 3.1.

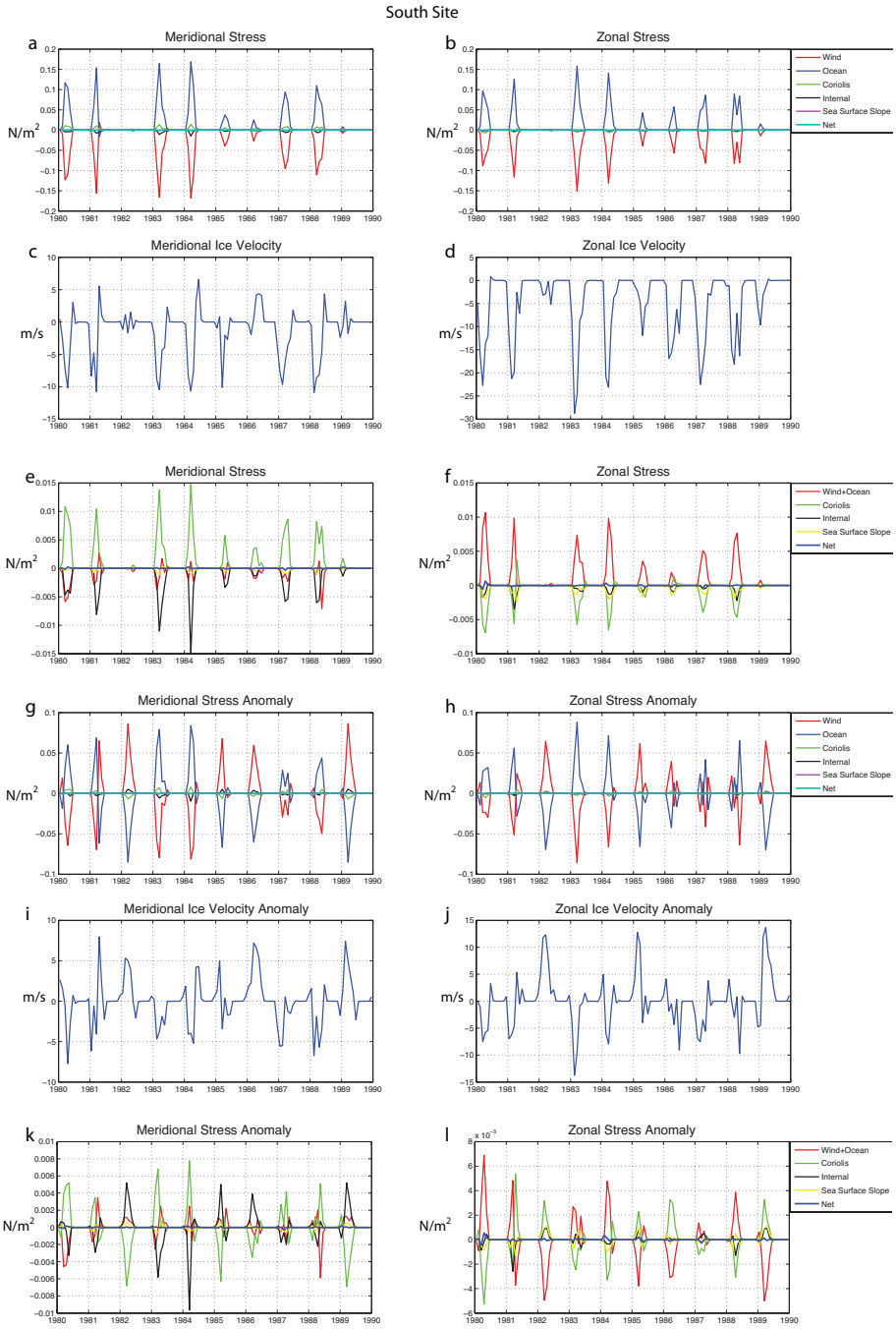
South Site
a
Meridional Stress
N/m2
b
Zonal Stress
N/m2
Wind
Ocean
Coriolis
Internal
Sea Surface Slope
Net
c
Meridional Ice Velocity
m/s
d
Zonal Ice Velocity
m/s
e
Meridional Stress
N/m2
f
Zonal Stress
N/m2
Wind+Ocean
Coriolis
Internal
Sea Surface Slope
Net
g
Meridional Stress Anomaly
N/m2
h
Zonal Stress Anomaly
N/m2
Wind
Ocean
Coriolis
Internal
Sea Surface Slope
Net
i
Meridional Ice Velocity Anomaly
m/s
j
Zonal Ice Velocity Anomaly
m/s
k
Meridional Stress Anomaly
N/m2
l
Zonal Stress Anomaly
x 10-3
N/m2
Wind+Ocean
Coriolis
Internal
Sea Surface Slope
Net
1980 1981 1982 1983 1984 1985 1986 1987 1988 1989 1990

Figure 3.20

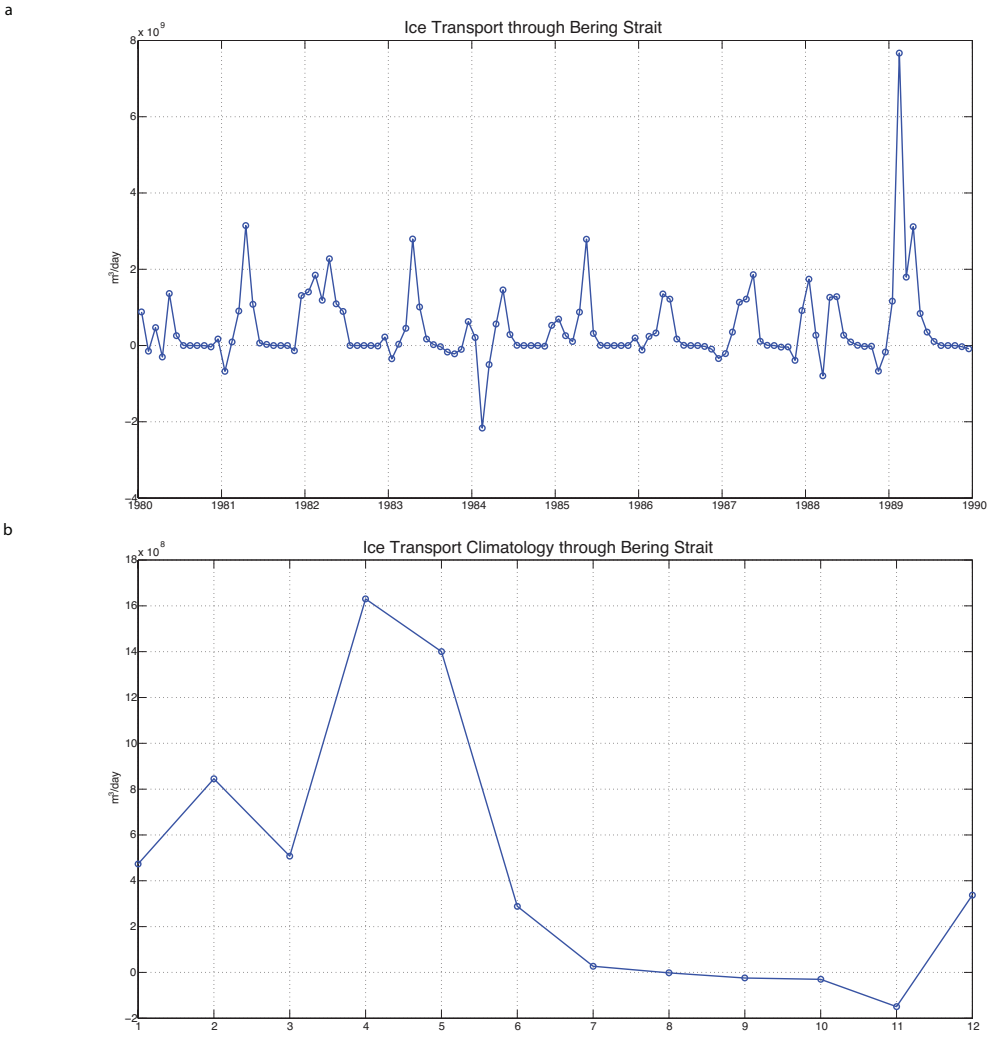

Figure 3.21: (a) Modeled sea ice transport through the Bering Strait for 1980-1989. (b) Modeled climatology of sea ice transport through the Bering Strait.

Chapter 4

Greenland Surface Lakes Observed by Repeated Laser Altimetry

Repeat laser altimetry from ICESat (Ice, Cloud, and land Elevation Satellite) has the capability to reveal the depths of Greenland surface lakes, which undergo large changes in surface elevation due to the draining and filling of the lakes. ICESat observed two types of surface lakes, supraglacial lakes on top of ice and ice-dammed lakes adjacent to glaciers. We have identified 32 active surface lakes in Greenland through ICESat repeat-track analysis. The maximum along-track depth is 55 m, and the median along-track depth is 11m. Most lakes drain completely, and a few lakes drain partially. Those 32 lakes are distributed along the coast in the northeast, in the west, and in the northwest of Greenland. No lakes were detected by ICESat in the southeast. Lakes at higher latitudes usually lie at lower elevations. Those lakes are near the equilibrium line, and many of them are close to outlet glaciers. The ICESat-detected lakes are deep, and mostly ice covered. Time series of lake surface elevations show that filled lakes can survive stably for several years and do not drain every year. Some nearby lakes have a high temporal correlation in lake level elevation, draining almost simultaneously.

We have developed a method of constructing the three dimensional geometry of supraglacial lake basins, using combined elevation measurements of the lake

basin from multiple campaigns, which is shown to be adequate through validation with high-resolution airborne laser altimetry. We have estimated the volume of water contained in the lakes at different times, by combining the constructed geometry of the lake basins and water level measurements or combining altimeter data and satellite images. The aspect ratios of individual supraglacial lakes can be quite different, but the volume estimates are similar. The volume estimate of a typical supraglacial lake is $3 \times 10^7 m^3$. Water volume estimates of a filled lake at different times can be very similar. The volume of water involved in the drainages of the ice-dammed lake beside Petermann Glacier is much larger, estimated to be $66 \times 10^7 m^3$ in 2005 and $90 \times 10^7 m^3$ in 2008. Compared to the estimated Greenland ice-sheet mass loss, which is $232 km^3 year^{-1}$ water-equivalent over the period October 2003- December 2008 (Shepherd et al., 2012), these lake drainage events are small. However, they may play an important role in changing ice velocities at the margin of the Greenland Ice Sheet.

4.1 Introduction

Surface melting at the margin of the Greenland Ice Sheet, which is one of the focal points in global climate change research, has increased significantly over the past decades (Abdalati and Steffen, 2001; Hanna et al., 2005; Mote, 2007; Bhattacharya et al., 2009; Fettweis et al., 2011; Mernild et al., 2011). Surface melt water can either accumulate in surface depressions on impermeable ice to form supraglacial lakes and rivers, or percolate through crevasses. Supraglacial lakes contain a large portion of meltwater accumulation and can drain rapidly, within a few hours (Das et al., 2008) to a few days (Box and Ski, 2007).

The large amount of surface melt water in the lakes could flow englacially, e.g. through moulins to the ice-bedrock interface, and thereby influence ice dynamics (Das et al., 2008). The amount of surface melt has been correlated to ice velocity change, either to ice velocity increase due to inefficient subglacial drainage systems (Zwally et al., 2002; Joughin et al., 2008) or to ice velocity decrease due to efficient subglacial drainages systems (Shepherd et al., 2009; Sundal et al., 2011).

The effect of surface melt on ice velocity is mainly seasonal (Joughin et al., 2008; Bartholomew et al., 2010; Sole et al., 2011; Hoffman et al., 2011), in which, at the early stage of the melting season, surface melting causes acceleration of the ice flow as a result of an inefficient subglacial drainage system. As the amount of surface melt increases to a certain level, the subglacial drainage system becomes more efficient. The velocity drops, to even lower levels than in winter, though the amount of surface melt continues to increase to its maximum values at the end of summer.

The long-term mean surface meltwater input rate determines the configurations of the subglacial drainage systems. However, the subglacial drainage systems take a few days to adjust to varying water input. Short-term variability in water input (i.e. diurnal melt cycles (Shepherd et al., 2009), rain, and lake drainages) usually causes ice acceleration, because subglacial drainage systems are unable to adapt immediately. In particular, the abrupt drainage of large volumes of water from supraglacial lakes could pressurize the subglacial drainage systems and accelerate ice flow locally and temporally (Schoof, 2010; Hoffman et al., 2011). In addition, the volume of water in the lakes also affects whether water-filled cracks can propagate through the ice sheet to cause the drainage of supraglacial lakes (Krawczynski et al., 2009).

Lastly, the drainage of supraglacial lakes could be an important factor in the Greenland Ice Sheet's mass balance and its contribution to sea level rise, which ice sheet modeling should incorporate. It is therefore important to quantify the volume of water involved in these lake drainage events.

We consider here the draining and filling of Greenland surface lakes by detection of large surface elevation changes in ICESat (Ice, Cloud, and land Elevation Satellite) laser altimeter data. Repeat-track analysis of ICESat laser altimeter data can reveal the depths of surface lakes by detecting the difference of surface elevations of filled and drained lakes. We use this data set to develop a technique to construct the three dimensional geometry of key lake basins, which allows us to estimate the volume of water contained in any given lake that is detected by ICESat. This leads to a time series of estimated water volume for an individual lake.

This framework can eventually be applied to all the identified lakes to determine their total contribution to the time-dependent mass budget of the Greenland Ice Sheet.

4.2 Methods

Laser altimeter data collected by the Geoscience Laser Altimeter System (GLAS) onboard NASA's ICESat provide changes in surface elevation from 86°N to 86°S from repeat-track measurements.These data were collected during several "campaigns" (measurement time periods) from 2003 to 2009. GLAS has three laser altimeters Laser 1 (L1), Laser 2 (L2), and Laser 3 (L3). The 1064 nm channel for altimetry has a 2 cm precision. The footprint of the laser beam on the ground has a diameter of between 50-70 m, and consecutive footprints along the same track are separated by 172 m when the satellite is at 600 km altitude. The track separation is $\sim 15km$ at 80° latitude. Due to problems discovered with the lasers during the L1 operation, L2 and L3 were operated intermittently for several campaigns from 25 September 2003 to 11 April 2009. The tracks of the last 33 days of Laser 2a (L2a) were repeated in subsequent campaigns. Figure 4.1 shows the operational time periods of ICESat campaigns. Table 4.1 lists the 17 ICESat campaigns and their corresponding operation times. ICESat operated two or three times per year from 2003 to 2009; usually with one campaign occurring around March, one campaign around October/November, and occasionally another campaign around June.

We focus on the ICESat repeat-track laser altimeter data that reveals surface elevation changes of surface lakes in Greenland. The repeat-track analysis of ICESat data often reveals large elevation changes due to the draining and filling of these surface lakes (Figure 4.2). The surface lakes form locally in low topography. The repeat ICESat tracks show that the surface elevation switches between two states, flat and high, and concave and low (Figure 4.2a,c). We demarcate lakes with "large" elevation changes as those exceeding 2m. We interpret the flat surface to be the surface of a filled lake, and the concave profile to be that part of the lake basin that has been partially or completely drained.

We have also examined optical satellite images of several lakes detected by ICESat. The ASTER (Advanced Spaceborne Thermal Emission and Reflection Radiometer) satellite images can reveal the surface horizontal spatial extents of the lakes in relation to the ICESat ground tracks at a spatial resolution of 15 to 90 m. Furthermore, the MODIS (Moderate Resolution Imaging Spectroradiometer) satellite images, which have higher temporal resolution (1 to 2 days) and lower spatial resolution (250 m, 500 m, 1000 m depending on bands), can also reveal the temporal evolution of the lakes, e.g. draining and filling.

Since the ICESat tracks may not transect the center of the lake, the actual water depth cannot the directly measured. We use images of the lakes from ASTER and MODIS to determine where the ICESat tracks transit the lakes. If the satellite transects the lake near the center, we can safely assume that the lake is drained completely from observation of concave profiles.

4.3 Results

4.3.1 Typical ICESat observations of surface lakes

ICESat detected two types of surface lakes, supraglacial lakes on top of ice and ice-dammed lakes adjacent to glaciers. Key examples of ICESat observations of a supraglacial lake and an ice-dammed lake are shown in Figure 4.2a and Figure 4.2c respectively. The supraglacial lake in Figure 4.2a is in the west of Greenland (67.735° N, -48.05° E). It has a very simple elliptical surface area and is often ice covered as shown in the MODIS (Moderate Resolution Imaging Spectroradiometer) satellite image in Figure 4.2e. This lake has an along-track length of 1.8 km and an along-track depth between 10 m and 15 m. We can see the draining and filling cycles of this lake in Figure 4.2a. It drained between 20 May 2004 and 22 May 2005 with an elevation decrease of 15 m, filled between 26 May 2006 and 27 October 2006 with an elevation increase of 9 m, drained between 13 March 2007 and 4 October 2007 again with an elevation decrease of 10 m, and filled between 19 February 2008 and 6 October 2008 again with an elevation increase of 8 m.

The ice-dammed lake (80.25° N, -60.2° E), shown in Figure 4.2c, is on the

western margin of Petermann glacier, just upstream from the grounding line, as shown in the ASTER (Advanced Spaceborne Thermal Emission and Reflection Radiometer) satellite image in Figure 4.2e. This lake has a very large, irregular area of $45.6km^2$, as estimated from the ASTER satellite image, with large depth. The lake drained between 23 May 2005 and 24 October 2005 with an elevation decrease of 14 m. Another drainage event occurred between 20 Feb 2008 and 7 October 2008 with an elevation decrease of 18 m. However, the lake never appears to drain completely.

These two representative lakes (one typically sized supraglacial, and one very large ice-dammed) indicate substantial elevation changes in their water levels. We next attempt to quantify how many lakes occur over Greenland in the ICESat observations, along with their sizes, locations, and filling/draining statistics.

4.3.2 Statistics of surface lakes detected by ICESat

We have identified 32 active surface lakes in Greenland through this ICESat repeat-track analysis. Their spatial distribution is represented as red pluses shown in Figure 4.2e. They are distributed near coastal regions in the northeast, west and northwest of Greenland. The ICESat tracks of campaign L2b (17 Feb 2004 - 21 Mar 2004), color-coded with the WGS-84 elevation, show the ICESat spatial coverage of the entire Greenland ice sheet and its large-scale elevation. ICESat has dense sampling in northern Greenland where in-situ observations are rarely available, thus providing a comprehensive and reliable monitoring over the high latitude part of Greenland. In southeastern Greenland where large ice loss from fast glacier flow into the ocean occurs, ICESat does not detect surface lakes with large elevation changes. This is possibly due to the large separation of different ICESat tracks and thus sparse spatial sampling in southern Greenland. It is also very likely that the steep and crevassed surface of the ice sheet in southeastern Greenland is not favorable for the formation of large surface lakes (Sundal et al., 2009).

The median along-track length of the 32 lakes identified here is 1.7 km, the mean is 2.2 km, the minimum is 0.4 km, and the maximum is 13 km. The elevation

drop due to lake drainage as determined from ICESat can be as large as 55 m, and the median value is 11 m, the mean value is 13.6 m, and the standard deviation is 11 m. Most lakes drained completely, but a few lakes only drained partially to halfway. These two types of drainages imply different drainage mechanisms, which will be discussed later. Next we will examine the temporal structure and coherency between drainage events of different lakes.

4.3.3 Temporal variability and correlation of lake surface elevations

We have examined the time series of the surface elevation observed at each of the 32 lakes detected by ICESat. The time series of surface elevation reveals cycles of draining and filling of the lakes. As shown in Figure 4.2b, the supraglacial lake in the west drained and filled repeatedly, draining in 2004, remaining empty in 2005, filling in 2006, draining again in 2007, and filling again in 2008. The period of this draining and filling cycle is approximately 2 years, except that it stayed empty in 2005. In Figure 4.2d, the ice-dammed lake near Petermann Glacier in the north has fluctuating water levels but never was observed to drain completely. The water level stayed almost constant through most winters e.g. around 1 Jan 2004, 2005, 2006, 2008 and 2009. The water level increased slowly, by $\sim$5 m in one year, if no drainage event was observed to occur during the interim, e.g. in 2004, 2006 and 2007. This lake drained large amounts of water in 2005 and 2008, with the water level dropping $\sim$14m in 2005, and $\sim$18m in 2008. The drainage of this lake occurs abruptly at an apparent critical triggering water level suggested by the water levels immediately before drainage (229 m in 2005 and 225 m in 2008).

Note that these lakes do not drain every year. A filled lake can survive stably for several years. All of these lakes drained once or twice over the 5.5 year record available from ICESat observations. Due to poor temporal resolution and limited available cloud-free campaigns of ICESat, multiple drainage events between consecutive campaigns, if any, cannot be resolved. Most drainage events happened in the summer, but a few drainage events occurred in other seasons. For example, one lake in northern Greenland (81.34 ° N, -31.945 ° E) with along-track length of

1.8 km drained completely with an elevation drop of 20 m between 4 March 2005 - 3 June 2005. Another lake in the north (79.28 ° N, -25.100 ° E) with along-track length of 2 km drained with an elevation change of 5 m between 18 Oct 2004 - 5 March 2005.

We next examine the correlation of the time series of surface elevation of different lakes. Some lakes show high correlation in lake-level elevation, draining and filling almost simultaneously. For example, high correlation ($\sim$ 0.9) exists between 3 lakes near Petermann Glacier, Humboldt Glacier, and Ryder Glacier separately. They drained twice, nearly simultaneously, in the summers of 2005 and 2008. Through examining daily MODIS images of the lakes for the exact drainage dates, the lake near Humboldt Glacier drained during 3 July - 8 July 2005, and the lake near Ryder Glacier drained during 8 July - 11 July 2005. This correlation may be due to some common meteorological factors or some hydrological connections, which will be discussed later.

The large changes observed in lake elevation suggest large volumes of water are discharging from the lakes. We next estimate the magnitudes of these drainage events.

4.3.4 Lake water volume and drainage estimation

In order to estimate the water volume of the drainage from a lake, we must know the geometry of the lake and the water level. The water level is directly measurable from ICESat, but the geometry must be estimated. If a lake has vertical sides and a known horizontal area, this estimate is simple and direct. For example, the ice-dammed lake (80.25 ° N, -60.2 ° E), shown in Figure 4.2c, has a large area ($45.6 km^2$) and nearly vertical walls at its boundaries. The volume of lake water drained can then be easily computed from the area and the elevation change. It drained $0.66 km^3$ between 23 May 2005 and 24 October 2005 (elevation decrease of 14 m) and $0.90 km^3$ between 20 Feb 2008 and 7 October 2008 (elevation decrease of 18 m). This large amount of water might influence ice dynamics locally if it drained subglacially, and could finally drain into the ocean. Other lakes with varying depths require more detailed modeling of the depth structure, which we

next address.

3D geometry of lake basins

The repeat-track ICESat laser altimeter data can reveal the depth of supraglacial lakes by detecting the difference of surface elevations of filled and drained lakes. The flat and high surface elevation profiles are typical of a filled lake, while the low and concave elevation profiles represent the shape of the lake basin of a drained lake.

The relatively large elevation differences of lake basin topography between different campaigns is mostly due to the cross-track offset of tracks in different campaigns and the large cross-track slope of lake basins. This information, however, can be used to estimate the local cross-track slope of lake basins. Also, ICESat tracks do not necessarily cross the deepest parts of lakes, and thus the apparent depths are lower than the true maximum depth of the lake. We have to consider the locations of ground tracks relative to each other and relative to the lake to infer the maximum depth.

We can therefore combine the elevation measurements of the lake basin from multiple campaigns with cross-track separation of a few hundred meters to construct the three dimensional geometry of a supraglacial lake basin.

We first perform triangulation interpolation of multiple elevation measurements of the lake basin. We can see local 3D topography in a band around the ground tracks. The cross-track slope is revealed and can indicate the maximum depth of the lake and where it is located.

An example of applying this strategy to a supraglacial lake near Ryder Glacier in northern Greenland (81.00° N, -49.74° E) is shown in Figure 4.3. In Figure 4.3a, ICESat ground tracks are overlaid on an ASTER image. Those repeat tracks are offset by a few hundred meters. In Figure 4.3b, the elevation difference between flat elevation profiles of the filled lake and concave elevation profiles of the drained lake can be as large as $\sim 50m$ with along-track length $\sim 1.14km$. The interpolated lake basin from ICESat measurement reveals part of the 3D basin topography, as shown in Figure 4.3c,d.

In order to construct a simple model of lake geometry, we assume that the shape of a lake basin is rotationally symmetric with a vertical axis and time-invariant. We have examined many satellite images, elevation profiles and airborne photographs of the lakes, and rotationally symmetric geometry around a vertical axis is an adequate approximation for most lakes detected by ICESat. Also, large supraglacial lakes usually form at almost the same locations on ice surface depressions corresponding to bedrock topography depressions (Echelmeyer et al., 1991; Jezek et al., 1994), and do not advect with ice flow (Echelmeyer et al., 1991; Selmes et al., 2011). The inter-annual variation of lake basin elevation from repeat airborne laser altimeter data is about 1-2 m (McMillan et al., 2007), consistent with typical surface elevation variation 1 - 2 m due to accumulation and ablation (Box et al., 2006). This 1-2 m fluctuation in lake basin elevation is much smaller than the typical depth 10-20 m of those lakes detected by ICESat.

We have developed a method of fitting a model of the geometry of a lake basin to ICESat measurements of the lake basin when a lake is drained. The geometry of the lake basin is assumed to be rotationally symmetric around a vertical axis. We tried different shapes, e.g. cone, quadratic symmetry, rotational symmetry with any power, Gaussian symmetry, etc., and compared the fitting results of different shapes. The best fit for the shape of the supraglacial lake basin near Ryder Glacier is a Gaussian function:

$$z(x,y) = z_0 - D_0 exp[\frac{(x-x_0)^2+(y-y_0)^2}{2\sigma^2}].$$

where x and y are horizontal coordinates in km in NSIDC's polar stereographic north projection. z is the elevation in m relative to the WGS 84 ellipsoid. x_0 and y_0 are the lake center's horizontal location in km in NSIDC's polar stereographic north projection. z_0 is the maximum lake basin elevation in m relative to the WGS 84 ellipsoid, which is close to the elevation of the edge of the lake basin, and water levels should not exceed this threshold. D_0 is the height of the Gaussian function, and represents the maximum possible water depth. σ is the variance of the Gaussian function, and 4σ is the characteristic diameter of the lake. The fitted model parameters for this lake are listed in Table 4.2. This lake basin has a Gaussian shape with a height of 62 m and a characteristic diameter of 1.7

km. This lake centers at (-81 km, -970 km) in NSIDC's polar stereographic north projection, and the elevation of the lake basin is 850-910 m above the WGS 84 ellipsoid. Figure 4.3e,f show the constructed Gaussian shape of this lake basin.

Volume and drainage calculations

After obtaining the best fit of the geometry of a lake basin, we can estimate the volume of lake water at different ICESat repeat-track times. ICESat can measure water levels when the lake is not empty as long as the ICESat track samples the lake surface. We use horizontal surfaces at the elevations of those water levels that intercept the modeled lake basin to compute the water contained in the lake. Then we can estimate the maximum lake depth, lake area, and volume of lake water at different times.

Table 4.3 lists estimated maximum depths, areas, and volumes of lake water for the supraglacial lake basin near Ryder Clacier for each of the available campaigns. This lake contained similar amounts of water between 13 March 2004 and 14 June 2005. Sometime between 14 June 2005 and 15 November 2005, the lake drained $0.031km^3$ of water. It remained empty from 15 November 2005 to 18 June 2006, and then filled with $0.028km^3$ of water between 18 June 2006 and 27 October 2007. Another drainage event between 13 March 2008 and 09 December 2008 drained $0.025km^3$ of water. The relatively constant volume of lake water when the lake is filled may be controlled by the topography (Echelmeyer et al., 1991; Jezek et al., 1994), and is consistent with the almost constant area covered by the lakes (Luthje et al., 2006).

4.3.5 Validation of lake geometry estimation and water level using independent data

Lake bathymetry validation

Our estimates of the lake volume and drainage events can be partially validated by comparing these results with other remotely sensed data. NASA's Laser Vegetation Imaging Sensor (LVIS) is an airborne scanning laser altimeter instru-

ment that flew over one empty Greenland lake that was sampled by ICESat. LVIS gives a higher resolution measurement and better coverage of the empty lake structure. However, it sampled the lake when it was empty, so that changes in water levels were not available. We next use the LVIS observations at this lake to compute an independent estimate of lake geometry and then compare it with the results using our method with ICESat data.

On 20-21 September 2007, LVIS flew along ICESat tracks 419, 204 and 412 in Greenland, at an altitude of 7600-8300 m, with a 1.1-1.5 km swath, and 20-25 m slightly-overlapping footprints. On track 419, LVIS and ICESat both sampled a supraglacial lake in West Greenland (67.76° N, -47.92° E; see Figure 4.4g), which was empty at the time of the LVIS flight on 20-21 September 2007. ICESat observations show that this lake was full on 14 April 2007 with a maximum depth $> 11m$ and an along-track width $\sim 2.5km$. This indicates that drainage occurred during the interim period.

We have constructed a model of the geometry of this particular lake basin from ICESat data using the method described earlier (Figure 4.4d,e,f). We have fitted the shape of this lake basin with a 2D Gaussian function (parameters are listed in Table 4.2) with a height of 19 m and a characteristic diameter of 3.1 km. This lake model centers at (-123.79 km, -2436.00 km) in NSIDC's polar stereographic north projection, and the elevation of the lake basin is 1582-1601m above the WGS 84 ellipsoid. This model result from ICESat data is qualitatively consistent with the LVIS scanning measurements in terms of maximum depth, horizontal sizes, area, shape, etc, as seen by comparing Figure 4.4e,f with Figure 4.4b,c.

We have also fitted the LVIS data to a 2D Gaussian model (see parameters in Table 4.2) for the shape of this lake basin with a height of 20 m and a characteristic diameter of 3.3 km (Figure 4.4h,i). This lake model centers at (-123.68 km, -2436.00 km) in NSIDC's polar stereographic north projection, and the elevation of the lake basin is 1581-1601m above the WGS 84 ellipsoid. This model should be considered more accurate because of the higher quality LVIS data.

We have compared these two models, obtained from independent LVIS and

ICESat observations, as shown in Figure 4.4e,f and Figure 4.4h,i. These two models are very similar, though the size (e.g. depth) of the LVIS model is a little larger (1.1 m deeper at the center) than in the ICESat model. The volume and area estimates at different times from these two models are very close, though the depth, area and volume estimates from ICESat model are a little lower than those from LVIS model (Table 4.4). Though ICESat measurements have relatively sparse coverage and larger spot sizes, the resulting 3D topography is nearly as good as that from high-resolution LVIS measurement.

Water level validation

LVIS also provides a means to test the accuracy of the water level measurements from ICESat, which is the key variables for estimating water volume as a function of time. On track 419, ICESat and LVIS both sampled a filled supraglacial lake in West Greenland (68.18° N, -48.16° E). The L3i campaign of ICESat (Nov 4, 2007) and LVIS (Sep 20/21, 2007) detected a nearly flat surface on that filled lake within 1.5 months of each other, which has much higher temporal resolution than individual ICESat campaigns. This provides a chance to compare the performance of ICESat and LVIS on a nearly flat surface. Comparing ICESat measurements and LVIS interpolated values at the same locations along the track, we find that the mean difference is 0.0092 m, the median is 0.0094 m, and the maximum is 0.1388 m. Compared to the size of the water level changes observed by ICESat, roughly 10m between campaigns, the elevation differences between ICESat and LVIS over a nearly flat surface are very small. Water level observations from ICESat are therefore reliable.

Lake area validation

We have also compared lake areas from the constructed geometry model of lake basins from ICESat data with Moderate Resolution Imaging Spectroradiometer (MODIS) satellite images on the same dates of ICESat detection. The results for the same lake in Figure 4.4 are shown in Table 4.5. The areas from the model are comparable to the areas estimated from the images, although they tend to be

somewhat smaller. However, the low-resolution (250 m) MODIS images have large uncertainty in quantifying lake areas.

In summary, the modeled geometry of lake basins using ICESat data is adequate, given this validation using LVIS high-resolution airborne laser altimeter data and MODIS satellite imagery. This method of modeling the 3D geometry of the lake basin from ICESat data can therefore be used in other lakes.

4.4 Discussions

The results of our analysis raise several interesting points that require further discussion. These include the issues of the aspect ratio of supraglacial lakes, the mechanisms for drainage events, the spatial distribution of the lakes, temporal evolution of the water levels, correlations among lake water levels, and lake depth estimation. We discuss these issues here, relate previous work to our results, and speculate on various topics.

4.4.1 Geometry of supraglacial lakes

The aspect ratio (width to depth) is often an assumed parameter (typically 100:1) for estimating the volume of supraglacial lakes from satellite images, which can only show area (e.g. Krawczynski et al. (2009)). Our results reveal that aspect ratios vary widely depending on the location in Greenland and the local geography. For example, the lake near Ryder Glacier in northern Greenland has an aspect ratio about 26:1 (deep and narrow), while the lake in western Greenland validated with LVIS observation has an aspect ratio about 166:1 (shallow and wide). Though the shapes of these two lakes are quite different, they contain similar volumes of water on the order of $10^7 m^3$. These two types of lake shapes are also observed in satellite images based on relations between reflectance and depth of ice-free lakes (Box and Ski, 2007).

4.4.2 Mechanisms for drainage of surface lakes

The mechanisms for instigating lake drainage events are not well understood. Draining of supraglacial lakes may be largely triggered by intense surface melting and heavy rainfall. Partial-draining and complete-draining events have been previously observed by satellite images (Box and Ski, 2007; McMillan et al., 2007). and our ICESat analysis confirms these two types of events. From our analysis of ICESat observations, most lakes drained completely to the bottom. This type of drainage is probably triggered by moulin or crack formation at the bottom of the lake basin, and could occur abruptly in a few hours (Das et al., 2008). Several lakes, though, only drained partially. The drainage mechanism may be supraglacial overspilling through outlet streams into moulins nearby or into other lakes, possibly forming an ice canyon through the lake bank, which could take a few days.

Ice-dammed lakes are filled with meltwater, streamflow and precipitation. Once lake water reaches some critical high level, drainage can occur in several ways. A channel can form englacially or subglacially which drains lake water away (Russell et al., 1990; Huss et al., 2007). Lake water can overflow and cut through the ice dam (Raymond and Nolan, 2000) or trigger subglacial drainage. Drainages through subglacial channels could cause nearly vertical shear motion of a block of ice, possibly along a fault near the ice dam (Russell et al., 1990; Walder, 2005). The duration of drainages of ice-dammed lakes can be a few hours (Russell et al., 1990) to a few days (Huss et al., 2007).

From ICESat observations, the ice-dammed lake beside Petermann Glacier in northern Greenland drained twice over the 5.5 year period of the ICESat operation. Due to its large capacity, it takes several years to fill up this lake until drainage occurs. The critical water depths immediately before the drainages detected by ICESat were 229 m on 23 May 2005 and 225 m on 20 Feb 2008. The water level dropped 14 m between 23 May 2005 and 24 October 2005, and again dropped 18 m between 20 Feb 2008 and 7 October 2008. The drainages involved large amounts of water: $0.66km^3$ in 2005 and $0.90km^3$ in 2008. The volume of water drained from this ice-dammed lake is 20-30 times larger than the typical

volume of water drained from a supraglacial lake, $0.03km^3$. Thus, an ice-dammed lake is likely to be more important than a supraglacial lake in influencing the mass balance of the ice sheet.

It is possible that subglacial drainage tunnels form as large volumes of water drain from this ice-dammed lake. Perhaps these tunnels at the ice-rock boundary on land connect to basal channels beneath the floating tongue (over the sea) of Petermann Glacier (Rignot and Steffen, 2008), so that subglacial water could flow along these continuous paths from land to ocean. Additional observations are required to support this speculation.

4.4.3 Spatial distribution of supraglacial lakes

The supraglacial lakes are not distributed uniformly over Greenland, but instead tend to cluster in certain locations. The spatial distribution of ICESat detected lakes concentrates in the west, the northwest and the northeast of Greenland. This pattern is consistent with previous work on the spatial distribution of all the lakes detected in MODIS images for the entire Greenland Ice Sheet. In those satellite images, most of the regions of Greenland (northwestern, northeastern, and western) have similar maximum fractional area covered by lakes (Sundal et al., 2009). In the southeast, however, lake coverage is smaller (Selmes et al., 2011). Our ICESat results are consistent with this distribution. These two independent methods both detected very few lakes in the southeastern Greenland and clustering of lakes near coastal regions in the northeast, west and northwest of Greenland (Selmes et al., 2011). We now speculate on the physical mechanisms that may lead to this distribution.

Through the examination of satellite images we have noticed that many large supraglacial lakes detected in ICESat data are located close to and upstream of glaciers. That might be the result of bedrock topography and the corresponding ice surface topography. Ice flow follows the gradient of bedrock topography. At large scales, the ice surface topography reflects the bedrock topography beneath it. Surface melt water flows along the gradient of the ice surface, generally in a direction similar to the ice flow. Thus, surface melt water flows towards glaciers.

The coastal areas have large undulations in topography. Surface melt water can accumulate in large surface depressions close to glaciers. On the other hand, the drainage of those lakes near glaciers may influence ice dynamics of the nearby glaciers if the lake water is drained subglacially. It is also likely that the drained water moves across the grounding line or the edge of the glaciers and discharges into the ocean subglacially. The fresh melt water can influence the ocean circulation near glaciers, and cause large basal and frontal melting of marine-terminating glaciers, e.g. through turbulent mixing at the ice-ocean interface.

The large supraglacial lakes detected by ICESat are at relatively high elevation close to the equilibrium line, the boundary between the zone of accumulation and the zone of ablation. At relatively high elevations close to equilibrium line where ice is compressed, surface melt water can flow along the surface in supraglacial rivers, accumulate in supraglacial lakes and drain through moulins inefficiently, possibly causing ice acceleration. Supraglacial lakes there can be very deep (maximum depth is 55 m from ICESat data) and stable, and most of them are ice-covered based on combined observations of ICESat and satellite images. It is also near the equilibrium line of western Greenland that correlation between surface melting and ice flow acceleration has been observed (Zwally et al., 2002). Similarly, drainages of lakes observed by ICESat that are near equilibrium line are likely to accelerate ice locally. In a low elevation runoff zone with many crevasses, surface melt water can drain through crevasses efficiently and cause less ice acceleration than at higher elevation (Colgan et al., 2011). This explanation is consistent with the observation that summer speed-up of ice flow is less obvious at the ice margin than further inland (Joughin et al., 2008). Many small and active melt ponds can exist in these low elevation areas, based on satellite imagery (Box and Ski, 2007; McMillan et al., 2007; Selmes et al., 2011; Lampkin, 2011). In contrast, large and stable supraglacial lakes were not detected to form in such crevassed areas using ICESat data, suggesting they are difficult to form in such locations.

Because tensile stress is proportional to the local surface slope, along the steep margin of the Greenland Ice Sheet large tensile stress produces lots of crevasses. In contrast, compression dominates in lake and river-covered areas fur-

ther inland where there are small surface slopes. There may also be a feedback from the ice acceleration to the drainage of surface melt, because ice acceleration can also produce crevasses that enhance the drainage of the surface melt. This may explain why ICESat did not detect any large surface lakes in southeastern Greenland where ice discharge dominates mass loss (Sundal et al., 2009; Selmes et al., 2011). It is possible that the existence of large and stable supraglacial lakes is a sign of stable ice flow conditions e.g. in the northwest and northeast of Greenland. This perspective is in contrast to the intuition that supraglacial lakes are signatures of warming and consequent ice mass loss.

4.4.4 Temporal evolution of lake water volume

Many previous estimates of supraglacial lake volumes were based on the area of the lakes seen in satellite images. The total area of supraglacial lakes exhibits seasonal variations, based on satellite imagery that has much higher temporal sampling than the ICESat data (Sneed and Hamilton, 2007; McMillan et al., 2007; Sundal et al., 2009; Georgiou et al., 2009). In western Greenland, lake coverage increases early in the melting season, e.g. in May and June in 2001 near Swiss Camp (McMillan et al., 2007), and most lakes drain in the middle of the melting season e.g., in July (Box and Ski, 2007; McMillan et al., 2007). The evolution of total lake area in northern Greenland is delayed by 2-3 weeks relative to that in western Greenland (Sundal et al., 2009).

This seasonal evolution of supraglacial lakes depends on elevation and latitude. The lakes form and drain earlier at low elevations and low latitudes than the lakes at high elevations and high latitudes. The evolution of supraglacial lakes also propagates inland and northward during the melt season (McMillan et al., 2007; Sundal et al., 2009; Bartholomew et al., 2010). In different regions, e.g. western versus northern Greenland, the seasonal evolution of supraglacial lakes may vary due to different meteorological conditions and geographical settings. Air temperature can influence the onset of lake filling and the timing of maximum lake area, and the maximum altitude where supraglacial lakes could exist.

The ICESat observations revealed that a lake frequently contains nearly the

same volume of water, which appears to be its maximum volume. This suggests that when a lake is filled to its maximum, it possibly overflows through outlet streams (Luthje et al., 2006) to maintain this constant volume which is determined by the local ice surface topography. Englacial/subglacial drainage could also occur once a lake is filled to a critical level. For example, the lake near Ryder Glacier in northern Greenland was observed to contain $\sim 3 \times 10^7 m^3$ of water on several occasions when it is filled. During the other times it was measured, this lake was empty, suggesting rapid drainage. Since ICESat did not measure the onset of melting in early summer, the rate of filling could not be determined from this dataset.

4.4.5 Correlation of water levels among lakes

As mentioned previously, three lakes near Petermann Glacier, Humboldt Glacier, and Ryder Glacier in Northern Greenland drained twice almost simultaneously in the summers of 2005 and 2008, based on our analysis of ICESat observations. Their drainages may have common controlling meteorological factors, e.g., warm air outbreaks, heavy rainfall events, etc. We studied the daily MODIS images at the beginning of July 2005, which is immediately before the drainages of the lakes near Humboldt Glacier and Ryder Glacier. These images indicated heavy cloud cover, suggesting that rainfall during that period could have triggered the drainages by adding extra water to the basins and changing the surface hydrology and morphology. It is also possible that those lakes have some hydrological connections. For example, they might share the same configuration of subglacial drainage systems determined by the amount of melt water available. In particular, the two lakes near Petermann Glacier and Humboldt Glacier might be connected through a supraglacial overspilling water flow. The higher supraglacial lake (∼860m high) drained its water first. The water could then flow along the northern canyons to the nearby, lower, ice-dammed lake (∼230m high) beside Petermann Glacier, thereby triggering its drainage. Additional observations are needed to substantiate this hypothesis.

4.4.6 Lake depths estimation

Previous researchers have used satellite images to retrieve lake depths, based on the principle that lake water surface reflectance depends on water depth (Sneed and Hamilton, 2007; Box and Ski, 2007). Unlike the estimates we have obtained here with ICESat, these retrievals have high uncertainties, as we will describe later. Satellite images can, however, provide better spatial and temporal coverage than ICESat, and thus are suitable for studying numerous melt ponds, e.g. in the ablation zone of western Greenland, and the high-frequency temporal evolution of lakes (Luthje et al., 2006; Sneed and Hamilton, 2007; Box and Ski, 2007; McMillan et al., 2007; Sundal et al., 2009; Georgiou et al., 2009; Selmes et al., 2011). These images may also be more useful for studying lakes with small amplitude changes in lake levels, since we used a 2 m criterion for the elevation change to be significant.

The main problem with imagery is that most Greenland surface lakes detected by ICESat are ice-covered at relatively high elevation close to the equilibrium line. Water depths of these ice-covered lakes cannot be retrieved from the satellite imagery, which applies only to totally ice-free lakes that are usually shallow and active at very low elevation, e.g. in western Greenland (Laura Cordero Llana, personal communication). The water volume contained in the ice-covered lakes ($\sim 10^7 m^3$ per lake) may, however, account for an important part of the total amount of melt water contained in all surface lakes on the Greenland ice sheet. This is because those ice-covered lakes are usually very deep and do not drain every year, but have a potentially large impact during a drainage event.

Another problem with imagery is that it applies to only a certain range of depths, even when the surface lakes are ice free. If the lakes are too deep, the depth retrieving method does not work because there is an upper limit of water depth beyond which reflectance does not decrease significantly with depth (Morassutti and LeDrew, 1996; Box and Ski, 2007). Optically deep water with depth more than $\sim$ 40m has almost constant surface reflectance (Sneed and Hamilton, 2007). If the lakes are too shallow, the radiative transfer model does not work well, e.g. for depths less than 2 m, the uncertainty is $\sim$0.9 m (Georgiou et al., 2009). Also, the empirical relationship between surface reflectance and water depth derives from

limited field measurements in a specific area (Box and Ski, 2007), which may not apply to other regions and cannot be generalized for all supraglacial lakes on the Greenland Ice Sheet. In contrast, ICESat is able to more accurately estimate the depths of very deep surface lakes, which reached a maximum along-track depth of 55 m.

ICESat laser altimetry and satellite imagery both provide useful information about the depths of different types of supraglacial lakes. ICESat detects lakes that are mostly ice covered, deeper, and further inland. Satellite imagery detects lakes that are totally ice free, shallower, and closer to the ice margin. ICESat laser altimeter measures the lake depths directly, giving reliable volume estimates for individual lakes at limited times. Satellite images provide comprehensive results because of good spatial and temporal coverage of lakes in certain regions. Therefore, we suggest that a combination of these two methods can provide constraints for the total volume of melt water contained in the supraglacial lakes on the Greenland ice sheet.

4.5 Conclusions

We have studied surface lakes in Greenland using repeat-track ICESat laser altimeter data. ICESat can detect the depths of both supraglacial lakes and ice-dammed lakes with large surface elevation changes due to the draining and filling of the lakes. We have identified 32 active lakes with large elevation changes ($> 2m$). The along-track lake depth can be as large as 55 m, and median along-track depth is 11 m. The spatial distribution of the lakes detected by ICESat concentrates along the coasts of northeastern, western, and northwestern Greenland. The lakes at higher latitudes usually sit at lower elevation. Time series of surface elevation show cycles of draining and filling of the lakes, and these lakes are not observed to drain in each year.

We have also developed a method of constructing the three dimensional geometry of supraglacial lake basins and estimating the lake water volume, by combining elevation measurements of the lake basin from multiple campaigns with

cross-track separation of a few hundred meters. We assume that the shape of the supraglacial lake basin is rotationally symmetric with a vertical axis and time-invariant. Through validation with LVIS high-resolution airborne laser altimetry, the modeled geometry of the lake basin from ICESat data is adequate, and the model assumptions are reasonable.

The volume of water contained in the supraglacial lakes is typically $3 \times 10^7 m^3$, and the volume of water drained from the ice-dammed lake beside Petermann Glacier is $66 - 90 \times 10^7 m^3$. Compared to the estimated Greenland ice-sheet mass loss, which is $232 km^3 year^{-1}$ water-equivalent over the period October 2003-December 2008 (Shepherd et al., 2012), these lake drainage events are small. However, the water drained from these surface lakes could induce ice velocity changes near the margins of the Greenland Ice Sheet. Drainage of these surface lakes could be important in the Greenland Ice Sheet's mass balance and its contribution to sea level rise.

Acknowledgments

I greatly thank Helen Fricker for providing wise advice on the work in Chapter 4. I really appreciate Helen Fricker for providing fundings for a few years. I am very grateful to Jennifer Bohlander, Ted Scambos, Bruce Raup, Ian Joughin and Marco Tedesco for providing satellite images. I also thank Michelle Hofton and Bryan Blair for introducing LVIS data and helpful discussion.

References

Abdalati, W. and Steffen, K. Greenland ice sheet melt extent: 1979-1999. *Journal of Geophysical Research-Atmospheres*, 106(D24):33983–33988, 2001.

Bartholomew, I.; Nienow, P.; Mair, D.; Hubbard, A.; King, M. A., and Sole, A. Seasonal evolution of subglacial drainage and acceleration in a greenland outlet glacier. *Nature Geoscience*, 3(6):408–411, 2010.

Bhattacharya, I.; Jezek, K. C.; Wang, L., and Liu, H. X. Surface melt area variability of the greenland ice sheet: 1979-2008. *Geophysical Research Letters*, 36, 2009.

Box, J. E. and Ski, K. Remote sounding of greenland supraglacial melt lakes: implications for subglacial hydraulics. *Journal of Glaciology*, 53(181):257–265, 2007.

Box, J. E.; Bromwich, D. H.; Veenhuis, B. A.; Bai, L. S.; Stroeve, J. C.; Rogers, J. C.; Steffen, K.; Haran, T., and Wang, S. H. Greenland ice sheet surface mass balance variability (1988-2004) from calibrated polar mm5 output. *Journal of Climate*, 19(12):2783–2800, 2006.

Colgan, W.; Steffen, K.; McLamb, W. S.; Abdalati, W.; Rajaram, H.; Motyka, R.; Phillips, T., and Anderson, R. An increase in crevasse extent, west greenland: Hydrologic implications. *Geophysical Research Letters*, 38, 2011.

Das, S. B.; Joughin, I.; Behn, M. D.; Howat, I. M.; King, M. A.; Lizarralde, D., and Bhatia, M. P. Fracture propagation to the base of the greenland ice sheet during supraglacial lake drainage. *Science*, 320(5877):778–781, 2008.

Echelmeyer, K; Clarke, TS, and Harrison, WD. Surficial glaciology of jakobshavns isbræ, west greenland: Part i. surface morphology. *J. Glaciol*, 37(127):368–382, 1991.

Fettweis, X.; Tedesco, M.; van den Broeke, M., and Ettema, J. Melting trends over the greenland ice sheet (1958-2009) from spaceborne microwave data and regional climate models. *Cryosphere*, 5(2):359–375, 2011.

Georgiou, S.; Shepherd, A.; McMillan, M., and Nienow, P. Seasonal evolution of supraglacial lake volume from aster imagery. *Annals of Glaciology*, 50(52): 95–100, 2009.

Hanna, E.; Huybrechts, P.; Janssens, I.; Cappelen, J.; Steffen, K., and Stephens, A. Runoff and mass balance of the greenland ice sheet: 1958-2003. *Journal of Geophysical Research-Atmospheres*, 110(D13), 2005.

Hoffman, MJ; Catania, GA; Neumann, TA; Andrews, LC, and Rumrill, JA. Links between acceleration, melting, and supraglacial lake drainage of the western greenland ice sheet. *Journal of Geophysical Research: Earth Surface (2003–2012)*, 116(F4), 2011.

Huss, Matthias; Bauder, Andreas; Werder, Mauro; Funk, Martin, and Hock, Regine. Glacier-dammed lake outburst events of gornersee, switzerland. *Journal of Glaciology*, 53(181):189–200, 2007.

Jezek, Kenneth C; Gogineni, Prasad, and Shanableh, M. Radar measurements of melt zones on the greenland ice sheet. *Geophysical Research Letters*, 21(1): 33–36, 1994.

Joughin, I.; Das, S. B.; King, M. A.; Smith, B. E.; Howat, I. M., and Moon, T. Seasonal speedup along the western flank of the greenland ice sheet. *Science*, 320(5877):781–783, 2008.

Krawczynski, M. J.; Behn, M. D.; Das, S. B., and Joughin, I. Constraints on the lake volume required for hydro-fracture through ice sheets. *Geophysical Research Letters*, 36, 2009.

Lampkin, DJ. Supraglacial lake spatial structure in western greenland during the 2007 ablation season. *Journal of Geophysical Research*, 116(F4):F04001, 2011.

Luthje, M.; Pedersen, L. T.; Reeh, N., and Greuell, W. Modelling the evolution of supraglacial lakes on the west greenland ice-sheet margin. *Journal of Glaciology*, 52(179):608–618, 2006.

McMillan, M.; Nienow, P.; Shepherd, A.; Benham, T., and Sole, A. Seasonal evolution of supra-glacial lakes on the greenland ice sheet. *Earth and Planetary Science Letters*, 262(3-4):484–492, 2007.

Mernild, S. H.; Mote, T. L., and Liston, G. E. Greenland ice sheet surface melt extent and trends: 1960-2010. *Journal of Glaciology*, 57(204):621–628, 2011.

Morassutti, MP and LeDrew, EF. Albedo and depth of melt ponds on sea-ice. *International journal of climatology*, 16(7):817–838, 1996.

Mote, T. L. Greenland surface melt trends 1973-2007: Evidence of a large increase in 2007. *Geophysical Research Letters*, 34(22):5, 2007.

Raymond, Charles F and Nolan, MATT. Drainage of a glacial lake through an ice spillway. *IAHS PUBLICATION*, pages 199–210, 2000.

Rignot, E and Steffen, K. Channelized bottom melting and stability of floating ice shelves. *Geophysical Research Letters*, 35(2):L02503, 2008.

Russell, Andrew J; Aitken, John F, and de Jong, Carmen. Observations on the drainage of an ice-dammed lake in west greenland. *J. Glaciol*, 36(122):72–74, 1990.

Schoof, C. Ice-sheet acceleration driven by melt supply variability. *Nature*, 468 (7325):803–806, 2010.

Selmes, N.; Murray, T., and James, T. D. Fast draining lakes on the greenland ice sheet. *Geophysical Research Letters*, 38, 2011.

Shepherd, A.; Hubbard, A.; Nienow, P.; King, M.; McMillan, M., and Joughin, I. Greenland ice sheet motion coupled with daily melting in late summer. *Geophysical Research Letters*, 36, 2009.

Shepherd, Andrew; Ivins, Erik R; Geruo, A; Barletta, Valentina R; Bentley, Mike J; Bettadpur, Srinivas; Briggs, Kate H; Bromwich, David H; Forsberg, René; Galin, Natalia, and others, . A reconciled estimate of ice-sheet mass balance. *Science*, 338(6111):1183–1189, 2012.

Sneed, W. A. and Hamilton, G. S. Evolution of melt pond volume on the surface of the greenland ice sheet. *Geophysical Research Letters*, 34(3), 2007.

Sole, Andrew John; Mair, Douglas Watson Fraser; Nienow, Peter W; Bartholomew, ID; King, MA; Burke, Matt J, and Joughin, Ian. Seasonal speedup of a greenland marine-terminating outlet glacier forced by surface melt–induced changes in subglacial hydrology. *Journal of Geophysical Research: Earth Surface (2003–2012)*, 116(F3), 2011.

Sundal, A. V.; Shepherd, A.; Nienow, P.; Hanna, E.; Palmer, S., and Huybrechts, P. Evolution of supra-glacial lakes across the greenland ice sheet. *Remote Sensing of Environment*, 113(10):2164–2171, 2009.

Sundal, Aud Venke; Shepherd, Andrew; Nienow, Peter; Hanna, Edward; Palmer, Steven, and Huybrechts, Philippe. Melt-induced speed-up of greenland ice sheet offset by efficient subglacial drainage. *Nature*, 469(7331):521–524, 2011.

Walder, JS. others. 2005. fault-dominated deformation in an ice dam during annual filling and drainage of a marginal lake. *Ann. Glaciol*, 40:174–178, 2005.

Zwally, H. J.; Abdalati, W.; Herring, T.; Larson, K.; Saba, J., and Steffen, K. Surface melt-induced acceleration of greenland ice-sheet flow. *Science*, 297(5579): 218–222, 2002.

Table 4.1: ICESat campaigns for the 3 laser altimeters and their corresponding operational periods

Campaign	Period
Laser 1	20 Feb 2003 - 29 Mar 2003
Laser 2a	25 Sep 2003 - 19 Nov 2003
Laser 2b	17 Feb 2004 - 21 Mar 2004
Laser 2c	18 May 2004 - 21 Jun 2004
Laser 3a	03 Oct 2004 - 08 Nov 2004
Laser 3b	17 Feb 2005 - 24 Mar 2005
Laser 3c	20 May 2005 - 23 Jun 2005
Laser 3d	21 Oct 2005 - 24 Nov 2005
Laser 3e	22 Feb 2006 - 28 Mar 2006
Laser 3f	24 May 2006 - 26 Jun 2006
Laser 3g	25 Oct 2006 - 27 Nov 2006
Laser 3h	12 Mar 2007 - 14 Apr 2007
Laser 3i	02 Oct 2007 - 05 Nov 2007
Laser 3j	17 Feb 2008 - 21 Mar 2008
Laser 3k	04 Oct 2008 - 19 Oct 2008
Laser 2d	25 Nov 2008 - 17 Dec 2008
Laser 2e	09 Mar 2009 - 11 Apr 2009

Table 4.2: Fitted model parameters for the geometries of the supraglacial lake basin near Ryder Glacier in northern Greenland and the supraglacial lake basin in western Greenland

Gaussian model parameters	Lake in the north from ICESat data	Lake in the west from ICESat data	Lake in the west from LVIS data
x_0 (km)	-80.74	-123.79	-123.68
y_0 (km)	-973.25	-2436.00	-2436.00
z_0 (m)	911.45	1600.80	1601.10
D_0 (m)	62.06	18.91	20.33
σ (km)	0.42	0.79	0.83

Table 4.3: Maximum depth, area, and volume estimates at different times of the supraglacial lake near Ryder Glacier in northern Greenland

Time	Max Depth (m)	Area (m^2)	Volume (m^3)
L2b 13Mar04	48.53	1.76×10^6	3.227×10^7
L2c 12Jun04	47.40	1.66×10^6	3.033×10^7
L3c 14Jun05	47.83	1.70×10^6	3.107×10^7
L3d 15Nov05	0	0	0
L3e 19Mar06	0	0	0
L3f 18Jun06	0	0	0
L3i 27Oct07	45.95	1.57×10^6	2.800×10^7
L3j 13Mar08	44.10	1.43×10^6	2.524×10^7
L2d 09Dec08	0	0	0

Table 4.4: Volume, area, and maximum depth estimates in different campaigns from constructed geometry of a lake basin in western Greenland based on ICESat data and LVIS data separately

Campaign	Volume from ICESat Model (m^3)	Volume from LVIS Model (m^3)	Area from ICESat Model (m^2)	Area from LVIS Model (m^2)	Max Depth from ICESat Model (m)	Max Depth from LVIS Model (m)
L2a	2.297×10^7	2.863×10^7	4.46×10^6	5.08×10^6	12.67	13.86
L2b	2.508×10^7	3.104×10^7	4.73×10^6	5.39×10^6	13.13	14.32
L2c	2.337×10^7	2.098×10^7	4.50×10^6	5.13×10^6	12.76	13.95
L3g	2.729×10^7	3.356×10^7	5.02×10^6	5.75×10^6	13.58	14.77
L3h	2.743×10^7	3.372×10^7	5.07×10^6	5.78×10^6	13.61	14.80
L2e	6.182×10^6	8.833×10^6	1.90×10^6	2.32×10^6	7.12	8.31

Table 4.5: Lake areas in different campaigns from constructed geometry of a lake basin in western Greenland based on ICESat data and from MODIS satellite images

Campaighn	Area from model (km^2)	Area from image (km^2)
L2b	1.76	1.90
L2c	1.67	2.39
L3c	1.70	2.84
L3i	1.56	3.53
L3j	1.42	2.44

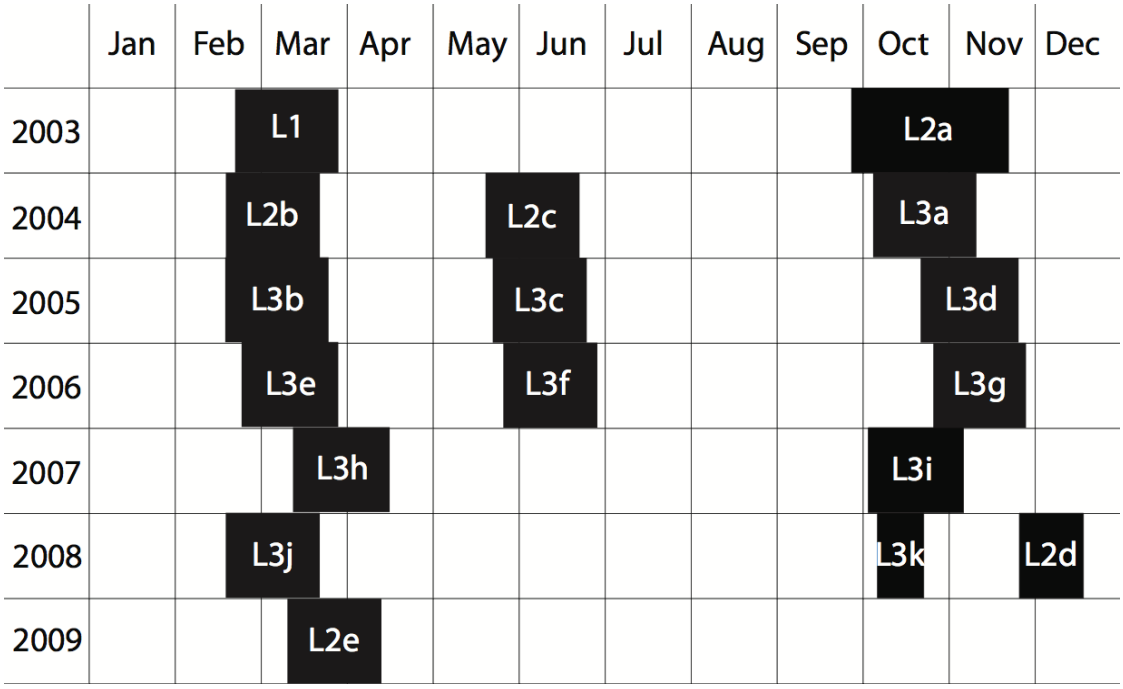

Figure 4.1: Operational time periods of the ICESat campaigns. There are 3 laser altimeters, represented as L1, L2 and L3.

Figure 4.2:(a) Surface elevation profiles of a supraglacial lake in western Greenland (67.735 ° N,-48.05 ° E) at different times represented by different colors from repeated ICESat laser altimeter measurements. (b) Time series of surface elevations of this supraglacial lake. (c) Surface elevation profiles of an ice-dammed lake adjacent to Petermann Glacier in northern Greenland (80.25 ° N, -60.20 ° E) at different times represented by different colors from repeated ICESat laser altimeter measurements. (d) Time series of surface elevations of this ice-dammed lake. (e) Spatial distribution of surface lakes in Greenland detected by ICESat. Red pluses represent locations of lakes. The background is MODIS Mosaic of Greenland overlaid with ICESat tracks color-coded with WGS-84 elevation. Orange rectangles represent locations of two typical surface lakes. The MODIS satellite image of the supraglacial lake in the west and the ASTER satellite image of the ice-dammed lake in the north are also shown.

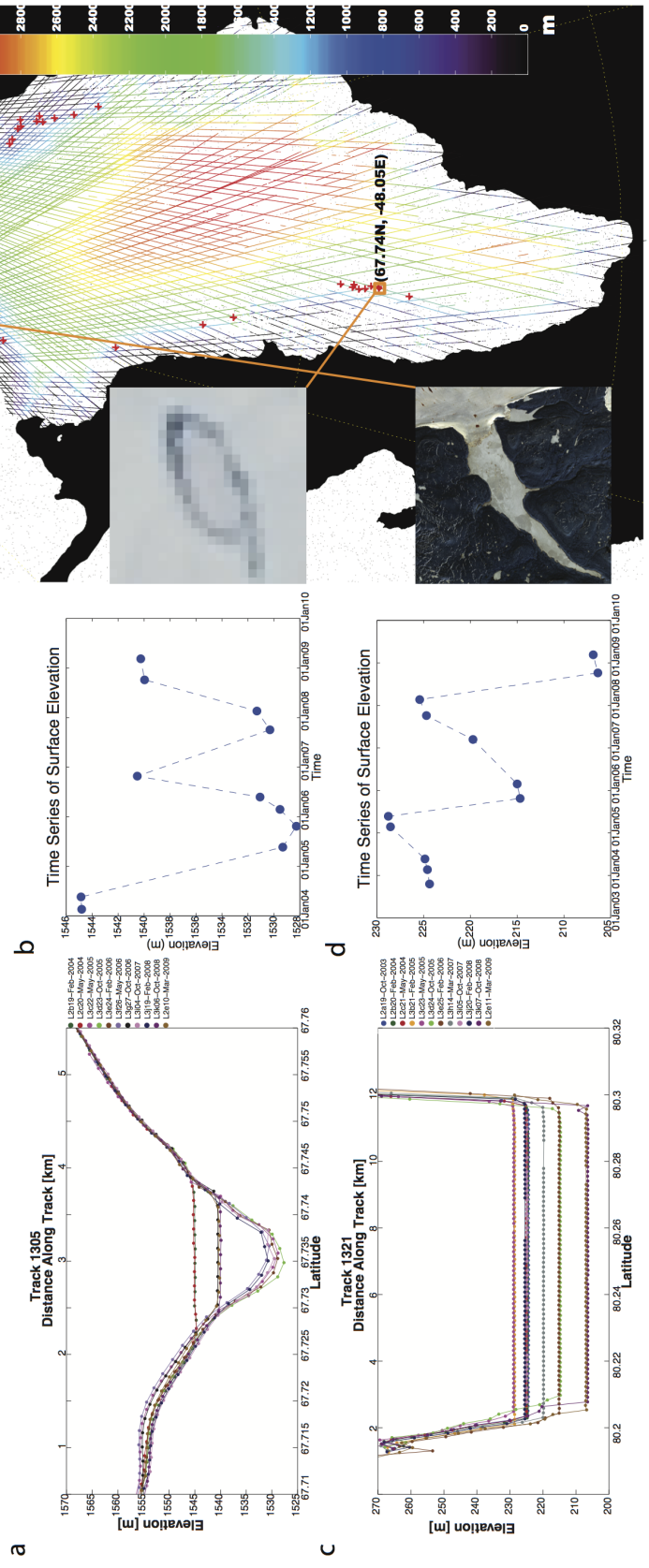
a
Track 1305
Distance Along Track [km]
Elevation [m]
Latitude
b
Time Series of Surface Elevation
Elevation (m)
Time
c
Track 1321
Distance Along Track [km]
Elevation [m]
Latitude
d
Time Series of Surface Elevation
Elevation (m)
Time
e
(80.25N, -60.20E)
(67.74N, -48.05E)
m

Figure 4.2

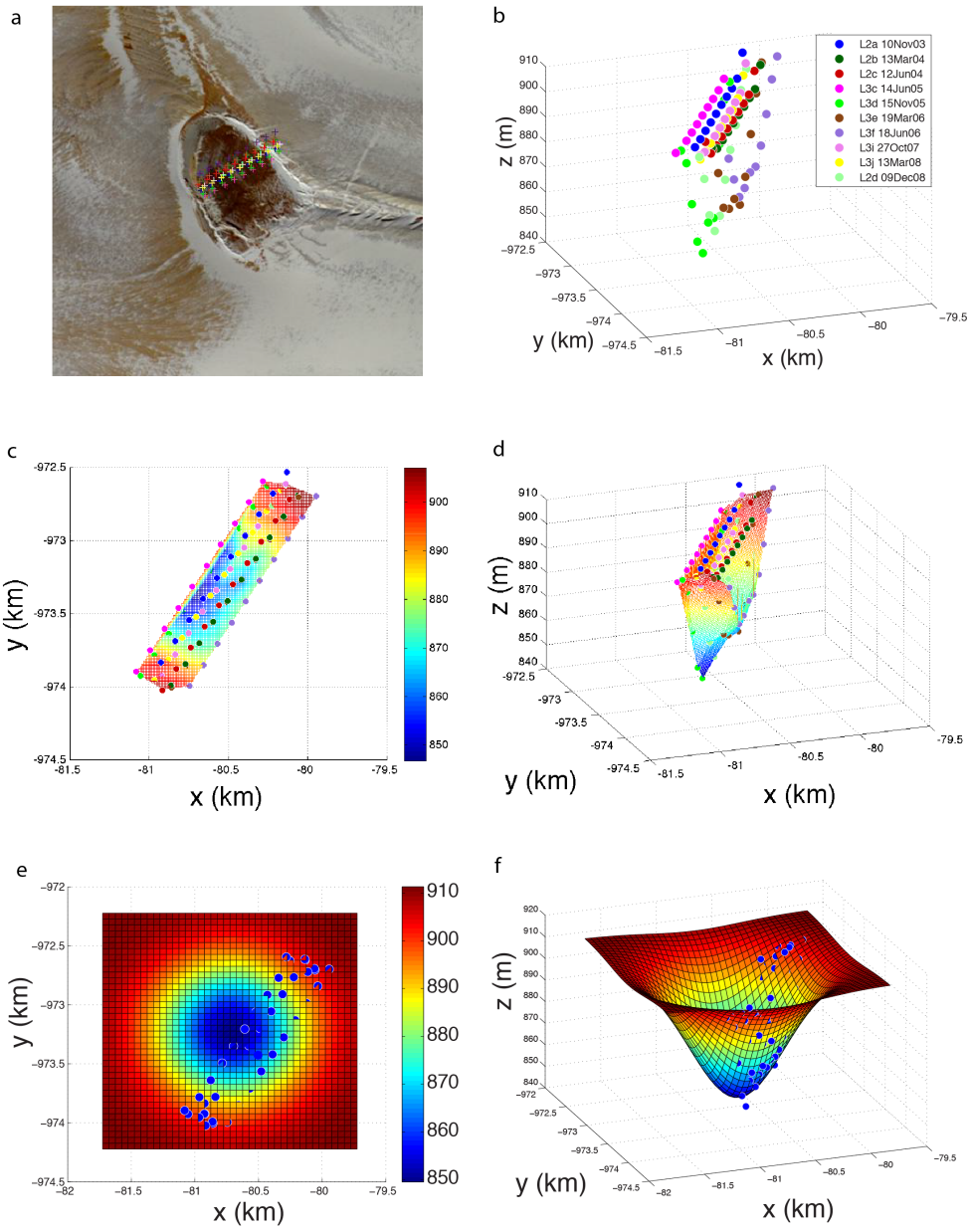

Figure 4.3: (a) ICESat tracks on the ASTER satellite image of one supraglacial lake near Ryder Glacier in northern Greenland (81.00 ° N, -49.74 ° E). The location of this lake is marked on the MODIS Mosaic of Greenland. (b) ICESat measurements of the lake from different campaigns in different colors. (c) (d) Interpolated surface from ICESat measurements of the lake basin. The dots are ICESat measurements from different campaigns. (e) (f) Constructed 3D geometry of the lake basin from ICESat data. The shape is Gaussian. The dots are ICESat measurements of the lake basin.

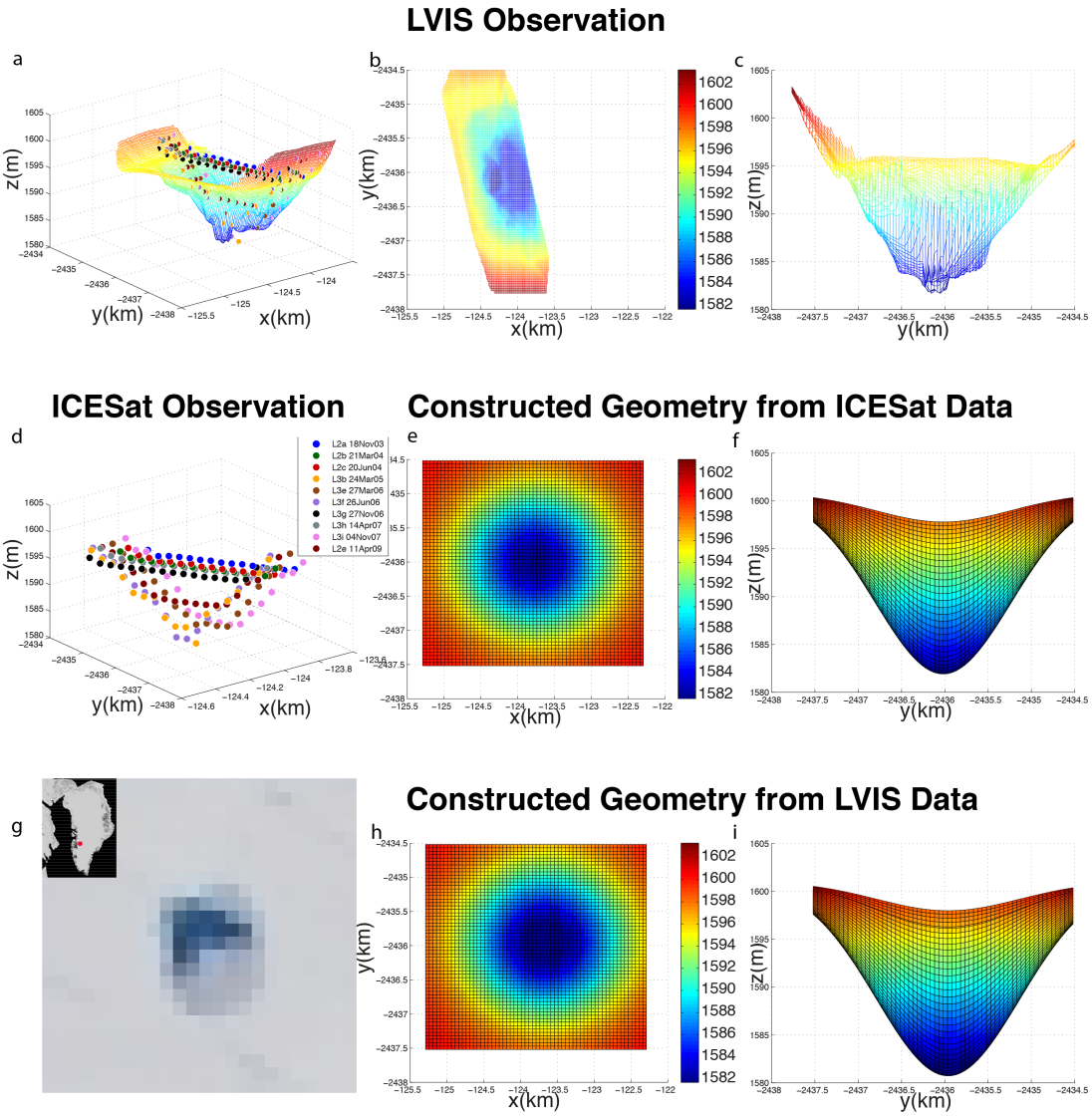

Figure 4.4: (a) (b) (c) Digital Elevation Model derived from LVIS measurements of one supraglacial lake in western Greenland (67.76 ° N, -47.92 ° E). The dots are ICESat measurements from different campaigns. (d) ICESat measurements of this lake from different campaigns in different colors. (e) (f) Constructed geometry of the lake basin from ICESat data. (h) (i) Constructed geometry of the lake basin from LVIS data. (g) MODIS satellite image of this lake, with part of the lake obscured by ice cover. The location of this lake is marked on the MODIS Mosaic of Greenland.

Chapter 5

Conclusion

5.1 Summary

Sea ice in the Bering Sea exhibits large seasonal and interannual variations, which significantly impact the local marine ecosystem and regional oceanography. To better understand the processes that control this regional sea-ice variability, we utilize a fine resolution (1/10-degree) global ocean and sea-ice model along with available observations. The simulation consists of the Los Alamos National Laboratory Parallel Ocean Program (POP) and the Los Alamos Sea Ice (CICE) models, and was run with Coordinated Ocean-ice Reference Experiment (CORE2) interannually varying atmospheric forcing for 1970-1989. Here 1980-1989 are analyzed; the first 10 years are treated as the spin-up period.

In order to identify the relationships between sea ice variability and varying atmospheric and oceanic conditions, we examine the partitioning of the ice volume tendencies into thermodynamic and dynamic components, as well as corresponding surface atmospheric and oceanic variables.

First the seasonal cycle of sea ice in the Bering Sea and environmental conditions are studied. In winter, sea ice is mainly formed in the northern Bering Sea with the maximum ice growth rate occurring along the coast. Winds drive sea ice to drift southwestward from the north to the southwestern ice edge. Along the ice edge especially in the western Bering, ice is melted by warm waters carried by the Bering Slope Current. This leads to the characteristic S-shaped pattern along

the southern ice edge. In spring and fall, similar dynamics and thermodynamics occur, but with smaller magnitudes and with season-specific geographical and directional differences. In summer, the Bering Sea is observed to be ice free, while the model has small amounts of residual ice. Surface melting is insignificant in all seasons. Furthermore, the driving forcings of seasonal cycle of sea ice in the Bering Sea, including heat budget and force balance for sea ice, are examined. Seasonal thermodynamic ice volume change is dominated by surface heat flux between the atmosphere and the ice in the north, and by heat flux from the ocean to the ice along the southern ice edge especially on the western side. Sea ice motion is largely associated with wind stress. Internal ice stress is large near the land boundaries in the north, and is small in the central and southern ice-covered area.

Next the year-to-year variability of sea ice in the Bering Sea and its forcing mechanisms are addressed. The sea ice variability in the Bering Sea can be largely explained by thermodynamic processes on the large scale, while dynamic effects are often important locally, especially near the ice margins with ocean and with land. Local dynamic and thermodynamic ice volume changes usually have opposite signs with similar and large magnitudes but with a slightly larger dynamic term, and the net ice volume change is usually dominated by dynamics locally near the ice margins. The anomalies of thermodynamic and dynamic tendencies can occasionally have the same sign to produce extreme anomalous events, for instance in February 1989 and in February 1984. The ice heat budget reveals that sensible heat flux dominates surface heat flux between the ice and the atmosphere, which controls the winter ice growth on the large scale, especially in the north. Consequently, the surface air temperature, which is specified from observations as a dominant part of the surface heat-flux forcing, strongly controls the ice volume tendency. Ocean-ice heat flux largely determines the ice basal melting along the ice edge in the south. The ice force balance indicates that monthly mean ice motion is nearly in phase with wind stress, especially in the meridional direction. Ocean stress can be important in driving ice motion near some straits in the north. Wind stress and ocean stress are opposite in direction, and similar and large in magnitude, and wind stress is slightly stronger in general. Internal ice stress is large near the

land boundaries in the north, and is small in the central and southern ice-covered area. The stress due to Coriolis effects and the stress due to sea surface slope are generally small.

Additionally, the draining and filling of Greenland surface lakes (including supraglacial lakes and ice-dammed lakes) are studied, based on repeat-track ICESat (Ice, Cloud, and land Elevation Satellite) laser altimeter data. 32 active lakes with large elevation change ($> 2m$) are identified. The along-track lake depth can be as large as 55 m, and median along-track depth is 11 m. The spatial distribution of the lakes detected by ICESat concentrates along the coasts of northeastern, western, and northwestern Greenland. The three dimensional geometry of supraglacial lake basins has been constructed from ICESat data, and validated with LVIS (Laser Vegetation Imaging Sensor) high-resolution airborne laser altimetry. Finally, the volume of water contained in the lakes and involved in the lake drainage events is estimated. The volume of water contained in the supraglacial lakes is typically $3 \times 10^7 m^3$, and the volume of water drained from the ice-dammed lake beside Petermann Glacier is $66 - 90 \times 10^7 m^3$. Compared to the published estimated Greenland ice-sheet mass loss, which is $232 km^3 year^{-1}$ water-equivalent over the period October 2003- December 2008, these lake drainage events are small. However, the water drained from these surface lakes could induce ice velocity changes near the margins of the Greenland Ice Sheet. Drainage of these surface lakes could be important in the Greenland Ice Sheet mass balance and its contribution to sea level rise.

5.2 Future work

Although significant progress has been made in understanding the physical mechanisms governing this sea-ice variability, several issues merit further attention. One approach is to investigate the co-variability of spatial patterns of sea ice and atmosphere/ocean conditions in the Bering Sea through the Empirical Orthogonal Functions (EOF) analysis. This will yield characteristic space-time patterns of variability of sea ice volume tendencies due to thermodynamic and dynamic pro-

cesses. These can then be related to large-scale climate events and to coherencies among regional oceanic and ecological processes in the Bering Sea.

The effects of mesoscale eddies on the Bering sea ice variability need to be addressed. An especially important issue is how eddy activity around the Bering Slope Current influences the ice basal melting and the dispersal of ice along the ice edge. One way to study this is to compare the high-resolution version (0.1 degree) simulation with a similarly forced low-resolution version (1 degree) of the model to identify whether the small-scale structures of ocean and ice alter the dynamical and thermodynamical properties of the system. This will require archiving daily, or at least weekly, fields of ocean and ice variables, which are not currently available.

Another important issue is that the specified surface atmospheric variables exert strong controls on the ice evolution in this model run. A careful study of the impact of full coupling on the atmosphere-sea-ice-ocean system needs to be executed and diagnosed like the current uncoupled model run. By comparing results between these simulations, the three-way interaction between sea ice, the atmosphere, and the ocean, in the presence of internal variability of the climate system, can be better understood.

Finally, the sea ice balances in the Bering Sea needs to be studied over a longer time period to determine whether the sea ice properties identified here for 1980-1989 are truly characteristic or whether other persistent patterns and balances arise during different time periods. Longer runs of the model, which were not available at the outset of this study, will also allow quantifying the decadal variability and trends of sea ice in the Bering Sea. These can be compared with model runs forced with future climate scenarios associated with global warming to project how sea ice conditions and their physical controls may be altered by a changing background climate state.

Appendix A

Ice thermodynamic and dynamic equations in the CICE model

This summarizes the important ice thermodynamic and dynamic equations utilized by the CICE model, based on *CICE: the Los Alamos Sea Ice Model Documentation and Software Users Manual Version 4.1* (Hunke and Lipscomb, 2010). Here we only show the continuous forms of the equations.

Governing Equations

CICE uses a subgridscale ice thickness distribution with five ice thickness categories: $0.00m \sim 0.60m, 0.60m \sim 1.40m, 1.40m \sim 2.40m, 2.40m \sim 3.60m, > 3.60m$. g is the ice thickness distribution, and gdh is the fractional ice area covered by ice with thickness h to $h + dh$.

The governing equations for evolution of ice concentration and ice volume per unit area for each ice thickness category are

$$\frac{\partial g_i}{\partial t} = -\nabla \cdot (\mathbf{u} g_i) + \Psi_i + \zeta_i \tag{A.1}$$

$$\frac{\partial V_i}{\partial t} = -\nabla \cdot (\mathbf{u} V_i) + \Theta_i + \nu_i \tag{A.2}$$

where g_i is ice thickness distribution for each category, V_i is ice volume per unit

area for each category, $\mathbf{u}$ is ice velocity, Ψ_i and Θ_i are contributions of mechanical redistribution, and ζ_i and ν_i are thermodynamic contributions.

Ice volume per unit area aggregated over the subgridscale ice thickness distribution is governed by

$$\frac{\partial V}{\partial t} = -\nabla \cdot (\mathbf{u}V) + \nu \tag{A.3}$$

where V is ice volume per unit grid cell area, $\mathbf{u}$ is ice velocity, and ν is the thermodynamic contribution to ice volume tendency summed over ice categories.

Ice Thermodynamics

CICE uses an energy-conserving thermodynamic sea ice model by Bitz and Lipscomb (1999). CICE has one snow layer and four ice layers with equal thickness.

The ice temperature in the ice interior is governed by the thermal diffusion equation in the vertical direction:

$$\rho_i c_i \frac{\partial T_i}{\partial t} = \frac{\partial}{\partial z}(K_i \frac{\partial T_i}{\partial z}) - \frac{\partial}{\partial z}[I_{pen}(z)] \tag{A.4}$$

where ρ_i is the sea ice density, $c_i(T, S)$ is the specific heat of sea ice, $K_i(T, S)$ is the thermal conductivity of sea ice, and I_{pen} is the penetrating solar radiation at depth z. The vertical coordinate z is defined to be positive downward with $z = 0$ at the top surface.

The vertical salinity profile is specified as follows, based on empirical relationships. The ice salinity at the midpoint in each ice layer

$$S_{ik} = \frac{1}{2} S_{max}[1 - cos(\pi z^{(\frac{a}{z+b})})] \tag{A.5}$$

where $z \equiv (k - 1/2)/N_i$, $S_{max} = 3.2psu$, and a and b are empirical constants. This salinity profile varies from $S = 0$ at the surface to $S = S_{max}$ at the bottom.

The specific heat of sea ice is

$$c_i(T, S) = c_0 + \frac{L_0 \mu S}{T^2} \tag{A.6}$$

where $c_0 = 2106 J/kg/deg$ is the specific heat of fresh ice at 0 ° C, $L_0 = 3.34 \times 10^5 J/kg$ is the latent heat of fusion of fresh ice at 0 ° C, and $\mu = 0.054 deg/psu$ is the ratio between the freezing temperature and salinity of brine.

The thermal conductivity of sea ice is

$$K_i(T, S) = K_0 + \frac{\beta S}{T} \tag{A.7}$$

where $K_0 = 2.03 W/m/deg$ is the thermal conductivity of fresh ice, and β is a constant.

Sea ice enthalpy is defined as

$$q_i(T, S) = -\rho_i[c_0(T_m - T) + L_0(1 - \frac{T_m}{T}) - c_w T_m] \tag{A.8}$$

Melting at the top surface is determined by

$$q\delta h = \begin{cases} (F_0 - F_{ct})\Delta t & \text{if } F_0 > F_{ct} \\ 0 & \text{otherwise} \end{cases}$$

where q is the enthalpy of the surface ice or snow layer, δh is thickness change. F_0 is the surface heat flux, F_{ct} is the conductive heat flux at the top surface.

Growth and melting at the bottom ice surface is determined by

$q\delta h = (F_{cb} - F_{bot})\Delta t$, where q is the ice enthalpy, δh is thickness change. F_{bot} is the ocean-ice heat flux, F_{cb} is the conductive heat flux at the bottom surface.

The energy flux from the atmosphere to the ice is

$$F_0 = F_s + F_l + F_{L\downarrow} + F_{L\uparrow} + (1 - \alpha)(1 - i_0)F_{sw} \tag{A.9}$$

where F_s is the sensible heat flux, F_l is the latent heat flux, $F_{L\downarrow}$ is the incoming longwave flux, $F_{L\uparrow}$ is the outgoing longwave flux, F_{sw} is the incoming shortwave flux, α is the shortwave albedo, and i_0 is the fraction of absorbed shortwave flux penetrating into the ice (and possibly through the ice into the ocean). Fluxes are defined as positive downward.

Incoming shortwave radiation and incoming longwave radiation are specified in the atmospheric forcing. This model uses the Delta-Eddington multiple

scattering radiative transfer scheme for shortwave radiation and albedo. Outgoing longwave radiation is blackbody radiation

$$F_{L\uparrow} = \varepsilon\sigma(T_{sf}^K)^4 \tag{A.10}$$

where $\varepsilon = 0.95$ is the emissivity of snow or ice, σ is the Stefan-Boltzmann constant and T_{sf}^K is the surface temperature in Kelvin provided by the model.

Sensible heat flux F_s is proportional to the difference between air potential temperature Θ_a specified in the atmospheric forcing and surface temperature T_{sf}^K calculated by the model

$$F_s = C_s(\Theta_a - T_{sf}^K) \tag{A.11}$$

Latent heat flux F_l is proportional to the difference between air specific humidity Q_a from the atmospheric forcing and surface saturation specific humidity Q_{sf}

$$F_l = C_l(Q_a - Q_{sf}) \tag{A.12}$$

$$Q_{sf} = (q_1/\rho_a)exp(-q_2/T_{sf}^K) \tag{A.13}$$

C_s and C_l are turbulent heat transfer coefficients determined by

$$C_l = \rho_a(L_{vap} + L_{ice})u^* c_q \tag{A.14}$$

$$C_s = \rho_a c_p u^* c_\theta + 1 \tag{A.15}$$

where L_{vap} and L_{ice} are latent heats of vaporization and fusion, ρ_a is surface air density and c_p is specific heat. u^* is the turbulent scale for velocity

$$u^* = c_u|\overrightarrow{U_a}| \tag{A.16}$$

where c_u is the exchange coefficient, and $\overrightarrow{U_a}$ is the wind velocity from the atmospheric forcing.

The heat flux from the ice to the ocean is

$$F_{bot} = -\rho_w c_w c_h u_* (T_w - T_f) \tag{A.17}$$

where ρ_w is the density of seawater, c_w is the specific heat of seawater, c_h is the heat transfer coefficient, $u_* = \sqrt{|\overrightarrow{\tau_w}|/\rho_w}$ is the friction velocity, T_f is the freezing temperature of ocean mixed layer, and T_w is sea surface temperature calculated by the model.

This model run is forced with Coordinated Ocean-ice Reference Experiment version 2 (CORE2) interannually varying atmospheric forcing from 1970-1989 (Large and Yeager, 2009). CORE 2 includes 6-hourly (1948-2006) surface wind velocity, specific humidity and air temperature based on NCEP reanalysis, daily radiation (1984-2006) and monthly precipitation (1979-2006) from satellite observations. Climatological mean annual cycles are used for radiation (1948-1983) and precipitation (1948-1978) before satellite observational periods. Some data sets are adjusted to satellite and in situ observations in the mean. For example, NCEP winds are adjusted to QuikSCAT satellite scatterometer winds (2000-2004): wind speed is increased almost everywhere, but wind direction is not corrected. Fluxes of heat, momentum and fresh-water at the surface are calculated interactively with the model variables of SST, ice/snow surface temperature, and ice surface roughness. CORE2 is on T62 grid with a horizontal resolution of $\sim 100km$ (east-west) and $\sim 200km$ (north-south) in the Bering Sea.

Ice Dynamics

The ice momentum equation is

$$m\frac{\partial \mathbf{u}}{\partial t} = \nabla \cdot \sigma + \overrightarrow{\tau_a} + \overrightarrow{\tau_w} - \hat{k} \times mf\mathbf{u} - mg\nabla H_0 \tag{A.18}$$

where m is the combined mass of ice and snow per unit area, $\overrightarrow{\tau_a}$ and $\overrightarrow{\tau_w}$ are the wind stress on ice and the ocean stress on ice, $\nabla \cdot \sigma$ is the internal ice stress, $-\hat{k} \times mf\mathbf{u}$ is the stress due to Coriolis effects, and $-mg\nabla H_0$ is the stress due to sea surface slope.

CICE use the elastic-viscous-plastic (EVP) sea ice dynamic model by Hunke and Dukowicz (1997). The EVP model is a modification of the viscous-plastic (VP) model for sea ice dynamics. The rheology of sea ice is based on the VP constitutive law

$$\frac{1}{E}\frac{\partial \sigma_1}{\partial t} + \frac{\sigma_1}{2\zeta} + \frac{P}{2\zeta} = D_D \tag{A.19}$$

$$\frac{1}{E}\frac{\partial \sigma_2}{\partial t} + \frac{\sigma_2}{2\eta} = D_T \tag{A.20}$$

$$\frac{1}{E}\frac{\partial \sigma_{12}}{\partial t} + \frac{\sigma_{12}}{2\eta} = \frac{1}{2}D_S \tag{A.21}$$

where

$$\begin{aligned}
&\sigma_1 = \sigma_{11} + \sigma_{22} \\
&\sigma_2 = \sigma_{11} - \sigma_{22} \\
&D_D = \dot{\varepsilon}_{11} + \dot{\varepsilon}_{22} \\
&D_T = \dot{\varepsilon}_{11} - \dot{\varepsilon}_{22} \\
&D_S = 2\dot{\varepsilon}_{12} \\
&\dot{\varepsilon}_{ij} = \tfrac{1}{2}(\tfrac{\partial u_i}{\partial x_j} + \tfrac{\partial u_j}{\partial x_i}) \\
&\zeta = \tfrac{P}{2\Delta} \\
&\eta = \tfrac{P}{2\Delta e^2} \\
&\Delta = [D_D^2 + \tfrac{1}{e^2}(D_T^2 + D_S^2)]^{1/2} \\
&P = P^* h exp(-C(1 - a_i))
\end{aligned} \tag{A.22}$$

where P^* and C are empirical constants, h is the mean ice thickness, and a_i is ice concentration.